MULTI-DIMENSIONAL MODELLING OF EVAPORATION IN THE MICRO REGION OF A MICRO GROOVED HEAT PIPE

A THESIS SUBMITTED TO
THE GRADUATE SCHOOL OF NATURAL AND APPLIED SCIENCES
OF
MIDDLE EAST TECHNICAL UNIVERSITY

BY

YİĞİT AKKUŞ

IN PARTIAL FULFILLMENT OF THE REQUIREMENTS
FOR
THE DEGREE OF DOCTOR OF PHILOSOPHY
IN
MECHANICAL ENGINEERING

JUNE 2015

Approval of the thesis:

MULTI-DIMENSIONAL MODELLING OF EVAPORATION IN THE MICRO REGION OF A MICRO GROOVED HEAT PIPE

submitted by **YİĞİT AKKUŞ** in partial fulfillment of the requirements for the degree of **Doctor of Philosophy in Mechanical Engineering Department, Middle East Technical University** by,

Prof. Dr. Gülbin Dural Ünver
Dean, Graduate School of **Natural and Applied Sciences**

Prof. Dr. Raif Tuna Balkan
Head of Department, **Mechanical Engineering**

Prof. Dr. Zafer Dursunkaya
Supervisor, **Mechanical Engineering Dept., METU**

Prof. Dr. Hakan Işık Tarman
Co-supervisor, **Engineering Sciences Dept., METU**

Examining Committee Members:

Assoc. Prof. Dr. Tuba Okutucu Özyurt
Mechanical Engineering Dept., METU

Prof. Dr. Zafer Dursunkaya
Mechanical Engineering Dept., METU

Prof. Dr. Yusuf Özyörük
Aerospace Engineering Dept., METU

Assoc. Prof. Dr. Barbaros Çetin
Mechanical Engineering Dept., Bilkent University

Assist. Prof. Dr. Yegân Erdem
Mechanical Engineering Dept., Bilkent University

Date:

I hereby declare that all information in this document has been obtained and presented in accordance with academic rules and ethical conduct. I also declare that, as required by these rules and conduct, I have fully cited and referenced all material and results that are not original to this work.

Name, Last Name: YİĞİT AKKUŞ

Signature :

ABSTRACT

MULTI-DIMENSIONAL MODELLING OF EVAPORATION IN THE MICRO REGION OF A MICRO GROOVED HEAT PIPE

AKKUŞ, YİĞİT
Ph.D., Department of Mechanical Engineering
Supervisor : Prof. Dr. Zafer Dursunkaya
Co-Supervisor : Prof. Dr. Hakan Işık Tarman

June 2015, 143 pages

Capillary cooling devices are preferred in heat removal from electronic components which are characterized by high heat dissipation rates. Heat pipes use various wick structures to generate the necessary capillary action. Heat pipes that use grooved micro-channels as wick structures, have been widely studied by researchers due to the fact that their simple geometry enables the modelling of fluid flow and heat transfer both analytically and numerically. Near the attachment point of liquid-vapor free surface to the groove wall tip, there exists an extended meniscus geometry which is generally known as the micro region. The low thermal resistance across the evaporating thin film of the micro region enables high heat transfer rates, and a considerable amount of the evaporation originates from this region. In the literature, evaporation has been modelled using the unidirectional flow assumption of the liquid. In the present study, the three directions of the liquid flow are considered. This thesis solves the evaporation in the micro region with the unidirectional flow model starting from a location where the effect of disjoining pressure is small. Unlike many studies in the literature, the boundary conditions defined at the starting point are not tuned during the solution procedure to match the undisturbed meniscus radius. The results of the unidirectional flow based model reveal that the curvature of the film thickness profile may change its sign and bends inward near the contact line depending on the physical system considered in the problem. Following unidirectional model, the present study applies the spectral element method to solve the linear momentum equations in order to get the effect of vertical flow of the liquid. Although the amount of inlet mass flow or the film thickness profile is not changed substantially with the application of bi-directional flow based evaporation model, determination of the distribution of vertical velocity in the micro region enables understanding of the underlying physical phenomena. Finally, the contribution of the axial flow to evaporation is investigated by solving the distribution of axial velocity using spectral element method and the contribution of the axial flow to evaporation is found to be negligible. Systems which form small apparent contact angles at a definite superheat, are found to have higher heat removal capacity.

Keywords: Grooved heat pipe, extended meniscus, micro region, evaporating thin film

ÖZ

MİKRO KANALLI BİR ISI BORUSUNUN MİKRO BÖLGESİNDEKİ BUHARLAŞMANIN ÇOK BOYUTLU MODELLENMESİ

AKKUŞ, YİĞİT
Doktora, Makina Mühendisliği Bölümü
Tez Yöneticisi : Prof. Dr. Zafer Dursunkaya
Ortak Tez Yöneticisi : Prof. Dr. Hakan Işık Tarman

Haziran 2015 , 143 sayfa

Yüksek ısı atım değerlerine sahip elektronik bileşenlerin soğutulmasında kılcal sıvı taşınması prensibi kullanarak soğutma sağlayan cihazlar tercih edilmektedir. Isı borularında kılcal taşınmayı sağlayan çeşitli fitil yapıları mevcuttur. Mikro oluklu kanalları fitil yapısı olarak kullanan ısı boruları basit geometrilerinin analitik ve sayısal modellemeyi kolaylaştırması sebebiyle araştırmacılar tarafından sıklıkla çalışılmaktadır. Sıvı-gaz serbest yüzeyinin oluk duvarının ucu ile birleştiği nokta yakınında, literatürde genellikle mikro bölge olarak bilinen, esnemiş bir menisküs geometrisi oluşmaktadır. Mikro bölgedeki buharlaşan ince film tabakası düşük ısı direnci sebebiyle dikkate değer oranda buharlaşmanın gerçekleştiği bir bölgedir. Literatürde, buharlaşma modelleri genellikle tek yönlü sıvı akışı durumuna göre oluşturulmuştur. Bu çalışmada ise, üç yönden de sıvı akışı göz önüne alınmıştır. Çalışmaya, tek yönlü sıvı akışına bağlı yaklaşımın, ayrılma basıncının yeterince düşük olduğu bir noktada tanımlanan başlangıç koşulları kullanılarak, modellenmesiyle başlanmıştır. Literatürdeki pek çok çalışmadan farklı olarak, deforme olmamış menisküs yarıçapını tutturmak amacıyla, çözüm sırasında sınır koşullarıyla oynamalar yapılmamıştır. Tek yönlü sıvı akışına bağlı modelin sonuçları, problemde ele alınan fiziksel sisteme göre, film kalınlığı profilinin eğriliğinin işaret değiştirip içeri yönlü bükülebildiğini göstermiştir. Tek yönlü modeli takiben, dik yöndeki sıvı akışının etkisini de işin içine katmak için, momentum denklemleri spektral element yöntemi ile çözülmüştür. İki yönlü akışa bağlı modelin uygulanması sonucunda film kalınlığı dağılımının veya girişteki kütle akışı miktarının çok değişmemesine rağmen, mikro bölgede dikey hız dağılımın belirlenmesi, problemin altında yatan fiziksel mekanizmayı anlamayı kolaylaştırmıştır. Son olarak, eksenel yöndeki akışın buharlaşmaya olan katkısı, eksenel hız dağılımının spektral element yöntemi ile çözülmesiyle araştırılmıştır ve eksenel yöndeki akışın buharlaşmaya önemli bir etkisinin olmadığı bulunmuştur. Belirli bir sıcaklık farkında daha düşük temas açılarına sahip sistemlerin daha yüksek ısı atma kapasitesilerine sahip oldukları belirlenmiştir.

Anahtar Kelimeler: Oluklu ısı borusu, esnemiş menisküs, mikro bölge, buharlaşan ince film

To my parents, daughter and wife

ACKNOWLEDGMENTS

The author wishes to express his deepest gratitude to his thesis supervisor Dr. Zafer Dursunkaya for his expert guidance, understanding and encouragement. Without his wisdom and full support, this work could not be completed.

The author wishes to express his appreciation to his thesis co-supervisor Dr. Hakan Işık Tarman for his expert guidance, especially in spectral element methods.

The author expresses his appreciation to his superior Emre Aynagöz, manager Dr. Akif Türker Gürer and director Serdar Terzi for their support during the doctorate studies.

The author wishes to express his appreciation to ASELSAN A.Ş. that is the leading company of defence industry in Turkey and supports graduate studies of its employees.

The author specially would like to thank his beloved wife Pınar Zengin Akkuş, daughter Arya Akkuş, mother Nurcan Düzenli, father Necati Akkuş and sister Seda Akkuş for their unconditional love and support.

Lastly, the author would like to thank the Scientific and Technological Research Council of Turkey for its financial support (TÜBİTAK-2211-A).

TABLE OF CONTENTS

CHAPTERS

APPENDICES

LIST OF TABLES

TABLES

LIST OF FIGURES

FIGURES

LIST OF ABBREVIATIONS

A_d	Dispersion constant, J
b	Half groove width, m
c	Mean speed, m/s
h	Groove depth, m
h_{lv}	Latent heat of evaporation, J/kg
k	Thermal conductivity, $\mathrm{W/m \cdot K}$
k_B	Boltzmann constant
M	Molar mass of liquid, kg/mol
$\dot{m}$	Mass flow rate, kg/s
$\dot{m}'$	Mass flow rate per unit length, kg/m·s
$\dot{m}''$	Mass flux, $\mathrm{kg/m^2 \cdot s}$
N_A	Avagadro's number
n	Total number of molecules
P	Pressure, Pa
P_c	Capillary pressure, Pa
P_d	Dispersion pressure, Pa
q''	Heat flux, $\mathrm{W/m^2}$
Q'	Heat transferred per unit length, W/m
R	Liquid–vapor interface radius, m
R_u	Universal gas constant, J/mol· K
s	Transformed coordinate in x-direction, m
t	Transformed coordinate in y-direction, m
T	Temperature, K
U	Velocity, m/s
u	Velocity in x-direction, m/s
v	Velocity in y-direction, m/s
v_g	Specific volume of gas, $\mathrm{m^3/kg}$
v_l	Specific volume of liquid, $\mathrm{m^3/kg}$

V	Molar volume, $\mathrm{m^3/mol}$
w	Velocity in z-direction, m/s
w^*	Total free energy, J
x	Vertical direction, m
y	Horizontal direction, m
z	Axial direction, m
	Greek Symbols
γ	Specific surface free energy, J
δ	Liquid film thickness, m
μ	Dynamic viscosity, Pa$\cdot$ s
ν	Kinematic viscosity, $\mathrm{m^2/s}$
Ω	Problem domain
ρ	Density, $\mathrm{kg/m^3}$
σ	Surface tension, N/m
$\hat{\sigma}$	Accommodation coefficient
$\bar{\bar{\sigma}}$	Stress tensor
θ	Liquid–solid contact angle
	Subscripts
$evap$	Evaporative
l	Liquid
lv	Liquid–vapor
m	Single molecule
ne	Non-evaporating
v	Vapor
w	Wall
x	Component along the x–coordinate
y	Component along the y–coordinate
z	Component along the z–coordinate

CHAPTER 1

INTRODUCTION

Heat pipe is a closed device which operates passively between a heat source and a heat sink. Thermal energy is removed from the heat source by means of evaporation of liquid and subsequent vapor flow away from the heat source or evaporator. The vapor condenses near the heat sink, or condenser, and condensate returns to the evaporator by the capillary action.

A typical heat pipe is a sealed tube. The inner wall of the tube has a wicking structure to generate capillary effect. In the manufacturing of a heat pipe, tube is vacuumed in order to lower the boiling point of the working fluid, subsequently the working fluid is added and the tube is hermetically sealed. Such a design provides the phase change of the working fluid with relatively small changes in temperature.

Heat pipes utilize the latent heat of evaporation of the fluid for transfer of heat between high and low temperature reservoirs. When one end of the heat pipe is subjected to a heat load, the working fluid evaporates and the newly formed vapor flows through the hollow core of tube to the cold end of the pipe. In the cold end, heat is removed from the heat pipe and the vapor condenses. The condensate travels back to the hot end of the heat pipe by the capillary action of the wick structure surrounding the inner wall of heat pipe. This cycle continues as long as a temperature difference exists between the two ends of heat pipe. The working cycle of a heat pipe is given in Figure 1.1.

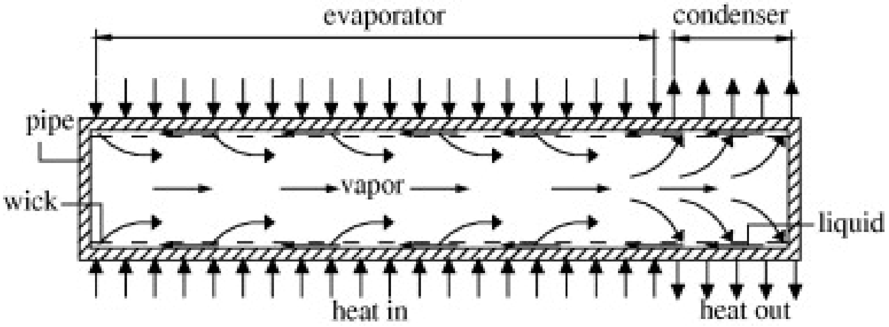

Figure 1.1: Working principle of a heat pipe [1]

Capillary action can be defined as the motion of liquid through narrow tubes or permeable substances due to adhesive and cohesive forces between the liquid and the surface. It only occurs when the adhesive forces which are the attraction of dissimilar particles, are stronger than the cohesive forces which are attraction of similar particles. The wicking structure providing the capillary action, may be any material capable of exerting capillary pressure on the condensed liquid to wick it back to the heated end. In commercial heat pipes, three main types of wick structures are used, namely sintered powder wick, grooved wick and wire mesh wick. The sintered powder is formed in a bonding process and porous structure provides the capillary action. Grooved wick is composed of fine channels located in the periphery of the inner wall. Channels may have different geometries such as triangular, rectangular or trapezoidal. The wire mesh screen wick is, on the other hand, composed of multiple layers of interwoven wires applied to the inner wall of the heat pipe.

In Figure 1.2, examples of heat pipes having different wick structures can be seen. The pictures on the left show the cross-sections of the heat pipes. In the pictures on the right, on the other hand, heat pipes are cut and opened to show their wick structures surrounding their inner walls. From top to bottom, examples of sintered, grooved and mesh screen wick structures can be seen.

Figure 1.2: Wick structures [2]

In the design of a wick structure, pore size optimization should be carefully made. Pore size should be small enough to get the maximum capillary head. On the other hand, it shouldn't be too small such that the permeability of the wick structure is reduced.

In addition to the proper selection of the wick structure, the material of the wall of the heat pipe should be properly selected. The very first requirement for the wall material is its compatibility with the working film. Materials which have high energy surfaces, are generally desired to get wetting systems. Secondly, thermal conductivity of the material should be high because conduction through the heat pipe wall should be high to provide high heat transfer rates from the heat source.

After the selection of the wick structure and wall material, the type of the working fluid should be decided. The fluid must form a wetting or partial wetting system on the wall material. To create adequate capillary head, the surface tension of the fluid should be sufficiently high. The latent heat of the fluid should also be high to increase the amount of heat removal. Fluids which can operate in very low temperatures must be selected in space applications such as liquid nitrogen. Inversely, high temperature applications of heat pipes, such as cooling of reactors, require the utilization of liquid metals. The common usage of heat pipes occurs in the cooling of electronic components, most commonly in computer processors. Working fluids used in these heat pipes are water, ammonia and acetone. In summary, the operation conditions determine the selection of heat pipe and its components. An improperly selected or designed heat pipe will not function efficiently. The heat pipe may experience dry out or it may not initiate its operation.

1.1 Types of Heat Pipes

1.1.1 Traditional Cylindrical Heat Pipes

These are the simplest and most popular type of heat pipes. They are used in most applications to transfer thermal energy from one point to another. The shape of the cross-section is generally cylindrical or similar rounded geometries. The inner wall of the heat pipe is composed of different wick structures depending on the application. The shape of the pipe can be adjusted by bending. However, every bending creates extra resistance against fluid flow through the wick structure. Thus, the number and the radius of curvature of the bends should be carefully decided. Heat pipes shown in Figure 1.2, are also examples of traditional heat pipes.

1.1.2 Micro Heat Pipes

Micro heat pipes consist of long thin non-circular channels. Sharp-angled corners of channel work as liquid arteries. Micro heat pipes can be characterized by the equation: $r_c/r_h \geq 1$ where r_c is the capillary radius, *i.e.* radius in a cross-section and r_h is the hydraulic radius, *i.e.* radius along the heat pipe axis. The size of hydraulic radius is generally about $100\,\mu$m. Micro heat pipes with various cross-sections are shown in Figure 1.3.

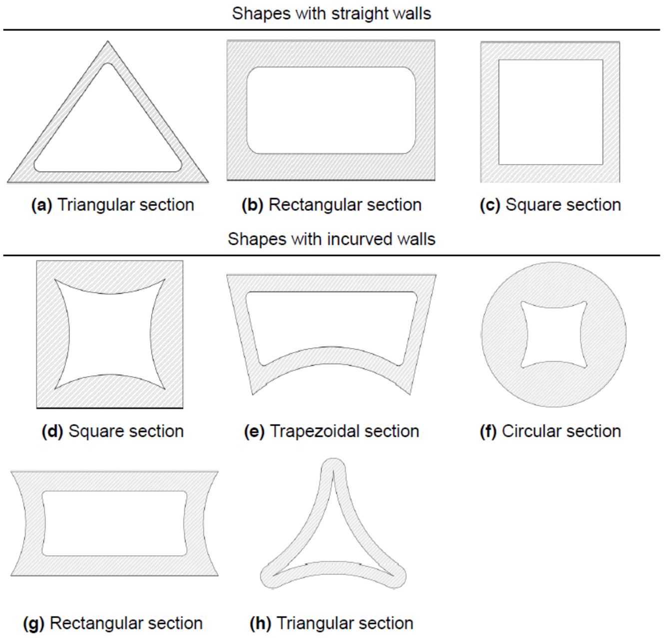

Figure 1.3: Various cross-sections of micro heat pipes [3]

1.1.3 Flat Heat Pipes

Flat heat pipes are very similar to traditional cylindrical heat pipes especially in terms of working principles but they have a rectangular cross-section instead. In addition to the purpose of heat removal, flat heat pipes are capable of temperature flattening on electronic devices due to their geometry. In Figure 1.4, a schematic of a flat heat pipe geometry can be seen.

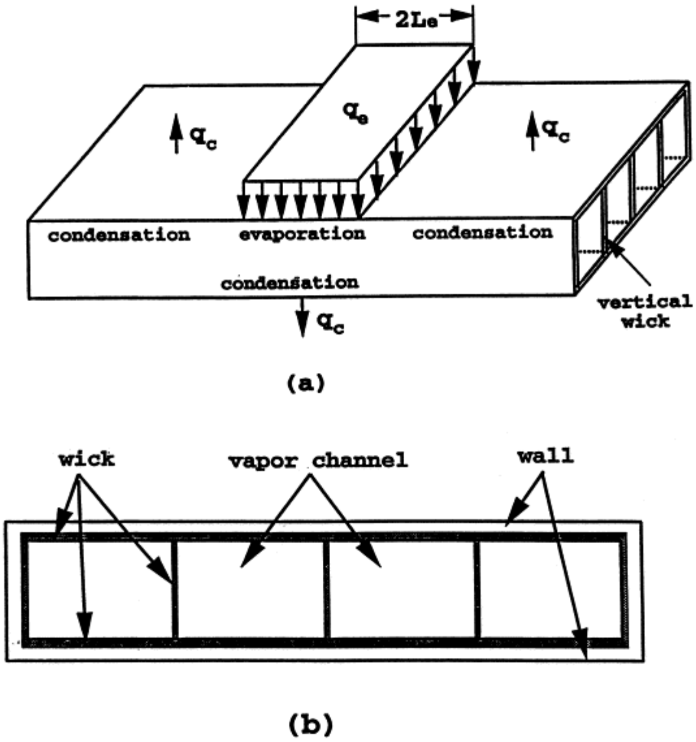

Figure 1.4: Schematic of a flat heat pipe: (a) geometry of heat pipe and (b) cross-sectional view [4]

1.1.4 Loop Heat Pipes

Loop heat pipes have the advantage of being able to provide reliable operation over a long distance. They can transport a large heat load over a long distance with a small temperature difference. Their ability of operating against gravity makes them the first choice in aerospace applications. Differing from the standard heat pipes, loop heat pipes have separate vapor and liquid lines. They have a compensation chamber which helps maintain the fluid inventory. Figure 1.5 exhibits the operation cycle of a loop heat pipe.

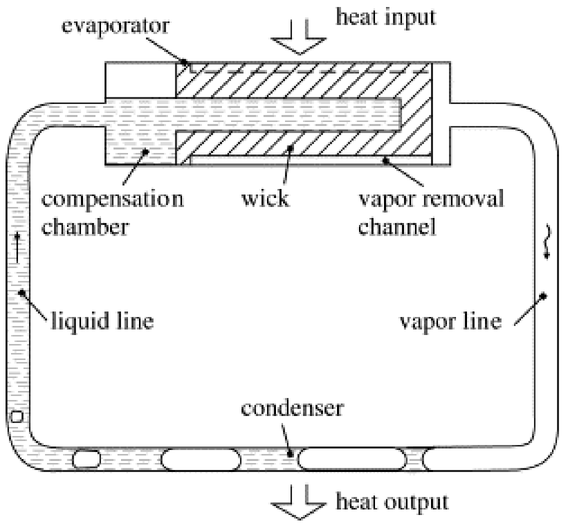

Figure 1.5: Operation cycle of a loop heat pipe [5]

1.1.5 Variable Conductance Heat Pipes

The variable conductance heat pipe, sometimes called the gas-controlled or gas-loaded heat pipe, has the ability of maintaining a device mounted at the evaporator at near constant temperature. This feature is achieved by maintaining constant pressure but at the same time varying the condensing area, which is called “gas buffering”. The reservoir filled with inert gas has a pressure equal to saturation pressure during normal operation. However, when the heat load at the source is increased, saturation pressure also increases which pushes the gas in the reservoir. When the volume occupied by the reservoir decreases, condensing area increases. Thus, more heat is removed *via* the heat pipe. Figure 1.6 shows a schematic for a variable conductance heat pipe.

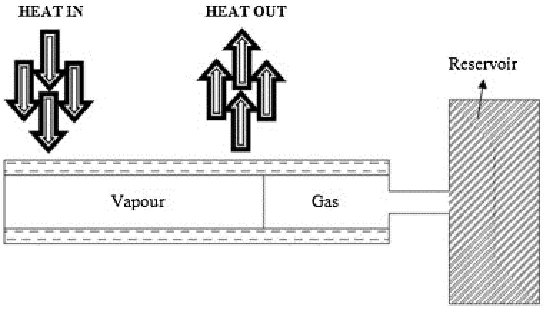

Figure 1.6: Variable conductance heat pipe [6]

1.2 Literature Review

The study of Bressler and Wyatt [7] in 1970 is one of the major initial studies which examine the surface wetting and evaporation of a fluid in a capillary groove. Capillary rise of the liquid was balanced by the gravity and the wall shear was taken into consideration in fluid flow which supplies liquid to the evaporating meniscus. Unidirectional average fluid velocity was assumed in the direction which is parallel to the groove wall. At the liquid-vapor interface, normal velocity gradient was taken as zero. Moreover, deformation of the meniscus due to disjoining pressure wasn't studied. The study of Bressler and Wyatt [7] did not apply any special phase change model at the the liquid-vapor interface. Evaporation at the liquid-vapor interface was assumed to take place due to thermal conduction through the liquid film. The wall temperature of the groove and the liquid-vapor interface temperatures were taken as constants. Based on these simple assumptions, Bressler and Wyatt [7] evaluated the average heat flux in an evaporating meniscus.

In 1971, Wayner and Coccio [8] conducted the first study concerning heat and mass transfer in the vicinity of triple interline of a meniscus formed on a flat plate immersed in a pool of liquid. The concepts of triple interline or simply interline which are frequently used in this study [8] and also in the literature, indicate the solid-liquid-vapor interface formed at the end of the meniscus. The study [8] had an experimental part and analytical part in which results of experimental part were used. In the experimental part, a pair of flat plates joined back to back and a row of thermocouples was sandwiched between them. This assembly was partially immersed to in a pool of liquid which was at controlled temperature. The assembly was heated from the top by means of a resistance heater and heat is conducted down the plates into the meniscus region. In the analytical part, firstly, two-dimensional differential equation for the steady state temperature in the plate was solved. For the boundary conditions, center line temperature distribution of the plates, the temperature of the top of the plates and the temperature of the bottom of the plates were experimentally determined. On the other hand, the last boundary condition, the temperature distribution on the surface of the plates, was assumed initially. The appropriateness of the assumed profile was checked comparing the center line temperature distributions found from the analytical solution and from the experimental results. After the determination of the temperature distribution in the plates, Wayner and Coccio [8] applied Fourier's law of conduction to find the film thickness distribution in the interline region. Interface temperature between liquid and vapor was assumed at the equilibrium saturation temperature. Calculated profiles of film thickness were found to be significantly thinner than equilibrium profile revealing the result that heat transfer process in the interline region cannot be explained by only using purely conduction model. Authors of [8], have concluded that large resultant heat flux in the interline region required a considerable additional work. Moreover, at the end of their study, Wayner and Coccio [8] suggested the thin film transport model which uses the concept of disjoining pressure, to explain the accelerated rates of evaporation in the interline region.

Wayner had continued his studies to understand the physical mechanisms near the contact line in following years. In 1972, Potash and Wayner [9] published the first study which use the concept of disjoining pressure in the liquid and the concept of interfacial resistance in the phase change phenomena. Authors [9] divided an evaporating meniscus which is formed on the surface of a hot vertical plate immersed in a pool of liquid, into three regions. The main or bulk portion of the meniscus which is originating from the surface of the liquid reservoir, is described by the conventional equation of capillarity. This region was named as intrinsic meniscus. The region of the meniscus where evaporation takes places and disjoining pressure plays an effective role, was named as evaporating thin film. The ultra thin film region where there is no evaporation, was named as equilibrium thin film. Intrinsic region with evaporating and equilibrium film regions were named as extended meniscus. The formation of thin film regions which first appeared in the literature by the study of Potash and Wayner [9], at the end of the intrinsic region is due to the existence of disjoining pressure which increases with decreasing film thickness and the definition and explanation of disjoining pressure shall be made in “Chapter 2” of the thesis, in detail. The data of disjoining pressure vs. film thickness was taken from the study of Derjaguin and Zorin [10] which is the first study in which theory of thin film adsorption and disjoining pressure were explored both theoretically and experimentally. Although it was not stated in [9], Wayner pointed in his following study [11] that contact angle was taken as zero in [9]. Depending on this assumption, Potash and Wayner [9] started the calculation for the evaporating meniscus from the intersection of equilibrium thin film region and evaporating thin film region with zero film thickness slope. The slope at the end of the first increment of the solution domain was calculated using an equation derived from the balance of disjoining pressure and hydrostatic head. The size of the increment was taken as 1 nm. Knowing the slope and the increment length, the film thickness at the end of the increment was calculated. Disjoining pressure corresponding to this film thickness, was obtained from the data of [10] as explained previously. Knowing the disjoining pressure, the film vapor pressure was calculated from a modified version of Kelvin equation suggested by Padday [12]. Heat flux was calculated from the equation derived from the interfacial resistance to evaporation by Schrage [13]. In the use of Schrage’s equation vapor temperature and interface temperature were taken as equal to simplify the equation. Both in modified Kelvin equation and Schrage’s equation, a constant interface temperature was used along the increment. Correction of this assumption was made applying Fourier’s law of heat conduction formula between the wall surface kept at a constant temperature and interfacial surface using the value of heat transferred found. After, iterations were repeated until there was a negligible change in the interfacial temperature, the final amount of the heat transferred or the mass evaporated from the first increment was calculated and the average fluid velocity entering the first increment from the second increment was calculated such that all of the evaporated mass supplied by the fluid flow. Calculations were continued for the consecutive increments until the film became sufficiently thick and the disjoining pressure had a negligible effect on the heat flux. In the intrinsic region, Clausius-Clapeyron equation was used to find vapor pressure of the film which was substituted into Schrage's equation to find the amount of heat transfer in an increment. The volumetric flow entering an increment was equated to the evaporated mass, again. In the absence of disjoining pressure gradient, change of meniscus curvature resulting from the hydrostatic change was responsible for fluid flow. At the start of the intrinsic region, various initial curvatures were tried until the resulting curvature became zero at the surface of the pool. At the end of the solution procedure, Potash and Wayner [9] found the heat flux, vertical liquid pressure, average velocity and film thickness distributions both in thin film and intrinsic meniscus regions. Authors reported that change in disjoining pressure in the thin film region and change in capillary pressure in the intrinsic region were sufficient to generate the fluid flow required for evaporation. Moreover, authors observed that the velocity and heat flux profiles went through their maximum values near the contact line and returned negligible values when the meniscus became relatively thick.

In 1973, Wayner [11] discussed the fluid flow of an evaporating meniscus having a non-zero contact angle. He called this type of meniscus as a “nonwetting meniscus”. Due the fact that equilibrium film pressure can be greater than spreading coefficient of solid-liquid interface, the author concluded that an intrinsic meniscus and an adsorbed thin film can exist together for a non-zero contact angle meniscus. However, following Derjaguin and Zorin [10], Wayner stated that “the contact angle can differ from zero only if no continuous transition from the adsorption layer to the bulk phase through a series of increasing thickness corresponding to thermodynamically stable states is possible.” Thus, for the quantitative description of the evaporation, discontinuous film thickness data is necessary in a non-zero contact angle meniscus system.

In 1976, Wayner *et al.* [14] studied the evaporation and fluid flow in the thin film region of a horizontal meniscus and considered only the disjoining pressure excluding the effect of the curvature change and gravity. a wetting liquid, in other words the system having a zero-contact angle, was studied. Furthermore, the analysis was restricted to the use of a non-polar liquid because disjoining pressure of non-polar liquids can be described by a simple power relation as suggested by the study of Derjaguin and Zorin [10]. Assuming continuum, neglecting inertial terms due to small liquid velocities and neglecting the second derivative of the velocity with respect to flow direction, 1-D steady momentum equation was solved in the direction of flow which was assumed to be parallel to solid wall, to find the velocity distribution. These assumptions on the momentum equation are also known as lubrication assumptions. The amount of evaporation from the surface was calculated based on Schrage's [13] evaporation model. Similar to the previous study of Potash and Wayner [11], in the use of Schrage's equation vapor temperature and interface temperature were taken as equal to simplify the equation. However, to find the vapor pressure of the film which were substituted into Schrage's equation, both Clausius-Clapeyron equation and the equation suggested by Derjaguin [10] were used enabling a more comprehensive approach. The equation suggested by Derjaguin [10], on the other hand, is similar to Kelvin equation but capillary pressure is replaced with disjoining pressure. At the end, evaporative mass flux leaving the film surface was equated to liquid mass flow rate per unit width of the film. Resulting differential equation for the film thickness was solved using the orthogonal collocation method. As one of the initial conditions, interline film thickness was used but its value was slightly increased, without an explanation. The other initial condition was the film slope at the interline which was zero due to the use of wetting liquid.

In 1978, Renk *et al.* [15] studied the shape of a zero contact angle meniscus formed on an isothermal flat plane. Although [15] did not include any evaporation process, this study had importance due to the fact that it was the first study which continuously used the disjoining and capillary pressures together with hydrostatic pressure in the whole meniscus.

In 1979, Holm and Goplen [16] studied the heat transfer in a meniscus formed between the walls of a liquid-filled capillary groove. Only the effect of disjoining pressure was used which reduced the vapor pressure at the liquid-vapor interface in the evaporating thin film region. Capillary pressure, on the other hand, was used to calculate the film pressure at the liquid-vapor interface in the intrinsic region. A wedge flow model was applied to determine the pressure gradient in the liquid. Holm and Goplen [16] solved the heat transfer problem in several capillary groove configurations and presented their results with respect to geometrical parameters of the grooves.

In 1979, Wayner [17] studied the interline region of a falling evaporating thin film. The difference between the real and apparent contact angles was emphasised. Furthermore, real contact angle was analyzed for both isothermal and evaporating conditions. Isothermal contact angle for wetting fluids had already been accepted as zero. However, at the interline of a falling evaporating film real contact angle was found to be very small and it was a function of the temperature gradient and the interline velocity. Lastly, heat sink capability of a simple fluid on metal was larger than that of a simple fluid on glass due to higher London-van der Waals dispersion force of the metal-fluid system, in other words, due to higher disjoining pressure created by the metal-fluid system with respect to the glass-fluid system.

Renk and Wayner conducted an experimental study [18] for an evaporating ethanol meniscus in 1979. Authors measured the profile of the meniscus using the optical technique of interferometry for different heat loads. Measurements showed that the evaporating meniscus profile was stable and that it was a function of the heat load. In order to complete the study, authors made a following analytical study [19]. Due to the fact that ethanol is a polar liquid, it was accepted as a non-wetting liquid and a finite contact angle meniscus was assumed and the disjoining pressure was neglected. In the calculation of liquid pressure gradient, all derivatives of the film thickness were ignored except the highest derivative term, the third derivative. There was no phase change model used at the interface. The major difficulty of suggesting an analytical model was the lack of experimental data in the close vicinity of contact line. Renk and Wayner [19] proposed an equation which was believed to represents the volumetric flow rate in the evaporating meniscus, and claimed that the use of the incoming volumetric flow rate coupled the microscopic fluid flow model to the macroscopic heat transfer measurements. Then, equating the incoming volumetric flow rate to the mass flux of liquid calculated from the liquid pressure gradient, Renk and Wayner [19] solved a third order differential equation starting from the interline. As a first initial condition, film thickness was assumed as zero due to the absence of disjoining pressure in the model. Other initial conditions were non-zero first and second derivatives of the film thickness due to nonwetting liquid. Results showed that evaporative heat flux distribution started at zero at the interline, went through a maximum at the very near point to the interline and approached zero asymptotically with increasing meniscus thickness.

In 1980, Moosman and Homsy [20] modelled the transport process in an evaporating meniscus using the same geometry of studies [15] and [19]. In modelling, Moosman and Homsy included the effects of both capillarity and multilayer adsorption. In the formulation of the evaporating flow, they eliminated the interface temperature in favour of the wall temperature and defined a new temperature jump concept between the wall and the vapor. Furthermore, Moosman and Homsy [20] applied a scaling process on the governing equations. This approach was the first explanatory order of magnitude analysis applied on the individual terms in equations which govern the conservation of mass, linear momentum and energy in an evaporating meniscus. On the other hand, Moosman and Homsy [20] reduced the governing equations to two non-linear equations, which contain non-dimensional liquid pressure and non-dimensional film thickness as unknowns. They solved this set of equations with the corresponding boundary conditions assuming infinite domain in the positive and negative longitudinal directions. In the solution procedure of the set of equations dependent variables, liquid pressure and film thickness, were expanded in a regular perturbation series about isothermal condition. Zeroth order solution which corresponded to isothermal solution and first order solution were taken into consideration. At the end of their study, Moosman and Homsy [20] stated that the perturbation solution was applicable for only extremely small superheat values which were not reasonable in practical applications. Full non-linear set of equations must be solved to simulate a realistic problem.

In 1980, Wayner made a study [21] regarding the film thickness profile in the vicinity of the contact line of an isothermal finite contact angle system. The author had analyzed non-zero contact angle systems in his previous study [11] and concluded that it is possible for an intrinsic meniscus and an adsorbed thin film to exist together. Wayner's study published in 1980 [21], on the other hand, suggested a model which enabled the calculation of film thickness distribution in the contact line region of a finite contact angle system but the presence of non-evaporating region was not included in this study. In modelling effort, Wayner augmented the disjoining pressure to the Young-Laplace equation of capillarity. However, the author used capillary pressure and disjoining pressure with different signs stating that "for a system at equilibrium, the vapor pressure change due to capillarity has to be offset by an equal vapor pressure change of opposite sign due to film thickness". Starting his analysis with zero initial slope and effective thin-film thickness of the order of interatomic spacing at the contact line, Wayner demonstrated that finite apparent contact angle system could be formed with substantial initial curvature. Finding a thin-film thickness of the order of interatomic spacing at the contact line contradicted with the thicker thin-film equilibrium results of Derjaguin [10]. However, referring to the study of Hu and Adamson [22] who pointed out the incapability of their experiment on differentiating between patches of fluid and a continuous film, Wayner claimed that patches of fluid indeed formed. Furthermore, due to the small dimension associated with the contact line region, Wayner preferred to use the term "effective" for values of curvature and thickness at the contact line.

In 1982, Wayner examined the relationship between the equilibrium shape of a thin film at the contact line, superheat, and interfacial forces for both zero and finite contact angle systems [23]. The systems having zero apparent isothermal contact angle were named as spreading systems and ones with finite apparent isothermal contact angle were named as non-spreading systems. Wayner used different signs for the capillary and disjoining pressures when forming the augmented Young-Laplace equation in his previous work [21] in which a finite contact angle system (non-spreading system) was studied. The author generalized this approach with use of the term "characteristic frequency for van der Waals interaction" which multiplies the disjoining pressure term and has different signs for spreading and non-spreading systems. For an isothermal spreading system, only a constant thickness adsorbed liquid film was predicted. For an evaporating spreading system, on the other hand, formation of an evaporating meniscus which is at equilibrium with its adsorbed non-evaporating film was predicted and this led to formation of an apparent contact angle. The contact line thickness was expected to be thinner in the evaporating spreading system with respect to isothermal spreading system. Curvature at the contact line was zero for both systems. Non-spreading systems, on the other hand, always had apparent contact angles but contact angle of the evaporating system was higher that that of the isothermal system. Likewise, there were finite curvature values of film profile at the contact line for both isothermal and evaporating non-spreading systems and curvature value of the evaporating system was higher.

In 1991, Sujanani and Wayner [24] studied the optical investigation of near-equilibrium thin liquid films. They compared their experimental results with the ones obtained from the theoretical solution. In the formulation of the problem, pressure jump between the liquid-vapor surface and bulk vapor phase was assumed constant over the transition region. However, this assumption was not verified in the study. Moreover, Sujanani and Wayner [24] used the minus fourth power of the film thickness to simulate the disjoining pressure in the whole problem domain. However, separate disjoining pressure formulations have been used for the thin and thick parts of the film in the literature. The study of Sujanani and Wayner [24] has importance regarding the formulation of the mass flux of vapor leaving the liquid-vapor interface. Although the same formulation was represented in different configurations in the past studies, the representation of Sujanani and Wayner [24] which contained the temperature and pressure jumps multiplied by two different constants, became a standard representation and is being used in current studies.

In 1992, Schonberg and Wayner [25] suggested an analytical solution to the governing equations in an evaporating film. However, they neglected the capillary effect in the close vicinity of the contact line which led to a misrepresentation of underlying physical phenomena.

In 1993, Dasgupta *et al.* [26] used the augmented Young-Laplace equation to evaluate experimental data for an extended meniscus. In the formulation of the problem, there were no order of magnitude analysis applied and gravity was also not considered. In the formulation of the fluid flow, lubrication assumption which was verified by Moosman and Homsy [20] in 1980, was applied. In the formulation of the curvature, a fairly flat film was assumed and square of the first derivative of the film thickness was assumed to be much smaller than unity. This approach was also verified by Moosman and Homsy [20]. For the evaporation of liquid at the interface, well-known temperature and pressure jumps model was used by following the representation of Sujanani and Wayner [24]. Evaporation model and liquid flow were combined but the augmented Young-Laplace equation was kept separate resulting a non-linear system of differential equations which is very similar to one found by Moosman and Homsy [20]. A Taylor series expansion of this non-linear system was used to tune the extremely sensitive initial conditions at the interline. Thickness of the non-evaporating film and the value of superheat were taken from the measurements of the experiment. The value of Hamaker constant was calculated from these measurements. Therefore, the average value of the modified Hamaker constant was measured *in situ*. Thus, constant thickness approximation to determine a value of Hamaker constant, was not anymore necessary. The experimental data of film thickness and the theoretically calculated profile were in a good agreement except for some small deviations in the transition region. Lastly, it should be stated that superheat values used in the experiment and theoretical calculations by Dasgupta *et al.* [26] were extremely small.

The following studies of Dasgupta *et al.* [27, 28] and Kim *et al.* [29] were quite similar regarding the formulation and solution strategies to the study of Dasgupta *et al.* [26].

In 1995, Schonberg *et al.* [30] studied the evaporation from a meniscus formed in a channel of a heat pipe. Using the same formulation of the previous studies [26, 27, 28, 29], Schonberg *et al.* worked on a system which had very high values of superheats about 5 K. Analysis was not only performed in a micro region but also a definite part of the macroscopic region was included in the solution domain. Due to the radical divergence of the length scales of micro and macro regions, matched asymptotic expansion method was applied. Formulation of a stable evaporating meniscus with a very high heat flux was proved theoretically, however, it was stated that there were no experiments conducted for such high superheat values. Finally, Schonberg *et al.* [30] attributed the large apparent contact angles to large viscous stresses in the contact line region where fluid flow in an extremely thin film.

Stephan and Busse [31] studied the heat transfer in a grooved heat pipe combining the solution of a two-dimensional heat conduction problem with the calculation of the shape of the liquid-vapor interface and its temperature in 1992. Unlike other studies in the literature [26, 27, 28, 29, 30], Stephan and Busse [31] merged the governing differential equations and solved a single differential equation having all boundary conditions defined at the intersection of absorbed layer and evaporating thin film. With this representation, the problem became an initial value problem solved with fourth order Runge-Kutta method. In the application of initial conditions, the film thickness and the film curvature were perturbed from their original values by assuming very small capillary pressure instead of zero capillary pressure. Thus, the possibility of having a trivial solution was prevented. Furthermore, the third derivative of the film thickness at the origin was iterated so that integration ended in a meniscus with desired curvature. Stephan and Busse [31] also investigated the effect of using varying wall temperature along the micro region and concluded that wall temperature is nearly constant in the micro region. Finally, authors stated that the assumption of an interface temperature equal to the saturation temperature of the vapor could lead to a large over-prediction of heat transfer coefficient.

In 1996, Ha and Peterson [32] studied the analytical investigation of heat transfer characteristics for evaporating thin liquid films in V-shaped microgrooves. This study was important in two aspects. First one was that the liquid flow in the axial direction of grooves was taken into consideration. The change of the radius of curvature in the intrinsic region part of the liquid-vapor interface was responsible for the axial flow and a first order differential equation with respect to the radius of curvature was derived and solved. Second important aspect of the study of Ha and Peterson [32] was the application of non-uniform heat flux along the axial direction of grooves. The evaporation at the interface, on the other hand, was modelled following the study of Schonberg and Wayner [25] which included only the disjoining pressure for the force balance at the liquid-vapor interface. The evaporative mass flux in the thin film region was matched with the applied non-uniform heat flux along the axial direction. Thus, the model of Ha and Peterson [32] enabled the understanding of the axial variation of the average heat transfer coefficient and the effective evaporating length.

The study of Thomas *et al.* [33] in 2001, was only about the liquid flow along trapezoidal grooves and did not analyze the evaporation process. In the formulation of liquid flow along the axis of a groove, Ha and Peterson [32] had been used a friction factor, but Thomas *et al.* [33] presented the two dimensional distribution of axial velocity by solving the non-dimensional Poisson equation which was derived from Navier-Stokes equation by assuming fully developed, laminar flow with negligible body and inertial forces. In order to get the dimensional values of axial velocity, pressure gradient along the axis had to be known which was function of the radius of curvature along the groove axis as suggested by Ha and Peterson [32].

In 2004, Launay *et al.* [34] studied the fluid flow along a micro-heat pipe array together with the evaporation and condensation processes. Condensation was modelled comprising the Nusselt theory and the assumption of a fourth order polynomial in the condensation film and transition region, respectively. Evaporation was modelled based on the suggestion of Wayner *et al.* [14]. The evaporation was modelled through a fourth order non-linear differential equation of film thickness which was solved using the fourth-order Runge-Kutta procedure. All the initial conditions were defined at the intersection of absorbed region and evaporating thin film region. The first and second derivatives of the film thickness were taken as zero. Although the fact that the use of this set of initial conditions without any tuning of derivatives of film thickness could lead to a flat film having a thickness of absorbed layer, the authors [34] did not mention about experiencing such a difficulty in the numerical solution process.

In 2005, Wee *et al.* [35] studied the effects of the liquid polarity and the wall slip on the heat and mass transport characteristics of an evaporating thin film. Evaporation was modelled again following the suggestions of Wayner. The differential equation was solved starting from the intersection of the absorbed layer and evaporating thin film as in the study of Launay *et al.* [34]. However, Wee *et al.* [35] did explain how they tuned the initial conditions in order to prevent a trivial solution. Furthermore, the authors [35] stated that an iterative technique was employed on the initial conditions such that the solution converged to the appropriate curvature in the bulk meniscus region. Finally, it was found that the liquid polarity reduces the evaporation due to stronger van der Waals forces of polar liquid.

In 2007, Wang *et al.* [36] studied the evaporation from a meniscus formed between the walls of a micro-channel for different channel sizes. Formulation and the solution methodology were similar to the previous studies of Stephan and Busse [31] and Wee *et al.* [35]. However, Wang *et al.* [36] did not apply the assumption, which was commonly used in the literature and was suggested by Wayner *et al.* [14], in their evaporation model. The assumption was about the temperature values of bulk vapor and vapor at the close vicinity of the liquid-vapor interface. Wayner *et al.* [14] assumed the equality of the two temperatures in the net mass flux formula suggested by Schrage [13]. Wang *et al.* [36], on the other hand, studied the problem without applying this assumption and found that this assumption led to underestimation of interfacial evaporation heat transfer coefficient for superheats above 5 K. Lastly, Wang *et al.* [36] concluded that the contribution of the thin-film region to the overall heat transfer was inversely proportional to the channel size and wall superheat.

In 2008, Wang *et al.* [37] suggested an analytical solution to the problem which they solved in their previous study [36]. The two simplifications of the proposed analytical solution were the negligible capillary pressure assumption and the application of the simple evaporation model developed by Wayner *et al.* [14]. At the end of their study, the authors [37] concluded that the results of the full numerical model and simplified analytical model agreed well.

In 2009, Bertossi *et al.* [38] studied the modelling of heat and mass transfer in the micro region. The approach of Bertossi *et al.* [38] to the problem was similar to the study of Stephan and Busse [31] except the alteration of the initial conditions. Stephan and Busse [31] assumed very small capillary pressure, which led to small perturbations on the absorbed layer thickness and second derivative of the film thickness, at the intersection of absorbed layer and evaporating thin film region which was the starting point of the integration or could be named as origin. Bertossi *et al.* [38], on the other hand, assigned small perturbation parameters to the slope of the film and heat flux from the interface leading to small alterations on film thickness and first derivative of the film thickness at the origin, respectively. At the end of their parametric study, the authors [38] concluded that the contact angle and the radius of curvature of the intrinsic meniscus region were totally independent of each other.

The two different studies of Do *et al.* [39, 40] were about the thermal performance of grooved heat pipes. In the modelling effort of the evaporation from the micro region, Do *et al.* [39, 40] used the evaporation model suggested by Wayner *et al.* [14] but they chose the intersection of intrinsic meniscus and evaporating thin film region as the starting point of integration. The authors [39, 40] did not report any film thickness distribution or heat flux distribution in the micro region in detail.

In 2011, Du and Zhao [41] studied the evaporation of thin-film in a rectangular micro-channel. The authors used the same solution methodology of Wang *et al.* [36] except the far field boundary condition which was the radius of the intrinsic meniscus. Wang *et al.* [36] took the half of the channel height as the radius of curvature of intrinsic meniscus. However, Du and Zhao [41] developed a simple geometrical formulation to calculate the value of the radius of intrinsic meniscus so that the center of the meniscus was kept on the axis of the channel. With the application of the renewed boundary condition, Du and Zhao [41] found a larger intrinsic meniscus than the undisturbed conditions.

In 2012, Benselama *et al.* [42] studied the thermocapillary effects on steadily evaporating contact line region. The authors [42] started modelling the flow from the two-dimensional Navier-Stokes and continuity equations without neglecting any terms. Furthermore, normal stress balance, shear stress balance and energy balance at the interface were applied including thermocapillary effect and without any simplification to determine boundary conditions at the liquid-vapor interface. Governing equations were non-dimensionalized with related scaling parameters and a dimensionless system was developed. A domain perturbation method was used to solve zeroth and first order solutions of this system. Zeroth order formulation of the problem, on the other hand, reduced the lubrication model of Moosman and Homsy [20] except the thermocapillarity effect. However, the addition of the first order solution by perturbation was a new practice in the solution of heat and mass transfer from an evaporating meniscus. In addition, Benselama *et al.* [42] suggested their closed-form solution to be used in the estimation of correct and accurate contact line conditions for full micro region models, which require conditions on film thickness and its first three derivatives to start the solution.

In summary, up to 1992, a lot of experimental studies had been conducted. Common traits of these studies were estimating some of the physical parameters from the experiments, applying very small temperature difference (heat load) to the experimental systems and using boundary conditions both at the entrance and end of solution domains in theoretical verification. After 1992, in addition to experimental studies, pure theoretical studies were also made such as [31], [30], [36], [41]. Common traits of these studies were using non-measured physical parameters (properties), applying superheats which are suitable for engineering problems, starting solution from the contact line and assuming zero contact angle and zero curvature at the contact line. Furthermore, these studies have tuned the boundary conditions defined at the contact angle to achieve convergence.

Except a few studies such as [39, 40, 43], there exists no theoretical study which chose another the starting point of integration than contact line in the literature. Moreover, these a few studies did not present the results of any pressure or pressure gradient distributions in the micro region in detail. On the other hand, evaporation in the micro region has never been modelled including the effect of the flows in three directions.

1.3 Objective of the Thesis

The main objective of the present study is to develop a multi-dimensional evaporation model in the micro region of a micro grooved heat pipe considering the fluid flow from all three perpendicular directions. Moreover, in order to eliminate the dependencies of boundary conditions to the contact line, analysis is aimed to start from the bulk meniscus region. Furthermore, as an higher order method, spectral element method is aimed to use in the micro region to get sufficient accuracy.

CHAPTER 2

DEFINITIONS AND OUTLINE OF THE THESIS

2.1 Capillary Pressure

Capillary pumping is generated by surface tension forces at the liquid-vapor interface resulting from deformation of the interface curvatures along two orthogonal directions. Capillary pressure between liquid and vapor is written in accordance with the Young-Laplace equation:

$$P_c = \frac{\sigma}{R_1} + \frac{\sigma}{R_2}\,. \tag{2.1}$$

The radius of curvature along the groove axis is much larger than the radius of curvature at the cross-section of the groove. Then, one term at the right hand side of Equation 2.1 can be neglected. For simplicity, the subscript is dropped in the rest of the study,

$$P_c = \frac{\sigma}{R}\,. \tag{2.2}$$

2.2 Disjoining Pressure

2.2.1 Definition and Formulation

In order to remove a small increment of liquid layer from the bulk of the liquid film, generally an equilibrium force is required. The magnitude of the equilibrium force increases while the film becomes thinner. “When the film is very thin, this attractive force between the liquid molecules and the solid surface act to pull liquid into the layer as if the pressure in the layer were reduced below the ambient pressure by an amount of P_d, which is known as the disjoining pressure ”[44].

One of the most clear physical explanation of the disjoining pressure was made by Carey [44] considering a model system consisting of a hemispherical housing with a trapped bubble of gas. As it can be seen from Figure 2.1, the liquid does not wet the inside of the housing. Moreover, the pressure of the gas in the housing is kept constant by a connected tube. In this model system, the hemispherical housing is submerged in a liquid film which is in contact with and fully wets the horizontal solid wall. When the housing is brought very close to the solid surface, the gas pressure inside the hemispherical housing becomes greater than the sum of the ambient pressure and the hydrostatic liquid pressure of the liquid film. The difference in the pressure values is equal to the disjoining pressure. In the absence of the additional pressure which is equal to disjoining pressure, the pressure of the gas in the hemispherical housing cannot be adequate to sustain the thin film thickness between solid wall and housing, and the system should maintain a thicker film at this place.

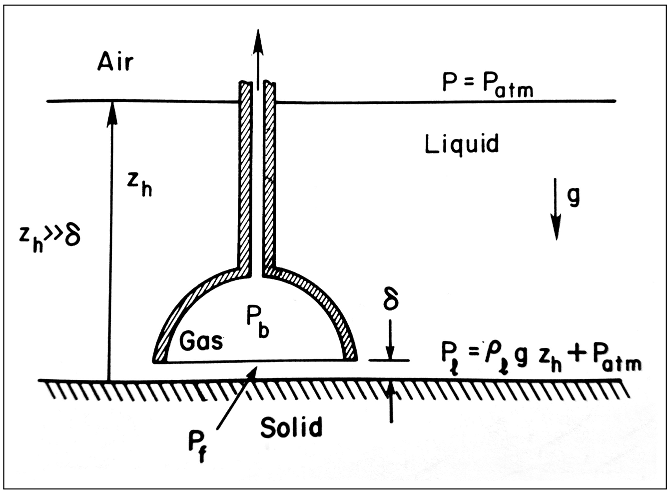

Figure 2.1: The model system used in [44]

Disjoining pressure, on the other hand, can also be defined in terms of the free energy of the liquid film. Derjaguin and Obuchov [45] described the disjoining pressure as the change of free energy with thickness and defined it as in Equation 2.3,

$$\gamma = \gamma_0 + \int_h^\infty P_d \, dh, \tag{2.3}$$

where γ is the specific surface free energy of the thin liquid film, γ_0 is the specific surface free energy of an infinitely thick film and h is the thickness of the layer.

A more general formulation of disjoining pressure was made by Derjaguin and Scherbakov [46] in Equation 2.4 in terms of the chemical potential of molecules and the total free energy, w, of the thin film,

$$R\,T\,\ln\left(\frac{P}{P_s}\right) = V\frac{\partial w}{\partial h}\,, \tag{2.4}$$

where, V is the molar volume of the liquid, P is the vapor pressure in equilibrium with thin film and P_s is the saturated vapor pressure at temperature T. The change in the total free energy of the system with respect to the height of the film thickness is the disjoining pressure,

$$P_d = -\frac{\partial w}{\partial h}^{*}\,, \tag{2.5}$$

Then, reduction of vapor pressure on the surface of equilibrium thin film can be defined by Equation 2.6.:

$$R\,T\,\ln\left(\frac{P}{P_s}\right) = V P_d. \tag{2.6}$$

It should be noted that the minus sign at the right side of Equation 2.6 is dropped because disjoining pressure is assumed to be negative by definition and with a minus sign, the value becomes positive. In order to overcome this confusion of sign, disjoining pressure is taken as positive without multiplication by the minus sign in the formulations.

In 1957, Derjaguin and Zorin [10] conducted an experimental work for the planar thin films of various liquids which were absorbed on smooth glass from their vapor phase. The apparatus used in the experiments can be seen in Figure 2.2. The liquid whose vapor adsorption was to be studied, was frozen in the bottom of the test tube, kept at a constant temperature T_2. The plate on which adsorption would take place, was kept at a constant temperature T_1. In order to maintain the relative pressures P/P_s with an accuracy of 0.001 to 0.002, the difference between T_1 and T_2 was set with accuracy an of 0.01°C.

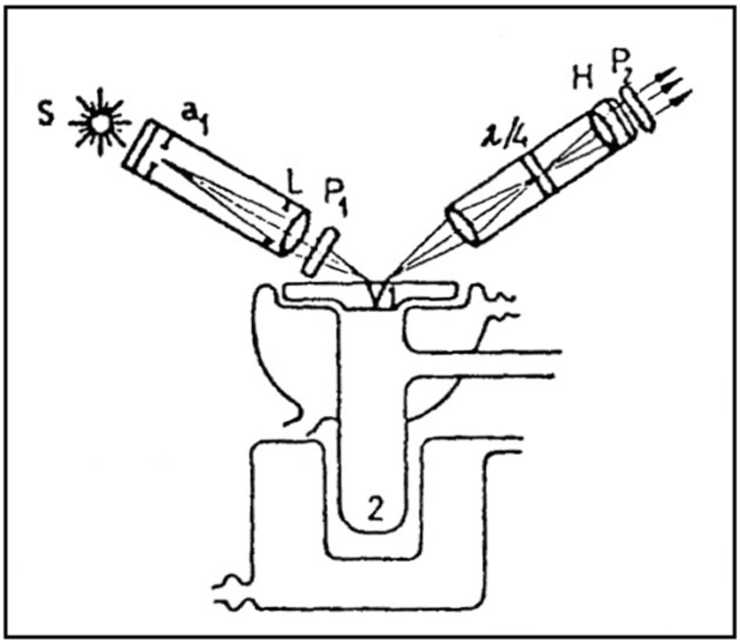

Figure 2.2: Apparatus used in the study of Derjaguin and Zorin [10]

In the experiments, adsorption isotherms of polar and non-polar liquids showed different trends. The adsorption isotherm of polar liquids (water, alcohols, nitrobenzene) intersected the saturation ordinate. This behaviour could be represented only by an exponential relation. Non-polar liquids (carbon tetrachloride, benzene), on the other hand, had the saturation ordinate as their asymptote enabling it to be represented by a power relation. The data of non-polar liquids collected during the experiments was led to the derivation of the famous power representation of non-polar liquids,

$$P_d = \frac{A_d}{\delta^3}\,, \tag{2.7}$$

where A_d is the dispersion constant which takes different values according to the type of the non-polar liquid and the solid plate on which liquid film exists. The sign of the dispersion constant is positive for wetting systems and negative for non-wetting systems.

A negative disjoining pressure, on the other hand, acts in an opposite manner with respect to a positive one. Its definition should be conjoining pressure rather than disjoining pressure. Following this idea, Starov [47] suggested to name this pressure as Derjaguin's pressure and use this name in his studies.

In a later study of Derjaguin [48], the use of Equation 2.7 was restricted to thin films thinner than 20 nm. An inverse quartic relationship was recommended to describe retarded interactions for thicker films.

For polar liquids, on the other hand, Derjaguin [49] developed a modified expression in 1985,

$$P_d = \frac{A_d}{\delta^3} + Ke^{-\delta/l}, \tag{2.8}$$

where constants K and l could take the values of 3×10^7 Pa and 8×10^{-10} m, respectively, when pure water on quartz glass was studied.

Other examples of disjoining pressure expressions for polar liquids can be found in various studies in literature such as Holm and Goplen [16] or Khrustalev and Faghri [50]. Generally, these expressions were developed by fitting a curve to the experimental data of Derjaguin and Zorin [10].

2.2.2 Application of Disjoining Pressure on Curved Surfaces

The effect of disjoining pressure becomes apparent when the film is sufficiently thin. In the capillary cooling devices, such as heat pipes, the interface of liquid and gas phases is curved near the presence of a solid boundary. This intersection of the three phases has various names in the literature such as contact line, triple line or triple contact line. In the close proximity of a contact line, disjoining pressure is effective due to very thin values of the film height. The presence of disjoining pressure leads to deviations from the undisturbed perfect circular meniscus shape. When the liquid-solid system is wetting, the value of the disjoining pressure is positive. It means that the film resists further thinning by the amount of disjoining pressure. In Figure 2.3, the interface of the liquid and gas phases are represented by three curves. The first curve is the part of the interface where the effect of the disjoining pressure is small due to high film thickness resulting in no significant deviation from the original circular geometry. This section is generally called the intrinsic meniscus in the literature. The second curve is the extension of the first one when the effect of disjoining pressure is not included. When the film thickness becomes sufficiently small, the curve deviates from its original shape as described by the third curve.

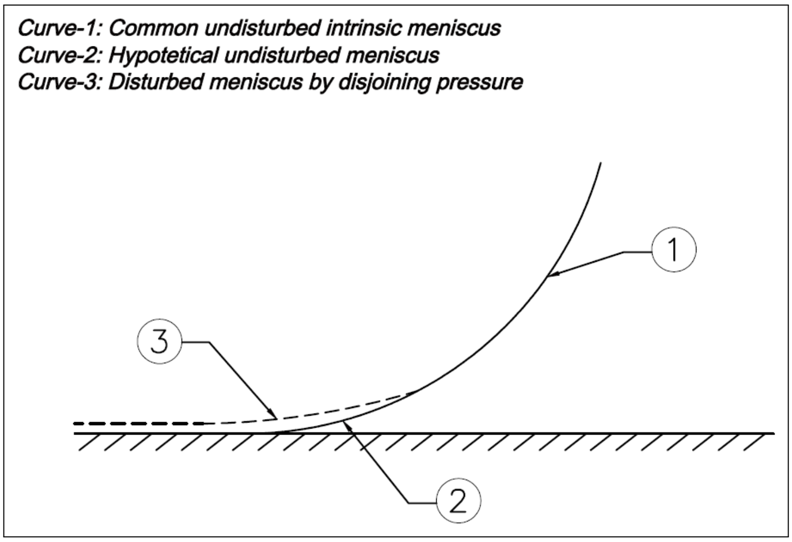

Figure 2.3: Deformation of a meniscus with the presence of disjoining pressure

The example in Figure 2.3 clearly points out that disjoining pressure must be present in the interface force balance when the film thickness is small. The classic Young-Laplace equation which defines the force balance at the curved surface then should be modified by the disjoining pressure. When the liquid-solid system is wetting, the positive disjoining pressure acts against the vapor pressure. The balance of the pressures can be seen in Figure 2.4.

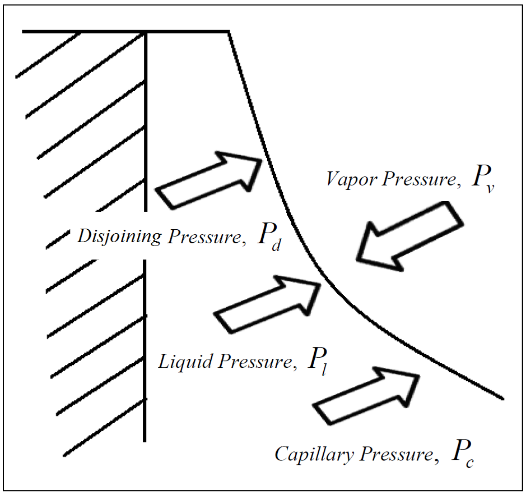

Figure 2.4: Pressure balance at the liquid-vapor interface

The modified version of the Young-Laplace equation by the addition of the disjoining pressure, is known as the augmented Young-Laplace equation given in Equation 2.9.:

$$P_v - P_l = P_c + P_d. \tag{2.9}$$

In spite of the common usage of the classic disjoining pressure formulations in the pressure balance of curved surfaces, it should be kept in mind that derivations of the disjoining pressure formulas were made based on experiments which studied the planar films. Almost all of the authors who use disjoining pressure correlations in curved films, state that the studied problem includes low film slopes.

If the liquid profile is moderately inclined, the application of disjoining pressure correlations becomes questionable. In his study published in 2010, Starov [47] claims that the non-zero contradictory equilibrium contact angle which appeared in the study of Miller and Ruckenstein [51], was due to moderate film slopes. On the other hand, the study of Stephan and Busse [31] had moderate slopes but the authors stated no problem arising from the utilization of classic disjoining formulation. In a recent study, Biswal *et al.* [52] used a slope and curvature dependent disjoining pressure correlation developed by Wu and Wong [53]. Unfortunately, the applications of slope and curvature dependent disjoining pressure correlations for different solid-liquid systems require the determination of a separate corresponding correlation constants for each solid-liquid systems. To determine these constants, a comprehensive experimental study should be carried out. Without such experimental study and set of data, the slope and curvature dependent disjoining pressure correlations cannot be applied to the practical problems.

2.3 Problem Definition

In the current study, heat pipes with a grooved wicking structure are going to be studied. Cross-section of the grooves which will be studied, is selected as rectangular for the computational advantage. The cross-section of a heat pipe with rectangular grooves, can be seen in Figure 2.5.

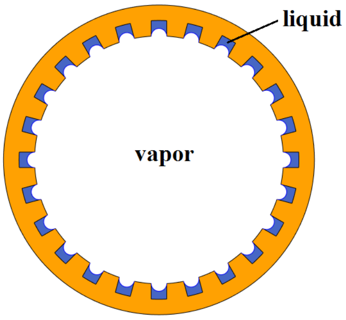

Figure 2.5: Cross-section of a grooved heat pipe

Micro grooves located on the periphery of the inner wall, serve as liquid arteries that carry the condensed liquid to the evaporator where the heat pipe is in contact with the device which is desired to be cooled. The evaporator region can also be called as the heat source of the heat pipe. In the middle cavity of the heat pipe, the vapor phase which forms in the evaporator, flows to the condenser section of the heat pipe due to gas pressure gradient. In the condenser section which is the cold end of the heat pipe (and also called as the heat sink of the heat pipe), the vapor phase condenses into liquid. Thus, heat pipe completes its self operating cycle.

Considering the high number of grooves in the periphery, fluid flow and heat transfer problem in a single rectangular groove is analyzed. Due to symmetry with respect to the channel mid-plane, only half of this geometry is chosen as the problem domain with symmetrical boundary conditions as shown in Figure 2.6.

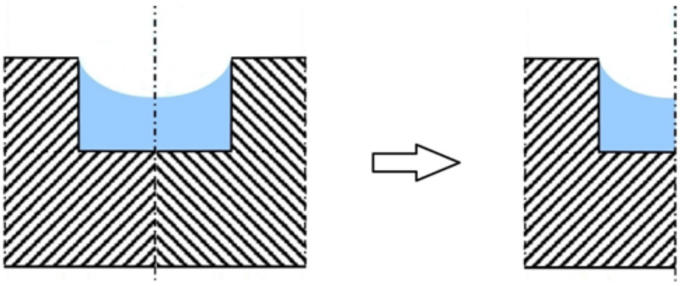

Figure 2.6: Cross-section of the single groove

The geometrical parameters and the coordinate system of the problem domain where the problem will be formulated, can be seen in Figure 2.7. The transverse y is defined between the side wall of the groove to the center of the groove. The x-coordinate is parallel to the side wall.

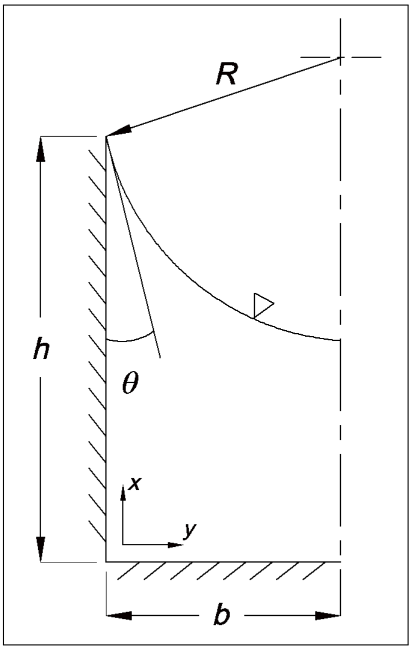

Figure 2.7: Groove geometry

Dimensions of the groove geometry studied in this thesis, are listed in Table 2.1.

Table 2.1: Dimensions of the groove geometry

Groove depth (μm)	h	1711.6
Groove half width (μm)	b	855.8
Apparent contact angle ($^\circ$)	θ	19.7
Intrinsic interface radius (μm)	R	909

Due to forces of adhesion between the wall and the wetting liquid, the meniscus attaches to the top of the groove as shown in Figure 2.7. It is assumed that there is always sufficient liquid in the heat pipe enabling the meniscus to remain attached to the top of the groove. Thus, dry-out situation or corner flow is not considered in this work. Resulting profile of the liquid along the groove can be seen in Figure 2.8 where the z-coordinate of the problem is taken along the axis of the groove.

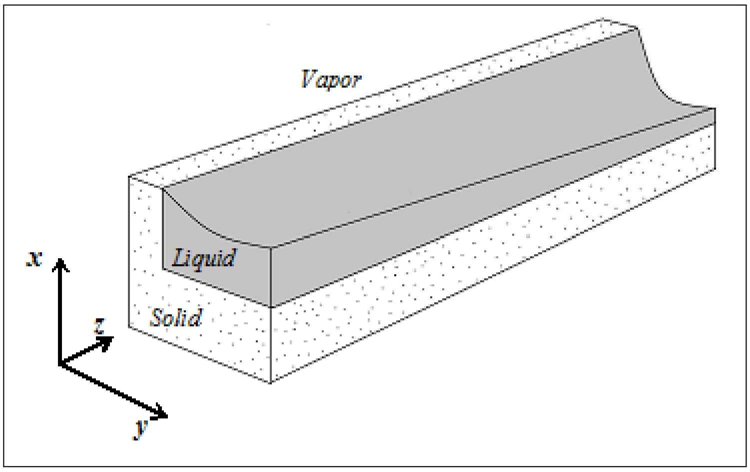

Figure 2.8: Liquid profile along the groove of heat pipe [43]

The curvature of the meniscus adjusts itself in order to counterbalance the pressure losses in the liquid and vapor phases. In the evaporator section, the amount of liquid decreases due to evaporation, resulting in a decrease in the radius of curvature. On the other hand, radius of curvature increases due to increased amount of liquid filled in the groove because of the condensation of vapor in the condenser. The variation in the radius of curvature along the heat pipe generates a pressure gradient in the liquid forcing the liquid flow towards the evaporator.

In this study, only the evaporator side of the heat pipe is investigated. The flow along the heat pipe, which is assumed to be fully developed, laminar, steady and incompressible, is coupled with evaporation from the liquid-vapor interface in order to develop a comprehensive three directional evaporation model.

Near the intersection point of the side wall and meniscus, a region exists with very small liquid thickness. The low thermal resistance across this thin film enables high heat transfer rates. The majority of evaporation takes place in this region. Therefore, most of the evaporation models in the literature only consider this extended meniscus region. With the increasing effect of disjoining pressure which will be discussed in the following chapter in detail, the interfacial line bends and the meniscus is stretched. Extended meniscus is practically divided into three regions with different characteristics as shown in Figure 2.9. Meniscus (intrinsic meniscus) or bulk region is the region where disjoining forces are negligible and fluid flow is only due to the change in the curvature of the meniscus. In the evaporating thin film region fluid flow is maintained by both capillary and disjoining forces and very high heat flux values are achieved due to ultra-thin thickness of the film. Non-evaporating region, on the other hand, is characterized by very high disjoining pressure which prevents evaporation. Evaporating thin film region and non-evaporating region is generally called as micro region in the literature.

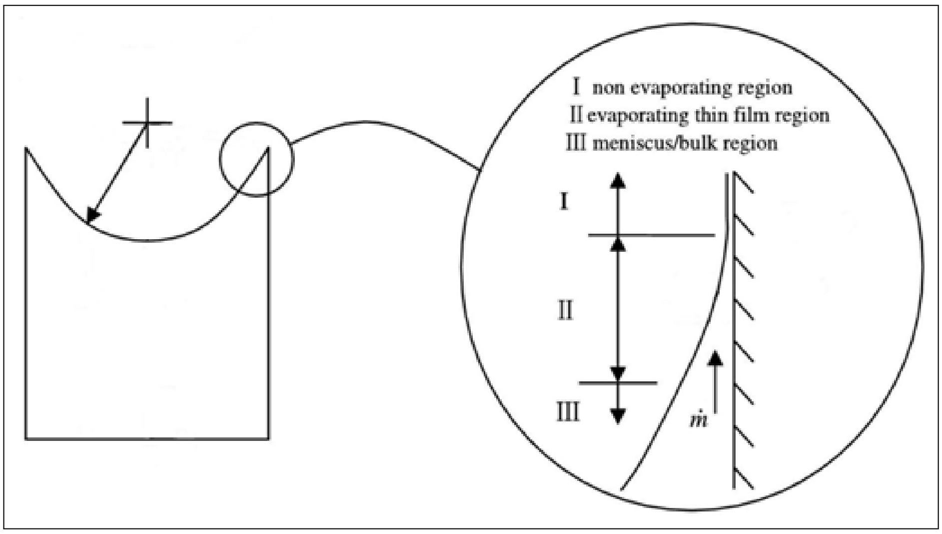

Figure 2.9: Extended meniscus

As the major part of the evaporation occurs in the thin film region, the evaporation model to be developed is based on this region.

2.4 Outline of the Thesis

Modelling of evaporation in the micro region starts with the analysis of flow in an arbitrary cross-section along the evaporator part of the heat pipe.

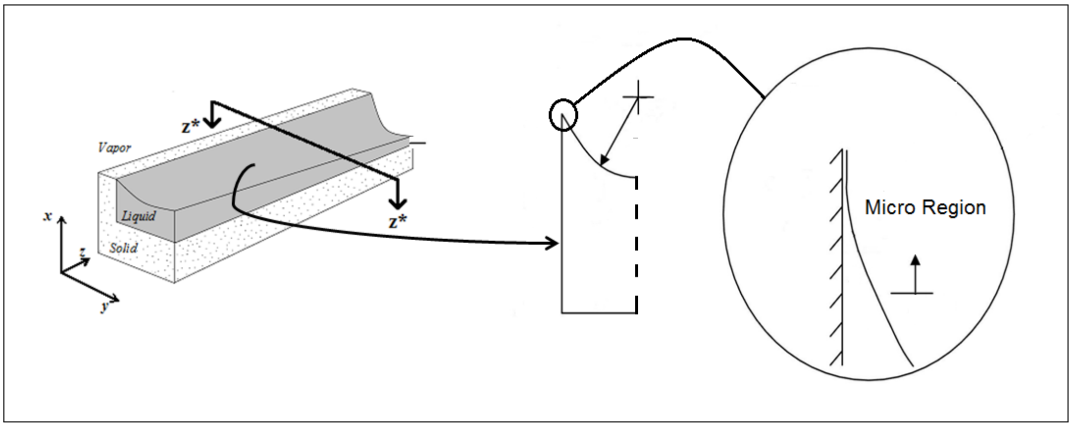

Figure 2.10: Micro region on an arbitrary cross-section

First, evaporation is modelled based on the u velocity as shown in Figure 2.11. Unlike existing unidirectional flow based models in the literature, analysis starts at a point in the bulk meniscus region.

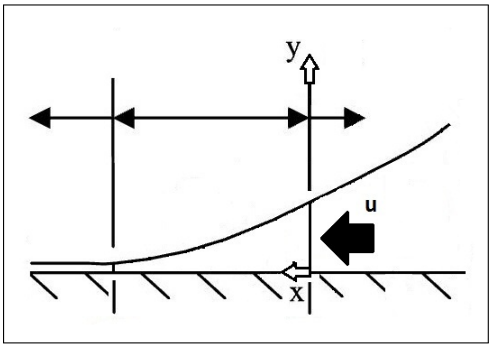

Figure 2.11: Unidirectional flow in the micro region

Second, evaporation is modelled based on both u and v velocities using spectral element method as shown in Figure 2.12. In this part, the results of the unidirectional flow based evaporation model are also applied to conserve the mass. The detailed solution process is summarized on a flow chart in Appendix A.

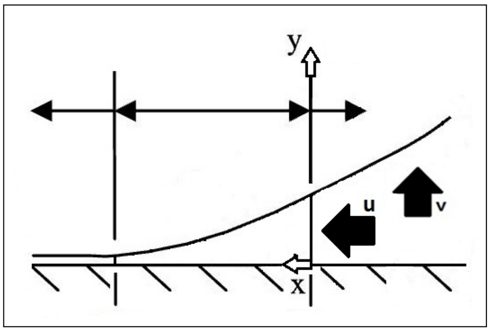

Figure 2.12: Bi-directional flow in the micro region

Last, the mass supply contribution of the fluid flow in the axial direction of the heat pipe is investigated by solving 2-D Poission's equation for axial velocity, w.

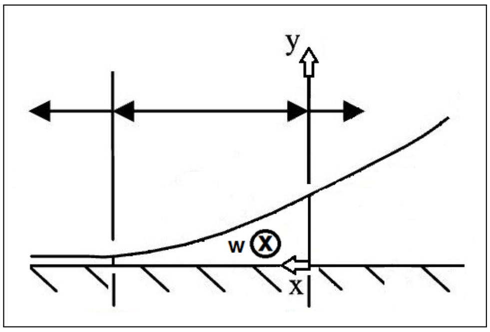

Figure 2.13: Axial flow in the micro region

At the end of the thesis, a parametric study is made using the developed model.

CHAPTER 3

EVAPORATION MODEL BASED ON UNIDIRECTIONAL FLOW

3.1 Theory of Evaporation

3.1.1 Evaporative Heat Flux from the Kinetic Theory of Gases

Evaporation is associated with high heat transfer coefficients. It enables to transfer high heat loads with small temperature differences so that heat pipes use the advantage of phase change heat transfer. Estimation of the limitation of heat transfer achieved by evaporation requires the investigation of the liquid-vapor interface at molecular level. Following the detailed study made by Carey [44] in his book, vapor molecules in the vicinity of liquid-vapor interface are going to be investigated, firstly.

In the kinetic theory of gases, Maxwell velocity distribution, formulated in Equation 3.1, is applied:

$$\frac{dn_{uvw}}{n} = \left(\frac{m}{2\pi k_B T}\right)^{3/2} \exp\Big(-(m/2k_B T)\left(u_m^2 + v_m^2 + w_m^2\right)\Big) du_m dv_m dw_m, \tag{3.1}$$

where n is total number of the molecules and the left side of the equation is the fraction of the total number of molecules having velocity between u and $u + du$, v and $v + dv$, w and $w + dw$ along x, y and z coordinates, respectively. In the right side of the equation, m, k_B and T are the mass of a gas molecule, Boltzman constant and absolute temperature, respectively.

In order to determine the flux of gas molecules which have a Maxwell velocity distribution through an arbitrary plane, the geometry depicted in Figure 3.1 is considered where L_x, L_y and L_z are dimensions of the box.

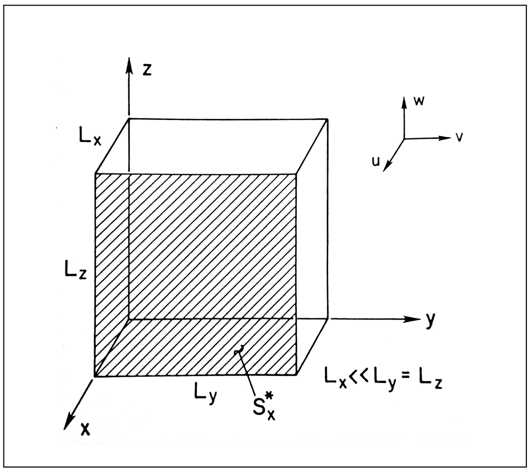

Figure 3.1: Geometry used in the analysis of molecular flux through a surface [44]

In this figure, the cross hatched surface is S_x^* and the amount of molecules within the box that will go through the surface S_x^* per unit time, is to be investigated. Regardless of the velocities v and w, the molecules which have a velocity component in the x direction, will pass through the S_x^* as long as they are located in a distance closer than $u\Delta t$. The fraction of the molecules having a velocity range between u and $U + du$ can be calculated using Maxwell velocity distribution as given in Equation 3.2,

$$\frac{dn_u}{n} = \int_v \int_w \frac{dn_{uvw}}{n} = \left(\frac{m}{2\pi k_B T}\right)^{1/2} e^{-mc^2/2k_B T} du. \tag{3.2}$$

The fraction of molecules which have u velocity and pass through to S_x^* per unit area and time, on the other hand, can be calculated considering the dimensions of the box:

$$dj_u = \left(\frac{u\Delta t}{L_x}\right) dn_u \left(\frac{1}{L_z L_y}\right)\left(\frac{1}{\Delta t}\right) . \tag{3.3}$$

When Equations 3.2 and 3.3 are combined and integrated for all possible values of u, the total rate at which molecules pass through S_x^* is found as shown in Equation 3.4,

$$j_u = \left(\frac{1}{4}\right)\left(\frac{n}{V}\right)\left(\frac{8k_BT}{\pi m}\right)^{1/2} = \left(\frac{M}{2\pi R_u}\right)^{1/2} \frac{P}{mT^{1/2}} . \tag{3.4}$$

Equation 3.4 shows that the flux in x direction is independent of any other dimension. Then, Equation 3.4 can be generalized to be used for any planar surfaces in a gas volume,

$$j_n = \left(\frac{1}{4}\right)\left(\frac{n}{V}\right)\left(\frac{8k_BT}{\pi m}\right)^{1/2} = \left(\frac{M}{2\pi R_u}\right)^{1/2} \frac{P}{mT^{1/2}} . \tag{3.5}$$

Equation 3.5, now, can be used to analyze the motion of the vapor molecules in the close proximity of a liquid-vapor interface. Let's assume a planar surface which is parallel to interface and located in an infinitesimally distance from the interface. The evaporation process requires that the number of vapor molecules that just escaped from the liquid phase must be greater than the number of vapor molecules merging with the liquid phase. Thus, the net evaporation rate is the difference between the flux of vapor molecules evaporated and the flux of vapor molecules condensing:

$$\dot{m}''_{evap} = m''_l - m''_v . \tag{3.6}$$

Flow rate of vapor molecules stated in Equation 3.5 was derived for stationary gases. However, the relation must be corrected for gases which have a bulk velocity. Vapor molecules which originate from bulk vapor phase and condensing on the liquid surface, have bulk velocity when crossing the planar surface which is just above the interface. Then, the relation for the flux of molecules is modified by a correction factor, Γ, as suggested by Schrage [13],

$$j_{nw} = \Gamma(a^*) \left(\frac{M}{2\pi R_u T} \right)^{1/2} \frac{P}{m} \ . \tag{3.7}$$

The definition of the correction factor, Γ, is given in Equation 3.8:

$$\Gamma(a^*) = \exp\big((a^*)^2\big) + a^* \pi^{1/2} \big(1 + \mathrm{erf(a^*)}\big). \tag{3.8}$$

If the bulk velocity of the vapor molecules which moves toward to the liquid is taken as w_0, the definition of a^* becomes,

$$a^* = \frac{w_0}{(2R_u T/M)^{1/2}} \ . \tag{3.9}$$

The molecules which are vaporized from the liquid phase, on the other hand, have negligible velocity due to infinitesimally small distance of the planar surface from the interface. Thus, Equation 3.5 is used to describe the flow rate of these vapor molecules.

In addition to the bulk velocity correction, reflection correction should also be considered in the flow rate of vapor molecules. For example, all the vapor molecules moving away from the interface do not have to be vaporized from the liquid phase. Some of them are molecules reflected from the interface because vapor molecules which hit the interface sometimes do not condense and are reflected from the interface. Similarly, the correction is necessary for vapor molecules which move towards the interface. Only some of the molecules actually condense and others are reflected. The correction factor for both cases are assumed to be the same and generally called as the accommodation coefficient, $\hat{\sigma}$.

Moreover, to determine the net mass flux at the interface, flow rates of the molecules have to be multiplied by the mass of a vapor molecule, m,

$$\dot{m}''_{evap} = m\hat{\sigma} \left(j_n - j_{nw} \right). \tag{3.10}$$

Substitution of Equation 3.5 and 3.7 to 3.10 yields the following relation for the evaporative mass flux at the interface,

$$\dot{m}''_{evap} = \hat{\sigma} \left(\frac{M}{2\pi R_u} \right)^{1/2} \left(\frac{P_{v,lv}}{T_{lv}^{1/2}} - \frac{\Gamma(a^*) P_v}{T_v^{1/2}} \right), \tag{3.11}$$

where P_l and P_v are the saturation pressures corresponding to the temperatures of liquid, T_l, and bulk vapor phase, T_v, respectively.

The magnitude of velocity correction factor, Γ, depends on the magnitude of a^*. To estimate the magnitude of a^*, the bulk velocity of vapor molecules at the interface has to be determined. At the interface, continuity of the vapor molecules requires the following relation for the vapor velocity,

$$w_0 = \frac{\dot{m}''_{evap}}{\rho_v} \ . \tag{3.12}$$

With the substitution of Equation 3.12 to 3.9, the relation for the a^* becomes as follows,

$$a^* = \frac{\dot{m}''_{evap}}{\rho_v} \left(\frac{2 R_u T_v}{M} \right)^{1/2} . \tag{3.13}$$

The value of a^* is small for the evaporation processes at high temperatures. In the limit of small a^*, velocity correction factor can be simplified to

$$\Gamma = 1 + a^* \pi^{1/2} \ . \tag{3.14}$$

Substituting Equation 3.14 with 3.13 to 3.11, using the ideal gas relation and rearranging terms, the evaporative mass flux at the liquid-vapor interface is reduced to Equation 3.15,

$$\dot{m}''_{evap} = \left(\frac{2\hat{\sigma}}{2 - \hat{\sigma}} \right) \left(\frac{M}{2\pi R_u} \right)^{1/2} \left(\frac{P_{v,lv}}{T_{lv}^{1/2}} - \frac{P_v}{T_v^{1/2}} \right). \tag{3.15}$$

This useful formulation is commonly attributed to the Schrage [13] in the studies which focus on the topic of thin film evaporation. In the Soviet literature, on the other hand, Equation 3.15 is referred as the Kucherov-Rikenglaz equation.

3.1.2 The Equilibrium Pressure Difference at the Liquid-vapor Interface

The equilibrium pressure difference at the liquid-vapor interface is related to the temperature difference between phases and surface forces at the interface. The relationship between equilibrium temperature and vapor pressure is obtained from the Clasius-Clapeyron equation. The surface forces which determine the shape of the interface, are capillary and disjoining forces. Modified Kelvin equation is applied to relate these forces to the pressure jump at the interface.

3.1.2.1 Clapeyron effect

Mathematical expression for the Clasius-Clapeyron equation can be shown in Equation 3.16,

$$\frac{dP}{dT} = \frac{h_{lv}}{\Delta v}\frac{1}{T}\ . \tag{3.16}$$

Transition between gas and liquid phase occurs at temperatures much lower than the critical temperature. In this case, the specific volume of the gas phase is much larger than that of the liquid phase. Thus, the difference between the specific volume of the phases can be approximated to the specific volume of gas phase,

$$\Delta v = v_g\left(1 - \frac{v_l}{v_g}\right) \approx v_g. \tag{3.17}$$

Furthermore, assuming low pressure, vapor can be approximated by the ideal gas law,

$$v_g = \frac{R_u}{M}\frac{T}{P}. \tag{3.18}$$

With the substitution of Equation 3.17 and 3.18, the relation of Clasius-Clapeyron for the ideal gases becomes as follows,

$$\frac{dP}{dT} = \frac{P}{T^2}\frac{h_{lv}M}{R_u}. \tag{3.19}$$

Equation 3.19, then, is integrated between the states of the bulk vapor and the vapor infinitesimally above the interface,

$$\ln\left(\frac{P_{v,lv}}{P_v}\right) = \frac{h_{lv}M}{R}\left(\frac{1}{T_v} - \frac{1}{T_{lv}}\right). \tag{3.20}$$

Taylor series expansion of the left side of Equation 3.20 yields Equation 3.21:

$$\left(\frac{P_{v,lv}}{P_v}\right) - 1 = \frac{h_{lv}M}{R}\left(\frac{1}{T_v} - \frac{1}{T_{lv}}\right). \tag{3.21}$$

After algebraic manipulations, the pressure difference of vapor at the interface is expressed as a function of superheat,

$$P_{v,lv} - P_v = \frac{h_{lv}MP_v}{R\,T_{lv}\,T_v}\,(T_{lv} - T_v). \tag{3.22}$$

3.1.2.2 Curvature effect

The change in vapor pressure due to a curved liquid-vapor interface, is expressed by the Kelvin equation:

$$\ln\left(\frac{P_{v,lv}}{P_v}\right) = -\frac{M}{\rho_l R T_{lv}}P_c. \tag{3.23}$$

When the evaporating film is thin enough, however dispersion forces start acting on the interface shape in addition to the capillary force. In his study published in 1970, Padday [12] stated that the disjoining pressure and curvature is additive on the film vapor pressure and he suggested the modified Kelvin equation in the calculation of vapor pressures of evaporating thin films,

$$\ln\left(\frac{P_{v,lv}}{P_v}\right) = -\frac{M}{\rho_l R_u T_{lv}}(P_c + P_d). \tag{3.24}$$

Taylor series expansion of the left side of Equation 3.24 yields Equation 3.25,

$$\frac{P_{v,lv}}{P_v} - 1 = -\frac{M}{\rho_l R_u T_{lv}}(P_c + P_d). \tag{3.25}$$

Equation 3.25 can be arranged to express the pressure difference of vapor at the interface as a function of capillary and disjoining pressures,

$$P_{v,lv} - P_v = -\frac{V_l P_v}{R_u T_{lv}}(P_c + P_d), \tag{3.26}$$

where V_l is the molar volume of the liquid.

3.1.3 Evaporation Model of Wayner

In the evaporation process taking place in an extending meniscus, Wayner *et al.* [14] suggested the following relation assuming small superheat values:

$$T_{lv}^{1/2} \approx T_v^{1/2}. \tag{3.27}$$

With this simplification, evaporative mass flux at the interface reduces to a function of pressure difference between bulk vapor phase and the vapor just above the interface,

$$\dot{m}''_{evap} = \left(\frac{2\hat{\sigma}}{(2-\hat{\sigma})}\right)\left(\frac{M}{2\pi R_u T_v}\right)^{1/2}(P_{v,lv} - P_v). \tag{3.28}$$

The pressure difference arises from the additive effects of superheat, curvature and dispersion forces as explained above. Then, Equation 3.28 can be written as a function of them,

$$\dot{m}''_{evap} = \frac{2\hat{\sigma}}{2-\hat{\sigma}}\left(\frac{M}{2\pi R_u T_v}\right)^{1/2}\left(\frac{h_{lv} M P_v}{R T_{lv} T_v}(T_{lv} - T_v) - \frac{V_l P_v}{R_u T_{lv}}(P_c + P_d)\right). \tag{3.29}$$

Following Wayner *et al.* [14], Equation 3.29 is simply expressed in the form of Equation 3.30 in the literature,

$$\dot{m}''_{evap} = a\left(T_{lv} - T_v\right) - b\left(P_c + P_d\right), \tag{3.30}$$

where

$$a = \frac{2\hat{\sigma}}{2-\hat{\sigma}}\left(\frac{M}{2\pi R_u T_{lv}}\right)^{1/2}\left(\frac{M P_v h_{lv}}{R_u T_v T_{lv}}\right), \tag{3.30a}$$

$$b = \frac{2\hat{\sigma}}{2-\hat{\sigma}}\left(\frac{M}{2\pi R_u T_{lv}}\right)^{1/2}\left(\frac{P_v V_l}{R_u T_{lv}}\right). \tag{3.30b}$$

Furthermore, Moosman and Homsy [20] eliminated the interface temperature in favour of the wall temperature assuming simple conduction in the transverse direction. Thus, temperature jump or superheat is defined in terms wall and saturated bulk vapor temperatures as shown in Equation 3.31:

$$\dot{m}''_{evap} = \frac{1}{1 + a\delta h_{lv}/k_l}\Big(a(T_w - T_v) - b(P_c + P_d)\Big). \tag{3.31}$$

3.2 Unidirectional Fluid Flow in the Thin Film Region

As explained previously, the major contribution to evaporation occurs in the thin film region where both capillary and dispersion forces are effective. The formulation of unidirectional fluid flow with the evaporation will be based on this region. However, there is no distinct boundary which separates the thin film region from the intrinsic region where only capillary forces exist. Then, it would be safe to start the flow analysis from a place in the intrinsic meniscus region where the ratio of disjoining pressure to capillary pressure is sufficiently small.

The evaporation process taking place at the interface creates a pressure gradient which enables the supply of liquid from the bulk meniscus to the thin film region.

The necessary pressure gradient in the intrinsic meniscus region is generated due to the deformation of the curvature of the meniscus. To formulate the liquid pressure gradient at the interface of the intrinsic meniscus region, derivative of the Young-Laplace equation is used. It should be noted that Kelvin equation (Equation 3.23) reduces to Young-Laplace equation if the superheat between liquid and vapor phases is negligible. In the thin film region, on the other hand, disjoining pressure is also taken into account and derivative of the augmented Young-Laplace equation which is given in Equation 3.32, is used to find the liquid pressure gradient at the interface. It should be noted that the vapor pressure can be assumed constant for a heat pipe, which is indeed a closed container for the vapor phase, therefore, the gradient of vapor pressure can be neglected:

$$-\frac{dP_l}{dx} = \frac{dP_c}{dx} + \frac{dP_d}{dx} \ . \tag{3.32}$$

Assuming unidirectional flow in the x direction, the change of pressure in the y direction is neglected. Then, the liquid pressure gradient at the interface can be used for entire domain.

The radius of curvature, R, can be geometrically defined as follows,

$$R = \frac{\left(1 + (d\delta/dx)^2\right)^{3/2}}{d^2\delta/dx^2} \ , \tag{3.33}$$

where δ, is the film thickness at an x position. It should be noted that the above definition of radius of curvature, R, differs from the common definition, using absolute values of the second derivative, which renders the radius of curvature positive. The current definition, however, accounts for the change in the sign of capillary pressure due to a change in the sign of the second derivative, enabling mathematical formulation and solution of the problem.

When Equations 2.2, 2.7 and 3.33 are substituted to Equation 3.32, the liquid pressure gradient in the x direction can be formulated as in Equation 3.34 where the only unknown is the film thickness, δ,

$$-\frac{dP_l}{dx} = -\frac{3A_d}{\delta^4}\frac{d\delta}{dx} + \sigma\frac{d^3\delta/dx^3}{\left(1+(d\delta/dx)^2\right)^{3/2}} - 3\sigma\frac{\left(d^2\delta/dx^2\right)^2}{\left((1+(d\delta/dx)^2\right)^{5/2}}\frac{d\delta}{dx} \ . \quad (3.34)$$

At the end of the thin film region, a non-evaporating region exists where the evaporation is suppressed due to low film pressure caused by very high disjoining pressures. The non-evaporated stationary block of liquid behaves like a solid. Then, all of the liquid entering the thin film region must evaporate until non-evaporating region to satisfy conservation of mass. For the momentum, on the other hand, x component of the Navier-Stokes equation should be solved because of unidirectional fluid flow assumption. Heat pipes have capillary pressure driven flows with very low velocities. Physics of the flow is based on balance of pressure forces originating from capillary effect and viscous forces originating from shear between liquid and solid boundaries. Furthermore, many heat pipes can work against gravity in earth applications or they can work in micro gravity applications in space. Thus, body forces do not play an effective role in the flow mechanism depending on the relative magnitude of capillary forces. Then, applying boundary layer approximations, x momentum equation can be simplified to Equation 3.35:

$$\frac{dP_l}{dx} = \mu\frac{d^2u}{dy^2} \ . \quad (3.35)$$

Equation 3.35 is integrated twice to get the u velocity distribution at an x location depending on the value of liquid pressure gradient at this position. The integration constants are determined using boundary conditions at the wall surface and liquid-vapor interface. At the wall, no slip condition is applied. At the liquid-vapor interface, negligible shear stress between vapor and liquid is assumed. The resulting u velocity distribution can be seen in Equation 3.36:

$$u = \frac{1}{\mu}\frac{dP_l}{dx}\left(\frac{y^2}{2} - \delta y\right) \ . \quad (3.36)$$

The only unknown in Equation 3.36 is the film thickness. In order to find the distribution of the film thickness in the thin film region, domain is discretized using strips.

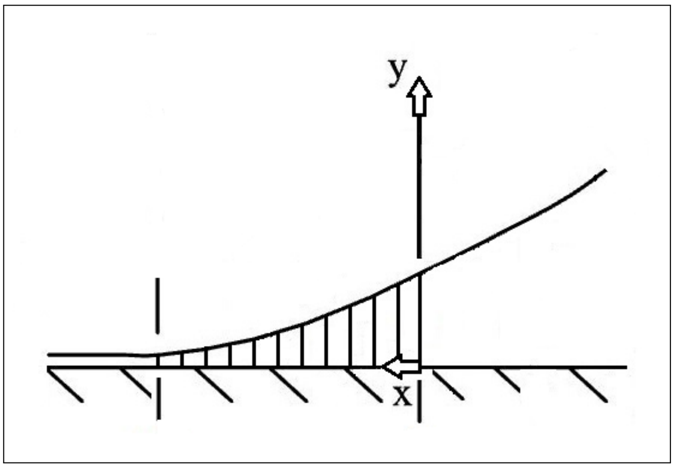

Figure 3.2: Solution domain

In each strip, conservation of mass is applied by equating the difference of inlet and outlet mass flow rates to the evaporative mass flow rate.

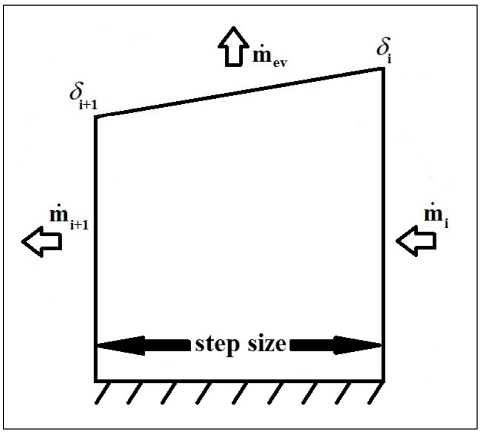

Figure 3.3: Mass conservation on a single strip

where

$$\dot{m}'_i = \rho_l \int_0^{\delta_i} u \, dy. \tag{3.37}$$

When the formulation of the u velocity is substituted in Equation 3.37, mass flow per unit depth is obtained as follows,

$$\dot{m}'_i = -\frac{1}{\nu}\frac{dP_l}{dx}\frac{\delta_i^3}{6} \ , \tag{3.38}$$

where mass flow per unit depth, m'_i, is only a function of film thickness, δ, due to the fact that dP_l/dx is function of δ.

In the solution procedure, initially the total mass flow rate entering the domain which is also equal to the amount of total evaporated fluid from the interface, is estimated. Analysis starts from an initial film thickness at which the ratio of disjoining pressure to the capillary pressure is negligible. In the first strip of the domain, the amount of fluid entering the strip is known. The amount of fluid exiting from the strip is a function of the thickness of the film at the end of the strip. The amount of fluid evaporating within the strip is a function of the average film thicknesses at the beginning and end of the strip. Then, the following relation is set to find the film thickness at the end of the first strip.

$$f(\delta_{i+1}) = \dot{m}'_i - \dot{m}'_{i+1}(\delta_{i+1}) - \dot{m}'_{evap}\left(\frac{\delta_i + \delta_{i+1}}{2}\right) = 0 \tag{3.39}$$

The step size of the numerical solution is set when the domain is divided to strips. This step size is used in the discretization of Equation 3.40 which is a 3^{rd} order, non-linear differential equation requiring three initial conditions set at the boundary. In the numerical solution of the equation, finite difference method is applied. During the solution procedure, secant method is used for root finding. At the end of the numerical solution performed on the first strip, the exit film thickness of the first strip is found. It is also the film thickness at the beginning of the second strip. Then, the same solution procedure is used for the second and successive strips. When all of the fluid is evaporated, the analysis is stopped and the liquid pressure gradient is checked. If the liquid pressure gradient is different than zero, the guess of the total amount of the fluid entering to the domain, is updated. Iterations are continued until the point on which liquid pressure gradient vanishes, coincides with the point where all of the fluid is evaporated.

3.3 Boundary Conditions

In the studies in which the numerical solution of the governing differential equation is started from the intersection of the non-evaporating and evaporating thin film region ([31], [36], [41], [54], [55]), thickness and first three derivatives of the film have to be specified. Equation 3.30 is set to zero to find the thickness at the edge of the non-evaporating region. The first derivative of the film thickness is taken as zero for spreading fluids. The second derivative of the film thickness is zero due to zero curvature assumption at the contact line. Third derivative of the film thickness, on the other hand, can be expressed as functions of the film thickness and first two derivatives from differentiation of the augmented Young-Laplace equation, Equation 2.9. However, in various studies these initial conditions are manipulated in different ways to overcome the numerical difficulties encountered. Stephan and Busse [31] calculated a non-evaporating film thickness thicker than the theoretical value and used a very small value for the second derivative of the film thickness by assuming very small capillary pressure instead of zero capillary pressure at the contact line. Moreover, they chose a suitable value for the third derivative of the film thickness so that the integration ended in a meniscus with the desired curvature. Wang *et al.* [36] chose a higher non-evaporating film thickness and non-zero first derivative. In addition, they manipulated the second derivative to match the far field boundary condition. Although the authors claim that such small alterations of the boundary conditions do not affect the results, this approach leads to a misrepresentation of underlying physical phenomena.

Furthermore, specifying boundary conditions at the contact line is not a reliable method especially for the systems which are subjected to large superheat because film thickness becomes extremely small thin in these systems. The shape of the contact line cannot be predicted in these systems due to the fact that there exists no experiment measuring such a thin film thickness which may be at the order of molecular separation.

Before presenting the boundary conditions used in this thesis, the contact angle should be discussed because apparent and real contact angles are frequently confused with each other. Generally, the term contact angle is used to represent the angle between the tangent line of the liquid-vapor and the solid at the triple intersection of solid-liquid-vapor. The contact angle which can be identified with the naked eye is called as apparent contact angle. The real contact angle, on the other hand, is the angle of the free surface at the junction of it with the adsorbed liquid. Real contact angle is sometimes at the level of surface roughness and it cannot be measured easily. In his study published in 1982 [23], Wayner stated that real contact angle is at the molecular level and cannot be seen. However, nearly all of the spreading systems were solved using the zero real contact angle as boundary condition without an exact experimental evidence. For example, the experimental results of Dasgupta *et. al* [26] could not show the real contact angle with the sufficient resolution but the analytical model based on the experimental results assumed zero real contact angle. For these reasons, instead of true contact angle at the contact line, apparent contact angle should be defined in a system.

In order to avoid the numerical difficulties and physical conflicts, in the current study, analysis starts from a place in the intrinsic meniscus region where the ratio of disjoining pressure to capillary pressure is sufficiently small.

Equation 3.39 is a third order differential equation requiring the specification of three initial conditions at the inlet of the solution domain. Integration is started at a location such that the effect of disjoining forces is negligible. The first derivative of the film thickness is calculated from the apparent contact angle, θ, the second derivative of the film thickness is calculated from Equation 3.33 based on the undisturbed meniscus curvature in the intrinsic meniscus region. The amount of fluid to be evaporated in the problem domain is unknown *a priori* to solution. This amount is found in an iterative manner so that when the entire amount of fluid entering the domain evaporates, film thickness reaches the non-evaporating thickness value at the end of the solution domain, where the film terminates. Note that the thickness of the non-evaporating film also an unknown *a priori*, and can only be obtained through the solution of the evaporation problem.

3.4 Results

Equation 3.39 is solved using the finite difference method with the physical data of the study of Stephan and Busse [31], where ammonia was the working fluid, given in Table 3.1.

Table 3.1: Physical parameters used in evaporation model

Vapor temperature (K)	T_v	300
Wall temperature (K)	T_w	301
Vapor pressure (Pa)	P_v	1.06×10^6
Density of saturated vapor (kg/m^3)	ρ_v	9
Density of liquid (kg/m^3)	ρ_l	600
Latent heat of evaporation (J/kg)	h_{lv}	1.18×10^6
Surface tension (N/m)	σ	2.0×10^{-2}
Dynamic viscosity of liquid (Pa $\cdot$ s)	μ_l	1.3×10^{-4}
Thermal conductivity (W/m $\cdot$ K)	k_l	0.48
Molar mass of liquid (kg/mol)	M	17.3×10^{-3}
Molar volume of liquid (m^3/mol)	V_l	28.8×10^{-6}
Accommodation coefficient	$\hat{\sigma}$	1
Dispersion constant (J)	A_d	2.0×10^{-21}
Initial film thickness (μm)	δ	0.282
Apparent contact angle ($^\circ$)	θ	19.7
Intrinsic interface radius (μm)	R	909

In the numerical solution, an adaptive step size reduction is used to resolve the physics of the problem near the contact line where peak heat flux values abruptly drop to zero. However, adequate resolution could not be achieved to distinguish the difference in numerical parameters between two successive steps. This is due to the insensitivity of the evaporative flux to film thickness. To overcome this problem, quadruple precision is used instead of double precision for the variables in the numerical calculation and convergence is achieved in the iterations.

Film thickness predictions of the current study and Stephan and Busse [31] are given in Figure 3.4. To explore the behaviour of the film thickness variation near the contact line, a blown up figure is also provided in Figure 3.4.

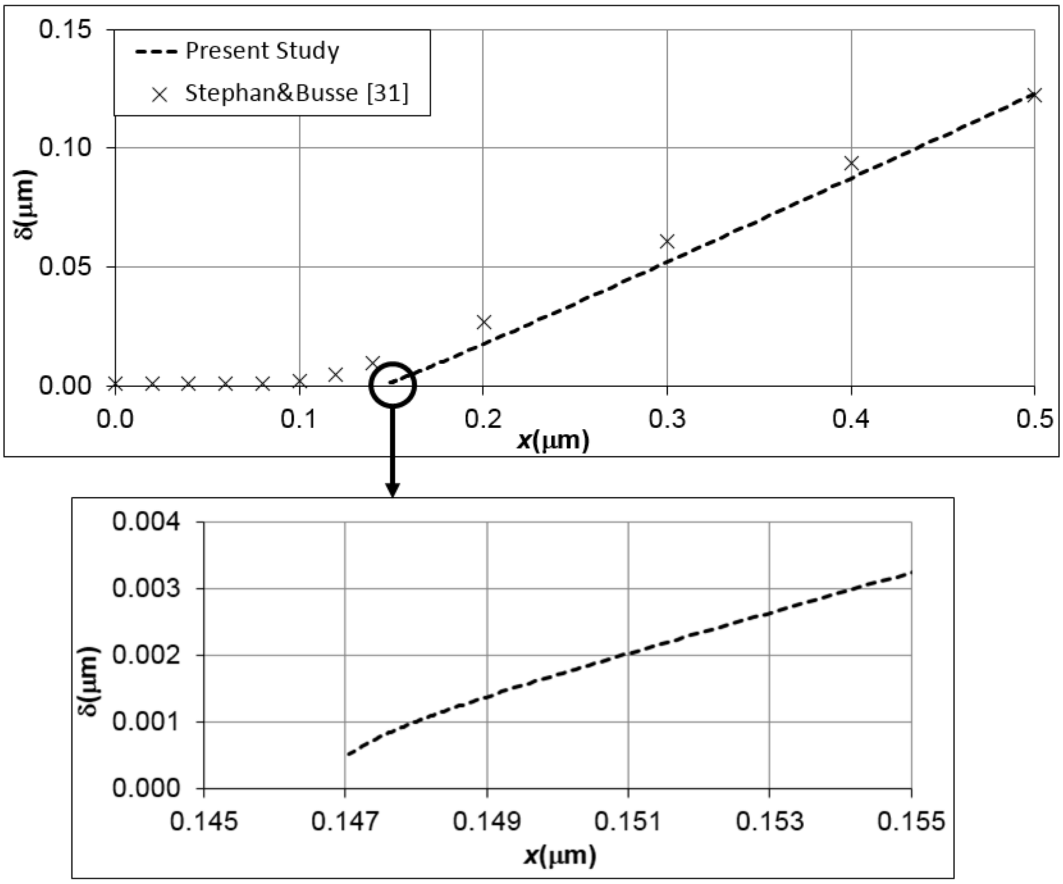

Figure 3.4: Film thickness variation of the current study and that of Stephan and Busse [31]

As shown in Figure 3.4, change in the curvature of the film thickness of the present study is less observable when compared with the film thickness of Stephan and Busse. Furthermore, when there is no enforced boundary condition, the second derivative of film thickness, δ, changes sign and bends inward near the contact line instead of asymptotically approaching zero. This behaviour can be explained by examining the pressure balance at the interface which is shown in Figure 3.5.

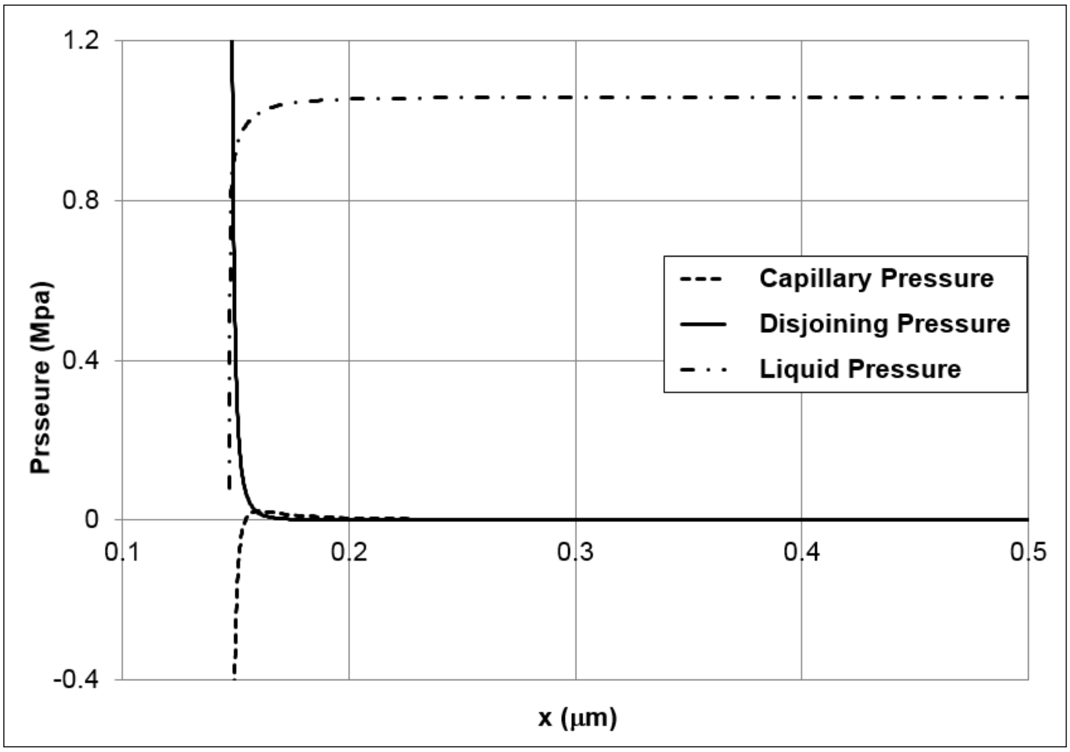

Figure 3.5: Variation of pressures

Augmented Young-Laplace equation, Equation 2.9, can be written to express the liquid pressure as follows,

$$P_l = P_v - (P_c + P_d), \tag{3.40}$$

where summation of capillary and disjoining pressures should not exceed the vapor pressure, otherwise absolute liquid pressure drops below zero which leads to a complete non-physical state. In order to prevent such a non-physical situation, rapidly increasing disjoining pressure should be somehow balanced. The sign change of the curvature creates a negative capillary pressure. This mechanism balances the rapidly increasing disjoining pressure due to ultra-thin film thickness values near the contact line. Thus, liquid pressure never drops below zero before the evaporation of all fluid entering the problem domain. However, in the absence of such a mechanism, the value of disjoining pressure exceeds 2.3 MPa at the contact line whereas the value of saturated vapor pressure is only about 0.1 MPa resulting a negative absolute pressure in the study of Stephan and Busse [31].

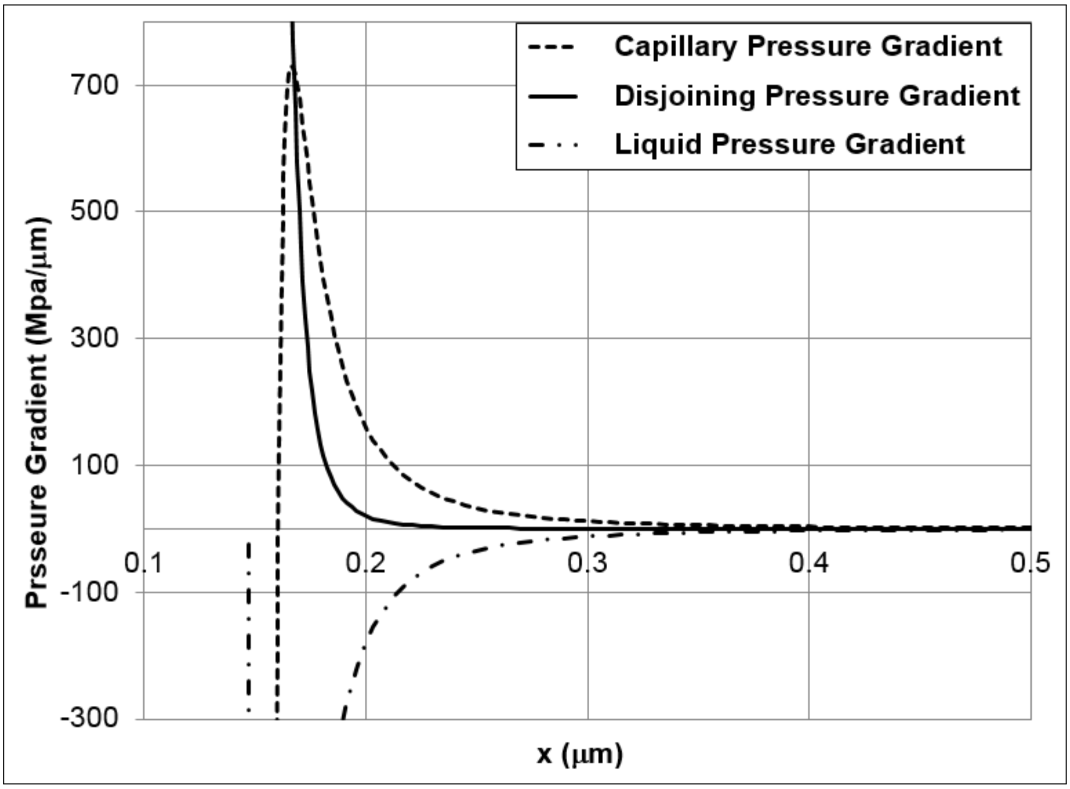

Figure 3.6: Contribution of capillary and disjoining pressures to liquid pressure gradient

In addition to a non-negative absolute liquid pressure value, the liquid pressure gradient at the end of the evaporating thin film must be zero because there is no fluid motion at the non-evaporating thin film zone where evaporation is suppressed by ultimately high disjoining pressure. Figure 3.6 shows the variation of the different contributions to pressure gradient within the evaporating thin film region and the liquid pressure gradient reaches zero at the contact line.

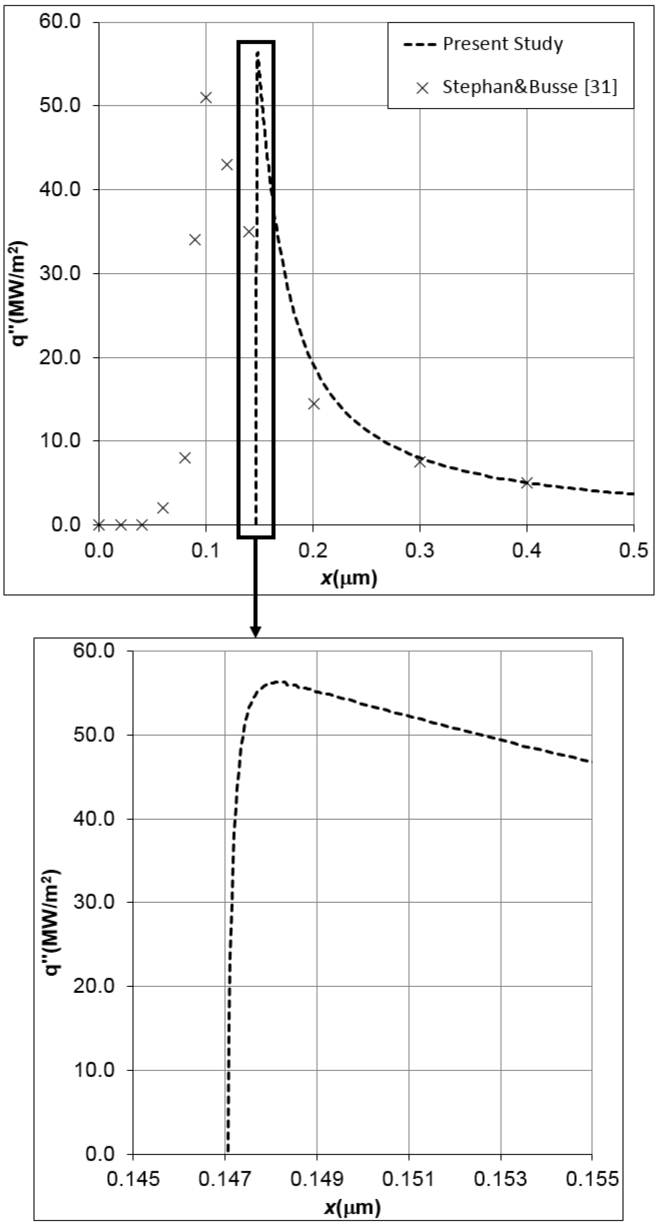

Figure 3.7: Heat flux variation of the current study and Stephan and Busse [31]

Figure 3.7 shows the variation of heat flux of the present and the reference studies in the thin-film region. Heat flux values of the present study match the values of Stephan and Busse [31] when the effect of disjoining pressure is small compared to the capillary pressure. However, for progressively small film thicknesses, heat flux of the present study increases more rapidly. After reaching the maximum value of the heat flux, which is 6% higher than the value reached in the study of Stephan and Busse [31], heat flux abruptly drops to zero. To get the adequate resolution for analysing this sudden decrease, excessively small step sizes are used in the numerical solution. The blown up plot in Figure 3.7, shows the resolved heat flux variation in the close neighbourhood of the maximum value of the heat flux.

The total heat transferred in the micro region ($0 \leq x \leq 1\,\mu$m) was reported as 6.6 W/m in the study of Stephan and Busse [31]. In the current study, starting the analysis with the same initial film thickness used in the study of Stephan and Busse [31], the total heat transferred is estimated as 5.38 W/m corresponding an 18.5% decrease in the total heat transferred.

CHAPTER 4

EVAPORATION MODEL BASED ON BI-DIRECTIONAL FLOW

4.1 Formulation

Although the assumption of unidirectional flow is generally applied to the micro region in the literature, a more general approach is necessary to get a comprehensive evaporation model. In the thin film region of an extended evaporating meniscus, both u and v velocities actually exist. Therefore, the y momentum equation should also be solved in addition to the x momentum, simultaneously. Moreover, conservation of mass within the solution domain should be guaranteed. The effect of gravity can be neglected as mentioned previously. Then, steady state, two-dimensional conservation of mass and linear momentum equations in Cartesian coordinates can be written as follows,

$$\frac{\partial u}{\partial x}+\frac{\partial v}{\partial y}=0, \tag{4.1}$$

$$u\frac{\partial u}{\partial x}+v\frac{\partial u}{\partial y}=-\frac{1}{\rho}\frac{\partial P}{\partial x}+\nu\Big(\frac{\partial^2 u}{\partial x^2}+\frac{\partial^2 u}{\partial y^2}\Big), \tag{4.2}$$

$$u\frac{\partial v}{\partial x}+v\frac{\partial v}{\partial y}=-\frac{1}{\rho}\frac{\partial P}{\partial y}+\nu\Big(\frac{\partial^2 v}{\partial x^2}+\frac{\partial^2 v}{\partial y^2}\Big). \tag{4.3}$$

Before starting the solution of governing equations, an order of magnitude analysis is applied to them. Unlike many studies in the literature, the solution of unidirectional model yielded moderate slope values instead of values which are very close to zero. Therefore film thickness and longitudinal distance cannot be compared to determine a scale for the order of magnitude analysis. On the other hand, the components of the surface velocity are suitable to be used in the order of magnitude analysis due to the fact that the geometry of the liquid-vapor interface was estimated in the solution of unidirectional model. For small contact angles, approximately less than 20°, the following can be used, due to the geometry of the contact line:

$$\frac{u_{lv}^{o}}{v_{lv}^{o}} > 1. \tag{4.4}$$

Non-dimensional parameters for the longitudinal direction, x, transverse direction, y, x velocity, u, and y velocity, v, can be defined as follows,

$$\bar{x} = \frac{x}{x^{o}}, \tag{4.5}$$

$$\bar{y} = \frac{y}{\delta}, \tag{4.6}$$

$$\bar{u} = \frac{u}{u_{lv}^{o}}, \tag{4.7}$$

$$\bar{v} = \frac{v}{v_{lv}^{o}}, \tag{4.8}$$

such that all dimensionless quantities are of the magnitude O(1).

Firstly, conservation of mass, Equation 4.1, is subjected to the order of magnitude analysis to determine a relation for the scale of longitudinal distance, x^{o}:

$$\frac{u_{lv}^{o}}{x^{o}}\frac{\partial \bar{u}}{\partial \bar{x}} + \frac{v_{lv}^{o}}{\delta}\frac{\partial \bar{v}}{\partial \bar{y}} = 0. \tag{4.9}$$

Since the dimensionless terms are of the O(1), the coefficients of the non-dimensional terms must be equal, and scale of longitudinal distance can be expressed as follows,

$$x^o = \delta \frac{u^o_{lv}}{v^o_{lv}}. \tag{4.10}$$

Before the order of magnitude analysis of conservation of linear momentum equations, the scale of absolute liquid pressure should be determined. However, when the comparison is made between the corresponding terms of the x and y momentum equations, finding a relation for the scale of the liquid pressure may not necessary. Thus, reference pressure, P^o, is used to make the absolute liquid pressure non-dimensional without an *a priori* definition,

$$\bar{P} = \frac{P}{P^o}. \tag{4.11}$$

Now, conservation of linear momentum equations can be non-dimensionalized,

$$\frac{u^o_{lv} v^o_{lv}}{\delta}\bar{u}\frac{\partial \bar{u}}{\partial \bar{x}} + \frac{u^o_{lv} v^o_{lv}}{\delta}\bar{v}\frac{\partial \bar{u}}{\partial \bar{y}} = -\frac{v^o_{lv} P^o}{u^o_{lv}\rho}\frac{\partial \bar{P}}{\partial \bar{x}} + \frac{(v^o_{lv})^2 \nu}{\delta^2 u^o_{lv}}\frac{\partial^2 \bar{u}}{\partial \bar{x}^2} + \frac{u^o_{lv}\nu}{\delta^2}\frac{\partial^2 \bar{u}}{\partial \bar{y}^2}, \tag{4.12}$$

$$\frac{(v^o_{lv})^2}{\delta}\bar{u}\frac{\partial \bar{v}}{\partial \bar{x}} + \frac{(v^o_{lv})^2}{\delta}\bar{v}\frac{\partial \bar{v}}{\partial \bar{y}} = -\frac{P^o}{\rho}\frac{\partial \bar{P}}{\partial \bar{y}} + \frac{(v^o_{lv})^3 \nu}{\delta^2 (u^o_{lv})^2}\frac{\partial^2 \bar{v}}{\partial \bar{x}^2} + \frac{v^o_{lv}\nu}{\delta^2}\frac{\partial^2 \bar{v}}{\partial \bar{y}^2}. \tag{4.13}$$

For simplicity, x momentum equation is multiplied by $\delta/u^o_{lv}v^o_{lv}$ and y momentum equation is multiplied by $\delta/(v^o_{lv})^2$,

$$\bar{u}\frac{\partial \bar{u}}{\partial \bar{x}} + \bar{v}\frac{\partial \bar{u}}{\partial \bar{y}} = -\frac{P^o}{(u^o_{lv})^2\rho}\frac{\partial \bar{P}}{\partial \bar{x}} + \frac{v^o_{lv}\nu}{\delta (u^o_{lv})^2}\frac{\partial^2 \bar{u}}{\partial \bar{x}^2} + \frac{\nu}{\delta v^o_{lv}}\frac{\partial^2 \bar{u}}{\partial \bar{y}^2}, \tag{4.14}$$

$$\bar{u}\frac{\partial \bar{v}}{\partial \bar{x}} + \bar{v}\frac{\partial \bar{v}}{\partial \bar{y}} = -\frac{P^o}{(v^o_{lv})^2\rho}\frac{\partial \bar{P}}{\partial \bar{y}} + \frac{v^o_{lv}\nu}{\delta (u^o_{lv})^2}\frac{\partial^2 \bar{v}}{\partial \bar{x}^2} + \frac{\nu}{\delta v^o_{lv}}\frac{\partial^2 \bar{v}}{\partial \bar{y}^2}. \tag{4.15}$$

When the terms in Equations 4.14 and 4.15 are compared one by one from left to right, the orders of the each corresponding terms are same except the orders of pressure gradient terms. In a heat pipe or in an extending meniscus of an heat pipe inertial terms are small due to creeping flow. Therefore, the balance is between the pressure gradient that causes the flow and shear at the wall which balances it. Following this fact, the order of the viscous terms and pressure gradient term of Equation 4.14 can be assumed same or at least comparable. The order of viscous terms in Equation 4.15 are same with the ones in Equation 4.14 as mentioned previously. However, the order of the pressure gradient term of the y momentum equation, Equation 4.15, is $(u^o_{lv}/v^o_{lv})^2$ times higher than the order of viscous terms. In the y momentum equation, there exists no term which can balance the pressure gradient which makes the presence of the pressure gradient non-physical. Then, the pressure gradient in the y direction is dropped from the governing equations:

$$\frac{\partial u}{\partial x} + \frac{\partial v}{\partial y} = 0, \tag{4.16}$$

$$u\frac{\partial u}{\partial x} + v\frac{\partial u}{\partial y} = -\frac{1}{\rho}\frac{dP}{dx} + \nu\Big(\frac{\partial^2 u}{\partial x^2} + \frac{\partial^2 u}{\partial y^2}\Big), \tag{4.17}$$

$$u\frac{\partial v}{\partial x} + v\frac{\partial v}{\partial y} = \nu\Big(\frac{\partial^2 v}{\partial x^2} + \frac{\partial^2 v}{\partial y^2}\Big). \tag{4.18}$$

4.2 Solution Procedure

Equations which govern the fluid flow within the solution domain, contain three unknowns which are u velocity, v velocity and the liquid pressure. Three equations with three unknowns, can be mathematically solved. However, the boundaries of the solution domain are not known *a priori* because the film thickness variation is actually the result of the defined problem. So, an initial estimate for the film thickness distribution is required to begin the solution of bi-directional fluid flow. The film thickness distribution result of the unidirectional analysis can be used as an first estimate. Furthermore, film thickness distribution is directly linked to the pressure gradient in the x direction as suggested by Equation 3.34 and to evaporative mass flux as suggested by Equation 3.31. Thus, liquid pressure is not an unknown if film thickness variation is known. The remaining two unknowns, u and v, can be calculated by solving only two equations and these equations should be momentum equations because continuity equation drops due to the direct application of evaporative mass flux as an initial estimate.

The conservation of mass within the solution domain is going to be satisfied in an iterative process depending on the updates of the film thickness distribution which are achieved by the simultaneous solution of x and y momentum equations. Details about the conservation of mass will be explained in Section 4.2.2.

4.2.1 Solution of Momentum Equations by Spectral Element Method

Spectral element method, which is an hp formulation of the finite element method, is used in the solution of momentum equations. Spectral element method uses high degree piecewise polynomials (p), thus a fast convergence to the exact solution is realized with fewer number of elements (h). With the application of the spectral element method, higher order, accurate and continuous velocity distribution is aimed to achieve. Furthermore, the short range in which evaporative heat flux reaches its highest point and suddenly drops to zero, can be easily solved with adeqate resolution by the help of non-uniformly spaced Gauss-Lobatto-Legendre (GLL) nodes which enable high resolution near boundaries. Figure 4.1 shows a distribution of 10×10 Gauss-Lobatto-Legendre nodes in a square.

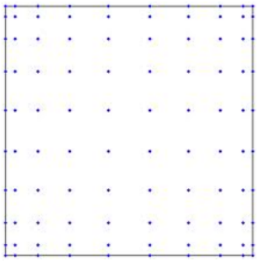

Figure 4.1: Distribution of 10×10 Gauss-Lobatto-Legendre nodes in a square

The spectral element method is capable of modelling complex and irregular geometries. In the current study, one quadrilateral element is used and it requires four vertex and four mathematically expressible edges to perform mapping between the irregular physical domain, Ω, and standard quadrilateral domain, Ω_{st}. The irregular physical domain on which spectral element method is applied, is seen in Figure 4.2

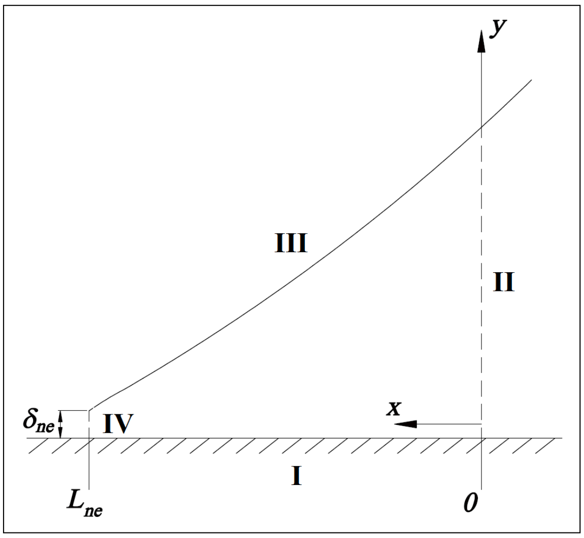

Figure 4.2: Physical domain

The set of two-dimensional momentum equations which are going to be solved by spectral element method is shown in Equations 4.19a-b:

$$u\frac{\partial u}{\partial x} + v\frac{\partial u}{\partial y} = \nu\Big(\frac{\partial^2 u}{\partial x^2} + \frac{\partial^2 u}{\partial y^2}\Big) + f(\delta), \tag{4.19a}$$

$$u\frac{\partial v}{\partial x} + v\frac{\partial v}{\partial y} = \nu\Big(\frac{\partial^2 v}{\partial x^2} + \frac{\partial^2 v}{\partial y^2}\Big). \tag{4.19b}$$

where $f(\delta)$ represents the liquid pressure gradient in the x direction and it is a known function of the film thickness. The boundary conditions of the momentum equations are established in Equations 4.20a-d:

$$I: \quad u = v = 0 \quad \text{at} \quad y = 0, \tag{4.20a}$$

$$II: \quad u = u_0(y) \quad v = v_0(y) \quad \text{at} \quad x = 0, \tag{4.20b}$$

$$III: \quad \mathbf{u} \cdot \mathbf{n} = m''_{evap}(\delta)/\rho \quad \text{at} \quad \text{the free surface}, \tag{4.20c}$$

$$IV: \quad u = v = 0 \quad \text{at} \quad x = L_{ne}. \tag{4.20d}$$

where $\mathbf{u} = [u, v]^T$.

4.2.1.1 Weak Formulation

The weak formulation of the equations is a variational statement of the problem. To achieve a weak form of a differential equation, equation is multiplied by a test function and integrated over the domain. The selection of the test functions can change according to the method preferred. When the dependent variable of the differential equation is approximated by trial functions, the result of integration is not exactly zero but equals to a residual. Then, the aim is to minimize the error between actual and approximate solutions.

Two-dimensional momentum equations, Equations 4.19a and 4.19b, are written in the vectorial form for the convenience, in the rest of the weak formulation,

$$\mathbf{u} \cdot \nabla \mathbf{u} = \nabla \cdot \bar{\bar{\sigma}} + \mathbf{F}, \tag{4.21}$$

where the vector, $\mathbf{F}$, which represents the body forces in Equation 4.21 should have the following form,

$$\mathbf{F} = [f(\delta), 0]^T. \tag{4.22}$$

The space of test functions,V, is defined on the boundaries as follows,

$$V = \{\mathbf{v} \in E(\Omega) \mid \quad \mathbf{v}|_I = \mathbf{v}|_{II} = \mathbf{v}|_{IV} = 0 \ ; \ \mathbf{v} \cdot \mathbf{n}|_{III} = 0\}, \tag{4.23}$$

where $\mathbf{v}$ is test function and $E(\Omega)$ is energy space.

Equation 4.21 is projected onto the space of test functions. The result of the integration can be seen below, in index notation:

$$\iint\limits_{\Omega} v_j u_i \frac{\partial u_j}{\partial x_i}\, d\Omega = \iint\limits_{\Omega} v_j \frac{\partial \sigma_{ij}}{\partial x_i}\, d\Omega \; + \; \iint\limits_{\Omega} v_j F_j\, d\Omega. \tag{4.24}$$

The first term at the right hand side of Equation 4.24 can be rewritten applying the chain rule,

$$\iint\limits_{\Omega} v_j u_i \frac{\partial u_j}{\partial x_i}\, d\Omega = \iint\limits_{\Omega} \left[\frac{\partial (v_j \sigma_{ij})}{\partial x_i} \; - \; \sigma_{ij}\frac{\partial v_j}{\partial x_i}\right] d\Omega \; + \; \iint\limits_{\Omega} v_j F_j\, d\Omega. \tag{4.25}$$

Considering only two-dimensional vector fields, divergence theorem is applied to the leading term of the first term at the right hand side of Equation 4.25:

$$\iint\limits_{\Omega} v_j u_i \frac{\partial u_j}{\partial x_i}\, d\Omega = \int\limits_{\partial\Omega} n_i \cdot (v_j \sigma_{ij})\, ds \; - \iint\limits_{\Omega} \sigma_{ij}\frac{\partial v_j}{\partial x_i}\, d\Omega \; + \; \iint\limits_{\Omega} v_j F_j\, d\Omega. \tag{4.26}$$

The first term at the right hand side of Equation 4.26 is equal to zero due to the definition of test function on the boundaries. Then, the weak formulation of the problem yields Equation 4.27 which is going to solve using trial functions for approximation,

$$\iint\limits_{\Omega} v_j u_i \frac{\partial u_j}{\partial x_i}\, d\Omega = - \iint\limits_{\Omega} \sigma_{ij}\frac{\partial v_j}{\partial x_i}\, d\Omega \; + \; \iint\limits_{\Omega} v_j F_j\, d\Omega. \tag{4.27}$$

Equation 4.27 can also be expressed in vector-operator notation:

$$\iint\limits_{\Omega} (\mathbf{v} \otimes \mathbf{u}) : \nabla \mathbf{u}\, d\Omega = - \iint\limits_{\Omega} \bar{\bar{\sigma}} : \nabla \mathbf{v}\, d\Omega \; + \; \iint\limits_{\Omega} \mathbf{v} \cdot \mathbf{F}\, d\Omega. \tag{4.28}$$

4.2.1.2 Mapping

In order to perform the numerical differentiations and integrations within the domain using of the Gauss-Lobatto-Legendre (GLL) nodes, the problem should be transformed to a standard domain which is a unit square.

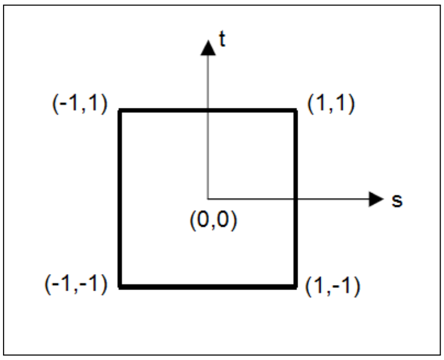

Figure 4.3: Standard domain

Actual irregular physical domain, Ω, then, should be mapped to the standard domain, Ω_{st}.

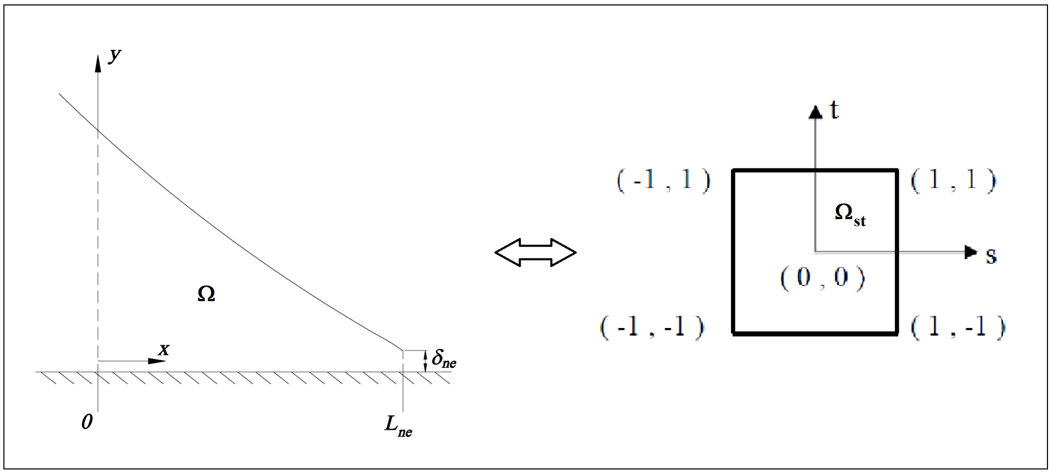

Figure 4.4: Mapping of physical domain to standard domain

The relation between actual and standard coordinates is constructed by using the mapping functions, X_1 and X_2:

$$x = X_1(s,t), \tag{4.29a}$$

$$y = X_2(s,t). \tag{4.29b}$$

Mapping functions, on the other hand, are constructed using the linear blending [56]. In this problem, mapping functions for the longitudinal and vertical coordinates are found as follows,

$$X_1(s,t) = \frac{1+s}{2} L_0\,, \tag{4.30a}$$

$$X_2(s,t) = \delta\left(\frac{1+s}{2} L_0\right) \frac{1+t}{2}\,, \tag{4.30b}$$

where $-1 \leq s,t \leq 1$ and δ is function of s as it is indicated. In the rest of the derivations, δ is going to be used without its argument for clarity.

The Jacobian of transformation is determined in Equation 4.31:

$$|J| = \left|\frac{\partial(s,t)}{\partial(x,y)}\right| = \left|\begin{pmatrix} \frac{L_0}{2} & 0 \\ \delta' \frac{L_0}{2}\frac{1+t}{2} & \frac{\delta}{2} \end{pmatrix}\right| = \frac{L_0}{4}\delta. \tag{4.31}$$

The calculation of mixed derivatives is necessary to evaluate the numerical differentiation operations in Equation 4.28. Mixed derivatives of transformation appears as in the form of Equations 4.32a-d:

$$\frac{\partial s}{\partial x} = \frac{2}{L_0}\,, \tag{4.32a}$$
$$\frac{\partial s}{\partial y} = 0\,, \tag{4.32b}$$
$$\frac{\partial t}{\partial x} = -2\frac{1+t}{L_0}\frac{\delta'}{\delta}\,, \tag{4.32c}$$
$$\frac{\partial t}{\partial y} = \frac{2}{\delta}\,. \tag{4.32d}$$

The gradient operator, then, becomes,

$$\nabla = \begin{bmatrix} \frac{\partial}{\partial x} \\ \frac{\partial}{\partial y} \end{bmatrix} = \begin{bmatrix} \frac{2}{L_0}\frac{\partial}{\partial s} - \frac{2(1+t)}{L_0}\frac{\delta'}{\delta}\frac{\partial}{\partial t} \\ \frac{2}{\delta}\frac{\partial}{\partial t} \end{bmatrix}. \tag{4.33}$$

4.2.1.3 Discretization

Dependent variable of the problem, which is the velocity, $\mathbf{u}$, in Equations 4.27 or 4.28 of the current study, is discretized by using polynomials next. In Galerkin approach, polynomial expansion is used for both trial space, U, and test space, V. Polynomial approximation of the dependent variable is shown in Equation 4.34:

$$\begin{bmatrix} u \\ v \end{bmatrix}(x,y) \cong \sum_{p=0}^{M}\sum_{q=0}^{N} \begin{bmatrix} u_{pq} \\ v_{pq} \end{bmatrix} L_p(s)L_q(t), \tag{4.34}$$

where L denotes Lagrange polynomial interpolant through Gauss-Lobatto-Legendre (GLL) points, $\{s_p, t_q\}$, typically,

$$L_p(s) = \prod_{m=0,m\neq p}^{M} \frac{s-s_m}{s_p-s_m} \quad \text{and} \quad \mathrm{L_q(t)} = \prod_{\mathrm{n=0,n\neq q}}^{\mathrm{N}} \frac{\mathrm{t-t_n}}{\mathrm{t_q-t_n}}, \tag{4.35}$$

where $\begin{bmatrix} u_{pq} \\ v_{pq} \end{bmatrix} = \begin{bmatrix} u \\ v \end{bmatrix}(X_1(s_p,t_q), X_2(s_p,t_q))$.

At the GLL nodes, Lagrange interpolants, Equation 4.35, exhibit Kronecker-Delta property,

$$L_p(s_m) = \delta_{pm}\,, \tag{4.36a}$$

$$L_q(t_n) = \delta_{qn}\,, \tag{4.36b}$$

with ‘$-1 = s_0 < ... < s_M = 1$ and $-1 = t_0 < ... < t_N = 1$.

GLL nodes together with the associated weights $\{w_m, w_n\}$ provide high accuracy quadrature approximation for integrals. A representative integration for the longitudinal velocity on the physical domain is performed in the following equations.

First, actual physical domain is transformed to the standard domain:

$$\iint\limits_{\Omega} u(x,y)\, d\Omega = \iint\limits_{\Omega_{st}} u\left(x(s,t), y(s,t)\right) J\, dsdt\,. \tag{4.37}$$

Secondly, discretization of the dependent variable is performed:

$$\iint\limits_{\Omega} u(x,y)\, d\Omega \cong \sum_{p=0}^{M}\sum_{q=0}^{N} u_{pq} \iint\limits_{\Omega_{st}} J L_p(s) L_q(t)\, dsdt\,. \tag{4.38}$$

Next, numerical integration is applied with the associated weights $\{w_k, w_l\}$:

$$\iint\limits_{\Omega} u(x,y)\, d\Omega \cong \sum_{p=0}^{M}\sum_{q=0}^{N} u_{pq} \left(\sum_{k=0}^{M}\sum_{l=0}^{N} J(s_k,t_l) L_p(s_k) L_q(t_l) w_k w_l \right)\,. \tag{4.39}$$

Then, Kronecker-Delta property of the Lagrange interpolants is used:

$$\iint\limits_{\Omega} u(x,y)\, d\Omega \cong \sum_{p=0}^{M}\sum_{q=0}^{N} u_{pq} \left(\sum_{k=0}^{M}\sum_{l=0}^{N} J(s_k,t_l) \delta_{pk} \delta_{ql} w_k w_l \right)\,. \tag{4.40}$$

The final, transformed and integrated form of the term can be seen in Equation 4.41:

$$\iint\limits_{\Omega} u(x,y)\, d\Omega \cong \sum_{k=0}^{M}\sum_{l=0}^{N} u_{kl} J_{kl} w_k w_l, \tag{4.41}$$

where $J_{kl} = J\left(X_1(s_k,t_l), X_2(s_k,t_l)\right)$.

To sum up, the weak form of momentum equations, Equation 4.28 or 4.29, has formed. Then, mapping of physical domain to standard domain has explained. After that, discretization procedure of trial and test spaces has shown.

Discretized formulation yields a definite set of equations. The number of equations is equal to the number of GLL nodes used in the domain. In this problem, 61×61 nodes are used to discretize the domain and one single element is used to represent the domain. Thus, the polynomials which approximate the trial and test space, are of 60^{th} degree.

4.2.1.4 Boundary Conditions

Boundary conditions were given in Equations 4.20a-d for the actual physical domain. These boundary conditions should also be transformed and discretized for the standard domain on which numerical calculation is performed.

Equation 4.20a, which states zero velocities at the wall, is result of the no-slip condition assumption of fluid particles at the solid contact. Due to this condition, velocities defined at the nodes of the boundary I is zero:

$$u_{p0} = v_{p0} = 0 \qquad \text{for} \qquad p = 0, 1, ..., M. \tag{4.42}$$

Equation 4.20b shows the initial velocity distributions, $u_0(y)$ and $v_0(y)$. They are assumed to have parabolic velocity profiles. Their magnitudes, on the other hand, are specified to satisfy the amount of inlet mass flow. The amount of inlet mass flow, on the other hand, cannot be known *a priori* because it must be equal to the total evaporated fluid amount which is one of the result of the complete analysis. Thus, the inlet mass flow, so as the initial velocity distributions are subjected to changes which are performed in an iterative manner and procedure is going to be explained in the Section 4.2.2. Discretization of the initial velocities at II can be seen in Equation 4.43:

$$u_{0q} = u_0\left(X_2(s_0, t_q)\right) \quad \text{and} \quad v_{0q} = v_0\left(X_2(s_0, t_q)\right) \qquad \text{for} \qquad q = 0, 1, ..., N. \tag{4.43}$$

Equation 4.20c states the relation between evaporative mass flux from the liquid-vapor interface and fluid velocities at the interface. As in the case of initial velocities, evaporative mass flux is also subjected to changes because the distribution of evaporative mass flux is a result of complete analysis and cannot known *a priori*. Before giving the discretization of the boundary condition at interface, unit normal vector to the surface must be defined:

$$\mathbf{n} = \frac{-\delta'}{\sqrt{1+(\delta')^2}}\,\mathbf{i} + \frac{1}{\sqrt{1+(\delta')^2}}\,\mathbf{j}\,. \tag{4.44}$$

After the multiplication of unit normal vector with velocity vector, Equation 4.20c can be rewritten as shown by Equation 4.45:

$$-\delta' u + v = \frac{\sqrt{1+(\delta')^2}}{\rho} m''_{evap}\,. \tag{4.45}$$

The boundary condition of surface velocities at III can also be expressed as in the form of Equation 4.46:

$$-u_{pN}\delta'(s_p) + v_{pN} = \frac{\sqrt{1+(\delta'(s_p))^2}}{\rho} m''_{evap}(s_p) \qquad \text{for} \qquad p = 0, 1, ..., M. \tag{4.46}$$

Equation 4.20d is the boundary condition at the end of the evaporating thin film region or at the starting point of non-evaporating region which is completely a stationary zone behaving like a solid body. Therefore, the velocities at the nodes of the boundary IV are zero,

$$u_{Mq} = v_{Mq} = 0 \qquad \text{for} \qquad q = 0, 1, ..., N. \quad (4.47)$$

For the homogeneous boundary conditions, test functions, v, are discretized in the same way and after implementing boundary conditions, the resultant set of equations is solved using the MATLAB software. In the numerical solution procedure, Picard iteration is used to handle the non-linear terms of the Navier-Stokes equation.

4.2.2 Application of Conservation of Mass

By solving the linear momentum equations, distributions of u and v velocity in the micro region have been determined without considering the conservation of mass in the spectral formulation. However, the film thickness distribution which is used as a constant boundary for the solution domain of spectral element method, has to be updated such that conservation of mass must hold even in the presence of transverse velocity, v. To update the film thickness distribution, spectral element method cannot be applied due to the fact that it requires non-changing boundaries to discretize the domain by nodes. Then, mass conservation is obtained by using the evaporation model based unidirectional flow.

In the solution of the unidirectional flow, only x momentum equation was considered. Furthermore, inertial terms and second derivative of the u velocity with respect to x direction were neglected due to boundary layer assumptions. The evaporation model based on the bi-directional flow, on the other hand, includes these neglected terms in the x momentum equation which is Equation 4.17 and rewritten below,

$$u\frac{\partial u}{\partial x} + v\frac{\partial u}{\partial y} = -\frac{1}{\rho}\frac{dP}{dx} + \nu\Big(\frac{\partial^2 u}{\partial x^2} + \frac{\partial^2 u}{\partial y^2}\Big). \tag{4.17}$$

Equation 4.17, can be written as follows,

$$\frac{\partial^2 u}{\partial y^2} = \frac{1}{\mu}\frac{dP}{dx} + \frac{1}{\nu}\Big(u\frac{\partial u}{\partial x} + v\frac{\partial u}{\partial y}\Big) - \frac{\partial^2 u}{\partial x^2}. \tag{4.48}$$

Furthermore, the neglected terms in the unidirectional flow model are grouped and named as ϕ,

$$\phi(x,y) = \frac{1}{\nu}\Big(u\frac{\partial u}{\partial x} + v\frac{\partial u}{\partial y}\Big) - \frac{\partial^2 u}{\partial x^2}\,. \tag{4.49}$$

Then, Equation 4.48 can be written in term of ϕ:

$$\frac{\partial^2 u}{\partial y^2} = \frac{1}{\mu}\frac{dP}{dx} + \phi(x,y). \tag{4.50}$$

The term on the left side and the first term at the right hand side of Equation 4.50 are the terms existing in the derivation of the evaporation model based on both unidirectional and bi-directional flow. The term $\phi(x,y)$, on the other hand, exists only on the formulation of evaporation model based on bi-directional flow.

Although the spectral element formulation of the bi-directional flow considers only the conservation of linear momentum, unidirectional flow based solution takes both mass and momentum conservation into consideration. Then, in order to satisfy conservation of mass, unidirectional flow model can be used. The term ϕ contains the effect of bi-directional solution. If the unidirectional model is applied by adding the values of the term ϕ into the formulation, in other words, if Equation 4.50 is used in formulation of unidirectional flow, a new film thickness distribution including the effect of bi-directional solution, can be achieved and conservation of mass is satisfied. However, the values of the term $\phi(x,y)$ within the domain have a two-dimensional distribution as a natural consequence of the spectral element solution. In order to use the unidirectional flow model, Equation 4.50 should be integrated twice in y direction. With the presence of two-dimensional $\phi(x,y)$ term, Equation 4.52 cannot be analytically integrated. To overcome this difficulty, the average values of the term at the x-coordinates, $\bar{\phi}(x)$, are calculated. Then, the right hand side of Equation 4.52 becomes only function of x as shown in Equation 4.51:

$$\frac{\partial^2 u}{\partial y^2} = \frac{1}{\mu}\frac{dP}{dx} + \bar{\phi}(x). \tag{4.51}$$

With the no slip boundary condition at the wall surface and no shear assumption at the liquid-vapor interface, two times integration of Equation 4.53 yields the u velocity distribution of unidirectional flow:

$$u = \Big(\frac{1}{\mu}\frac{dP}{dx} + \bar{\phi}(x)\Big)\Big(\frac{y^2}{2} - \delta y\Big). \tag{4.52}$$

Using this velocity distribution and the solution methodology explained in Section 3.2, a new film thickness having the effect of v velocity from the spectral element solution *via* the term $\bar{\phi}(x)$, is achieved. However, this process is not enough to conform the conservation of mass and momentum at the same time. The new film thickness distribution and the new evaporative heat flux distribution as a function of film thickness, are not used as boundary or boundary condition to the bi-directional flow domain. Then, using the new film thickness distribution and evaporative heat flux distribution, solution of the bi-directional model should be repeated. After that, unidirectional flow model should be applied again to add the effect of new values of $\bar{\phi}(x)$ to the conservation of mass. This iterative procedure must be repeated until convergence. The detailed solution process which includes the application of conservation of mass for bi-directional flow based evaporation model, is summarized on a flow chart in Appendix A.

4.3 Results

After making three cycles of iterations between the solutions of spectral element method and unidirectional flow model, the change in the film thickness variation becomes negligible. Then, the results at the end of three iterations can be taken as final results which satisfy the conservation of mass and x and y linear momentum equations for the bi-directional liquid flow. Thus, the evaporation model which includes both the effect of planar velocities u and v, is completed and results can be examined. The distributions of u and v velocities with the distribution of heat flux in the micro region and in the close proximity of contact line are shown in Figures 4.5 and 4.6, respectively.

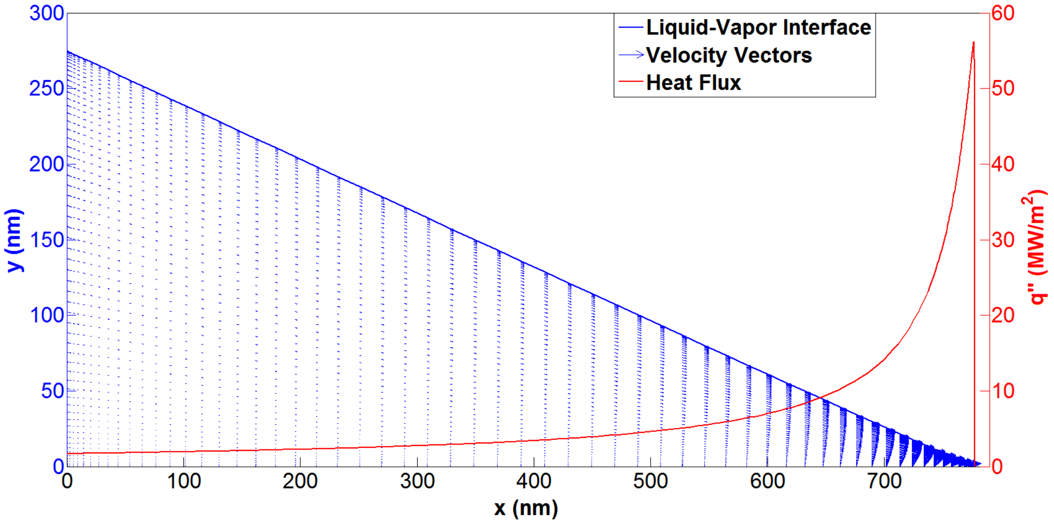

Figure 4.5: Bi-directional velocity vectors in the micro region

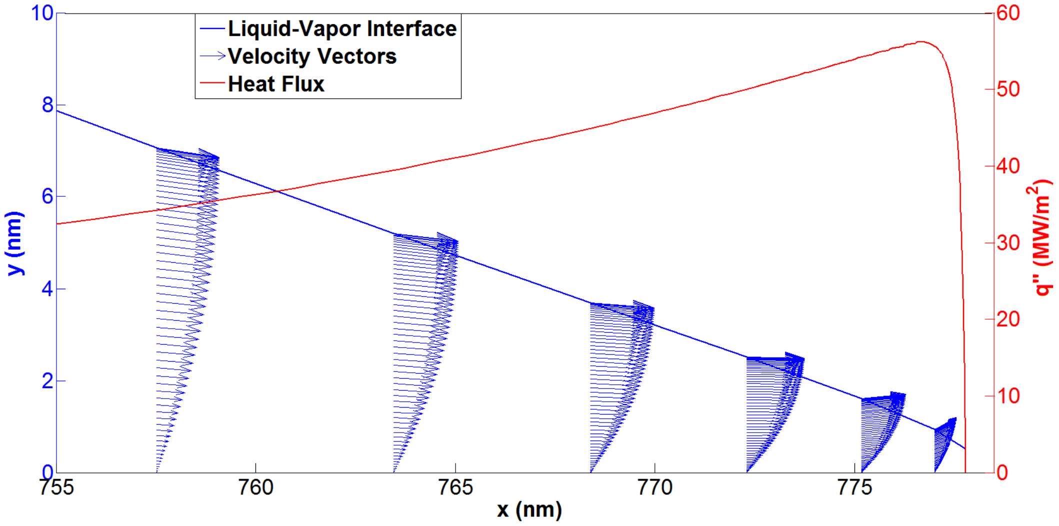

Figure 4.6: Bi-directional velocity vectors near contact line

The magnitudes of the velocity vectors show increasing trend with decreasing film thickness at first glance in Figure 4.5. This trend is a result of decreasing flow area and increasing evaporation rate. When Figure 4.6 is examined, fluid continues to accelerate in the horizontal direction until peak evaporation flux is reached. To understand the detailed behaviour of the horizontal velocity, a contour plot of it is given in Figure 4.7.

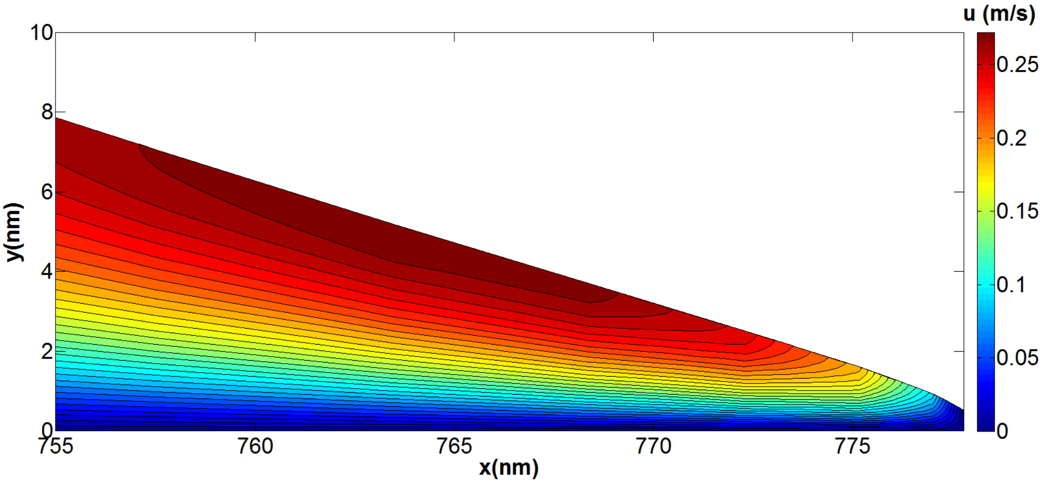

Figure 4.7: Distribution of u velocity near contact line

Due to the sharp increase of the disjoining pressure, evaporation is suppressed and fluid comes to rest at the point of zero evaporation which is the starting point of the non-evaporating region. As it can be seen from Figure 4.6, the distance between the maximum evaporation point and starting point of the non-evaporating region is very short. Therefore, flow starts to decelerate before the point of maximum evaporation and matches the “zero fluid velocity” condition at the contact line. As it can be seen from Figure 4.7, the maximum u velocity is reached approximately at a distance of 765 nm whereas the maximum evaporation occurs at a distance of 777 nm.

The distribution of the v velocity in the micro region is shown in Figure 4.8.

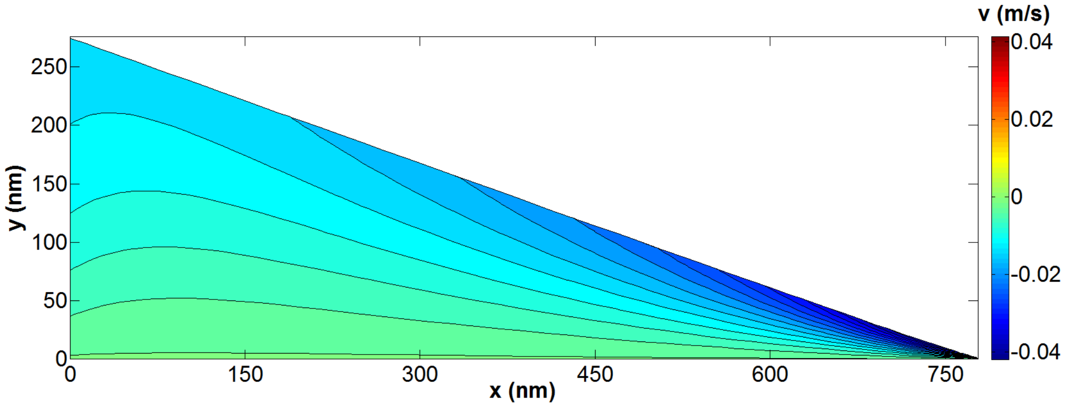

Figure 4.8: Distribution of v velocity in the micro region

Figure 4.8 shows that the magnitude of the v velocity increases with diminishing flow area, similar to u velocity. To see the distribution of v velocity near the contact line, a close up plot is given in Figure 4.9.

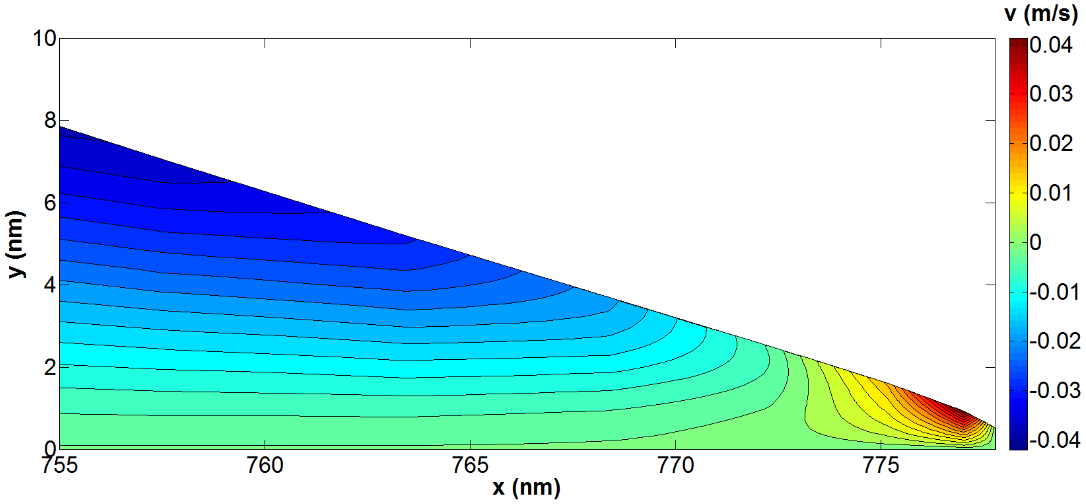

Figure 4.9: Distribution of v velocity near contact line

When Figure 4.9 is examined, the magnitude of the v velocity decelerates due to the effect of the stationary contact line except the sharp increase at the maximum evaporation point. The resolution of the contour plot is not sufficient to view the phenomena occurring at the close vicinity of the maximum evaporation point together with the rest of the micro region. Observing the values of the v velocity at the free surface may yield a better understanding of the change of v velocity within the micro region.

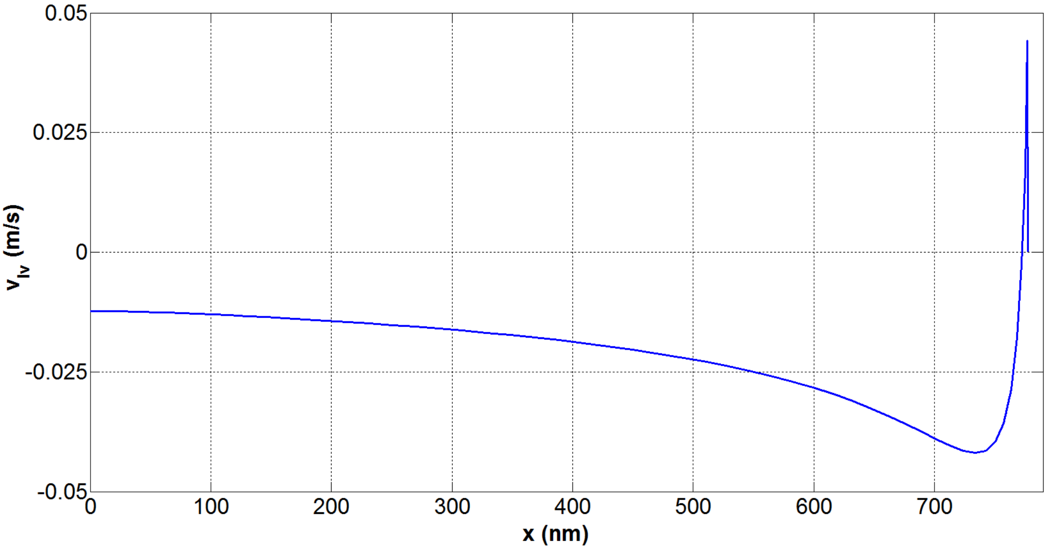

Figure 4.10: Distribution of v velocity at the free surface

The change of v velocity at the liquid-vapor interface is informative in representing the distribution trend of the v velocity throughout the problem domain. Initially, the magnitude of the v velocity decreases due to the contraction of the flow area and the sign of the v velocity is negative due to the slope of the free surface. Then, magnitude of the v velocity begins to drop at about a distance of 735 nm, because the flow decelerates due to the effect of the stationary fluid boundary condition at the contact line. On the other hand, the evaporation curve reaches its peak at a distance of 777 nm and fluid molecules escape from the liquid phase at higher rates when approaching this point. Thus, instead of coming to a rest, fluid molecules accelerate in the positive vertical direction and

v velocity reaches its maximum magnitude with the positive sign at the point of maximum evaporation. After this peak, due to the sudden drop in evaporation, v velocity drops sharply and becomes zero at the contact line.

Finally, it should be noted that the effect of the bi-directional flow based evaporation model to the total evaporated mass is found to be negligible because the total evaporated mass decreases only 0.04% from the mass found by uni-directional flow based evaporation model. However, the presentation of the distribution of vertical velocity in the micro region enables to understand the underlying physical phenomena.

CHAPTER 5

CONTRIBUTION OF AXIAL FLOW TO EVAPORATION

A considerable amount of the evaporation originates from the micro region or specifically from the evaporating thin film region part of the micro region. Previous chapters have been devoted to modelling the evaporation occurring in the thin film region of an arbitrary cross-section of grooved heat pipe. Firstly, a uni-directional flow model is developed without considering the vertical component of the fluid velocity. Secondly, a bi-directional model is suggested by including the vertical component of the velocity by solving the two-dimensional momentum equations in two directions by using a one element spectral method. The undisturbed meniscus region of the bulk fluid is taken as the fluid supply to the evaporating thin film region in the one and two dimensional analyses. However, in order to suggest a complete model, the mass supply contribution of the fluid flow in the axial direction of the heat pipe, to the micro region must be added. The fluid flow which is parallel to the groove axis (heat pipe axis), must be modelled to asses the amount of mass entering the micro region.

5.1 Formulation

The complete formulation of the fluid flow in the z direction (*i.e.* parallel to groove axis) of heat pipe requires the solution of conservation of mass and linear momentum equations. Conservation of mass including the effect of flow in the z direction can only be modelled including the evaporation and condensation process as whole. However, this study only aims to create a three-dimensional evaporation model of the micro region and condensation phenomena is not covered in this thesis. Thus, a comprehensive model of fluid flow in the z direction cannot be covered. At this point, it is decided that only conservation of linear momentum equations are taken into account to get the w velocity distribution on a cross-section of the groove. Moreover, the required mass conservation information is going to be taken from the study of Odabaşı [43] which covers the axial fluid flow as an whole, in a similar geometry. Conservation of linear momentum requires the solution of the following three components of the Navier-Stokes equation:

$$u\frac{\partial u}{\partial x}+v\frac{\partial u}{\partial y}+w\frac{\partial u}{\partial z}=-\frac{1}{\rho}\frac{\partial P}{\partial x}+\nu\Big(\frac{\partial^2 u}{\partial x^2}+\frac{\partial^2 u}{\partial y^2}+\frac{\partial^2 u}{\partial z^2}\Big), \tag{5.1}$$

$$u\frac{\partial v}{\partial x}+v\frac{\partial v}{\partial y}+w\frac{\partial v}{\partial z}=-\frac{1}{\rho}\frac{\partial P}{\partial y}+\nu\Big(\frac{\partial^2 v}{\partial x^2}+\frac{\partial^2 v}{\partial y^2}+\frac{\partial^2 v}{\partial z^2}\Big), \tag{5.2}$$

$$u\frac{\partial w}{\partial x}+v\frac{\partial w}{\partial y}+w\frac{\partial w}{\partial z}=-\frac{1}{\rho}\frac{\partial P}{\partial z}+\nu\Big(\frac{\partial^2 w}{\partial x^2}+\frac{\partial^2 w}{\partial y^2}+\frac{\partial^2 w}{\partial z^2}\Big). \tag{5.3}$$

However, before starting solving them, an order of magnitude analysis should be applied. The ratio of the groove depth, d, or groove thickness, h, to the groove length, L can be chosen as the scaling parameter which is much smaller than one,

$$\epsilon=\frac{d}{L}. \tag{5.4}$$

As another scaling parameter, capillary number can be used whose definition is the ratio of the viscous forces to capillary forces,

$$C=\frac{\mu U}{\sigma}. \tag{5.5}$$

where U is the velocity scale in the axial direction. Capillary number is usually large for high-speed flows and low for low-speed flows. In the case of a heat pipe, low-speed flows are experienced. Then, following the study of Markos-Gebresilassie [57], these scaling parameters are taken equal for creeping flow assumption,

$$\epsilon = C. \tag{5.6}$$

Non-dimensionalization of the coordinates can be seen below,

$$\bar{x} = \frac{x}{d}, \tag{5.7}$$

$$\bar{y} = \frac{y}{d}, \tag{5.8}$$

$$\bar{z} = \frac{z}{L} = \epsilon \frac{z}{d}. \tag{5.9}$$

Considering the continuity, velocities can be non-dimensionalized as follows,

$$\bar{u} = \frac{u}{\epsilon U}, \tag{5.10}$$

$$\bar{v} = \frac{v}{\epsilon U}, \tag{5.11}$$

$$\bar{w} = \frac{w}{U}. \tag{5.12}$$

The main driving force for the flow is associated with the deformation of the curvature of the free surface in a heat pipe. Then, the absolute pressure can be scaled by the capillary pressure,

$$\bar{P} = \frac{P}{\sigma / d}. \tag{5.13}$$

Then, Equations 5.1 to 5.3 are non-dimensionalized by inserting non-dimensional forms of the variables,

$$\frac{\epsilon^2 U^2}{d}\left(\bar{u}\frac{\partial \bar{u}}{\partial \bar{x}} + \bar{v}\frac{\partial \bar{u}}{\partial \bar{y}} + \bar{w}\frac{\partial \bar{u}}{\partial \bar{z}}\right) = -\frac{\sigma}{d^2\rho}\frac{\partial \bar{P}}{\partial \bar{x}} + \frac{\epsilon U\nu}{d^2}\left(\frac{\partial^2 \bar{u}}{\partial \bar{x}^2} + \frac{\partial^2 \bar{u}}{\partial \bar{y}^2} + \frac{\partial^2 \bar{u}}{\partial \bar{z}^2}\right), \tag{5.14}$$

$$\frac{\epsilon^2 U^2}{d}\left(\bar{u}\frac{\partial \bar{v}}{\partial \bar{x}} + \bar{v}\frac{\partial \bar{v}}{\partial \bar{y}} + \bar{w}\frac{\partial \bar{v}}{\partial \bar{z}}\right) = -\frac{\sigma}{d^2\rho}\frac{\partial \bar{P}}{\partial \bar{y}} + \frac{\epsilon U\nu}{d^2}\left(\frac{\partial^2 \bar{v}}{\partial \bar{x}^2} + \frac{\partial^2 \bar{v}}{\partial \bar{y}^2} + \frac{\partial^2 \bar{v}}{\partial \bar{z}^2}\right), \tag{5.15}$$

$$\frac{\epsilon U^2}{d}\left(\bar{u}\frac{\partial \bar{w}}{\partial \bar{x}} + \bar{v}\frac{\partial \bar{w}}{\partial \bar{y}} + \bar{w}\frac{\partial \bar{w}}{\partial \bar{z}}\right) = -\frac{\epsilon\sigma}{d^2\rho}\frac{\partial \bar{P}}{\partial \bar{z}} + \frac{U\nu}{d^2}\left(\frac{\partial^2 \bar{w}}{\partial \bar{x}^2} + \frac{\partial^2 \bar{w}}{\partial \bar{y}^2} + \frac{\partial^2 \bar{w}}{\partial \bar{z}^2}\right). \tag{5.16}$$

Using the equality defined in Equation 5.6, surface tension is written in terms of absolute viscosity, μ, velocity scale, U, and small scaling parameter, ϵ:

$$\sigma = \frac{\mu U}{\epsilon}. \tag{5.17}$$

Equation 5.17 can be used to eliminate the term surface tension appearing in Equations 5.14 to 5.16:

$$\frac{\epsilon^2 U^2}{d}\left(\bar{u}\frac{\partial \bar{u}}{\partial \bar{x}} + \bar{v}\frac{\partial \bar{u}}{\partial \bar{y}} + \bar{w}\frac{\partial \bar{u}}{\partial \bar{z}}\right) = -\frac{U\nu}{\epsilon d^2}\frac{\partial \bar{P}}{\partial \bar{x}} + \frac{\epsilon U\nu}{d^2}\left(\frac{\partial^2 \bar{u}}{\partial \bar{x}^2} + \frac{\partial^2 \bar{u}}{\partial \bar{y}^2} + \frac{\partial^2 \bar{u}}{\partial \bar{z}^2}\right), \tag{5.18}$$

$$\frac{\epsilon^2 U^2}{d}\left(\bar{u}\frac{\partial \bar{v}}{\partial \bar{x}} + \bar{v}\frac{\partial \bar{v}}{\partial \bar{y}} + \bar{w}\frac{\partial \bar{v}}{\partial \bar{z}}\right) = -\frac{U\nu}{\epsilon d^2}\frac{\partial \bar{P}}{\partial \bar{y}} + \frac{\epsilon U\nu}{d^2}\left(\frac{\partial^2 \bar{v}}{\partial \bar{x}^2} + \frac{\partial^2 \bar{v}}{\partial \bar{y}^2} + \frac{\partial^2 \bar{v}}{\partial \bar{z}^2}\right), \tag{5.19}$$

$$\frac{\epsilon U^2}{d}\left(\bar{u}\frac{\partial \bar{w}}{\partial \bar{x}} + \bar{v}\frac{\partial \bar{w}}{\partial \bar{y}} + \bar{w}\frac{\partial \bar{w}}{\partial \bar{z}}\right) = -\frac{U\nu}{d^2}\frac{\partial \bar{P}}{\partial \bar{z}} + \frac{U\nu}{d^2}\left(\frac{\partial^2 \bar{w}}{\partial \bar{x}^2} + \frac{\partial^2 \bar{w}}{\partial \bar{y}^2} + \frac{\partial^2 \bar{w}}{\partial \bar{z}^2}\right). \tag{5.20}$$

If Equations 5.18 and 5.19 are multiplied by the ϵ and Equations 5.18 to 5.20 are divided to $U\nu/d^2$, the resultant equations becomes as follows,

$$\frac{\epsilon^3 U}{\nu d^3}\left(\bar{u}\frac{\partial \bar{u}}{\partial \bar{x}}+\bar{v}\frac{\partial \bar{u}}{\partial \bar{y}}+\bar{w}\frac{\partial \bar{u}}{\partial \bar{z}}\right)=-\frac{\partial \bar{P}}{\partial \bar{x}}+\epsilon^2\left(\frac{\partial^2 \bar{u}}{\partial \bar{x}^2}+\frac{\partial^2 \bar{u}}{\partial \bar{y}^2}+\frac{\partial^2 \bar{u}}{\partial \bar{z}^2}\right), \tag{5.21}$$

$$\frac{\epsilon^3 U}{\nu d^3}\left(\bar{u}\frac{\partial \bar{v}}{\partial \bar{x}}+\bar{v}\frac{\partial \bar{v}}{\partial \bar{y}}+\bar{w}\frac{\partial \bar{v}}{\partial \bar{z}}\right)=-\frac{\partial \bar{P}}{\partial \bar{y}}+\epsilon^2\left(\frac{\partial^2 \bar{v}}{\partial \bar{x}^2}+\frac{\partial^2 \bar{v}}{\partial \bar{y}^2}+\frac{\partial^2 \bar{v}}{\partial \bar{z}^2}\right), \tag{5.22}$$

$$\frac{\epsilon U}{\nu d^3}\left(\bar{u}\frac{\partial \bar{w}}{\partial \bar{x}}+\bar{v}\frac{\partial \bar{w}}{\partial \bar{y}}+\bar{w}\frac{\partial \bar{w}}{\partial \bar{z}}\right)=-\frac{\partial \bar{P}}{\partial \bar{z}}+\left(\frac{\partial^2 \bar{w}}{\partial \bar{x}^2}+\frac{\partial^2 \bar{w}}{\partial \bar{y}^2}+\frac{\partial^2 \bar{w}}{\partial \bar{z}^2}\right). \tag{5.23}$$

Order one approximation of Equations 5.21 to 5.23 yields following equations,

$$\frac{\partial \bar{P}}{\partial \bar{x}}=\frac{\partial \bar{P}}{\partial \bar{y}}=0, \tag{5.24}$$

$$\frac{\partial \bar{P}}{\partial \bar{z}}=\frac{\partial^2 \bar{w}}{\partial \bar{x}^2}+\frac{\partial^2 \bar{w}}{\partial \bar{y}^2}. \tag{5.25}$$

Equation 5.24 implies that the change of absolute pressure is only a function of z-coordinate at the leading order. The change of pressure with the z-coordinate is formulated by Equation 5.25 which is the two-dimensional Poisson's Equation.

5.2 Solution Procedure

Equation 5.25 shows that to get the axial velocity, w, distribution in an arbitrary cross-section of the heat pipe groove, the value of the pressure gradient at that axial location must be known. In other words, to solve Equation 5.25 for the w, the left side of the equation has to be known. In her study, Odabaşı [43] used the same groove geometry to model the flow along the groove channel. The change of the radius of curvature of the liquid-vapor interface and the pressure gradient along the groove axis were calculated in the study of Odabaşı. Then, an approximate value of the pressure gradient corresponding to the axial location where the undisturbed main radius of the interface is close to the radius value used in the current study, can be taken from the study of Odabaşı [43]. In spite of the fact that current study and study of Odabaşı use different approaches in the solution of evaporation phenomena, the approximate value taken from the study of Odabaşı [43] is sufficient to estimate the contribution of axial flow as a source of fluid supply to the evaporation process. Therefore, the average liquid pressure gradient at the cross-section on which the problem is going to be solved, has a known value,

$$\left.\frac{\partial \bar{P}}{\partial \bar{z}}\right|_{z^*} = f(z^*), \tag{5.26}$$

where z^* is the z-coordinate corresponding to the location of the cross-section along the axial direction and $f(z^*)$ is the value of the average pressure gradient at that section.

Equation 5.25 is going to be solved using spectral element method because spectral element method can give adequate accuracy even in small regions like evaporating thin film region, the schematic of which given in Figure 5.1.

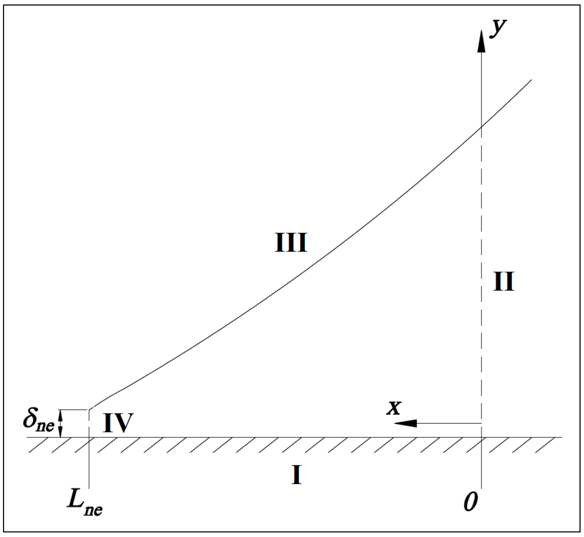

Figure 5.1: Evaporating thin film region

In order to solve Poisson's Equation in the evaporating thin film region, boundary conditions at the boundaries have to be defined. No slip boundary condition is assumed at the wall surface. At the end of the domain, zero velocity is considered due to stationary, non-evaporating fluid. No shear is assumed at the liquid-vapor interface. At the entrance of the domain, on the other hand, velocity distribution of the axial velocity is unknown and the problem cannot be solved without this information. To get an estimate for the distribution of the inlet velocity at the entrance of the micro region, the problem is solved on the half of the groove cross-section which includes micro region and has definite boundary conditions as well.

5.2.1 Solution of Poisson's Equation on the Groove Cross-Section

Quadrilateral element requires the use of 4 vertex points and 4 edges which should be suitable to define by definite functions. The selection of the half of the groove cross-section together with the micro region as problem domain creates 5 vertex points and 5 edges as it can be seen in Figure 5.2.

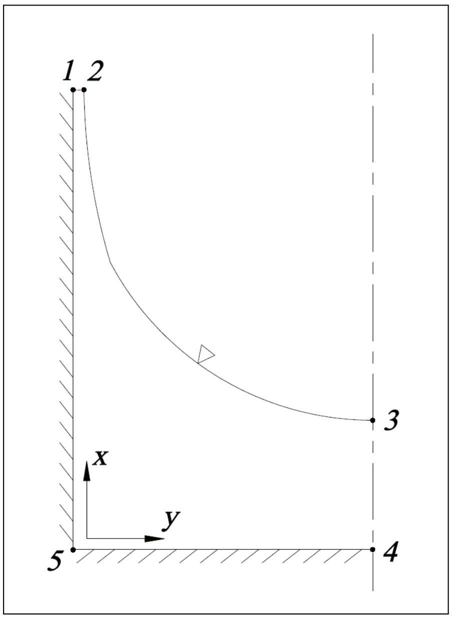

Figure 5.2: Half cross-section having 5 vertex points

The height of the non-evaporating region which is assumed as a horizontal line attached to the tip of the groove rather than representing a region, is lying between points 1 and 2 of Figure 5.2 and existence this boundary creates an extra vertex and edge. However, the length of this boundary is at the order of 1 nanometer. When compared with the dimensions of the groove, this boundary can be neglected. Figure 5.3 shows the simplified domain having 4 vertex points and edges.

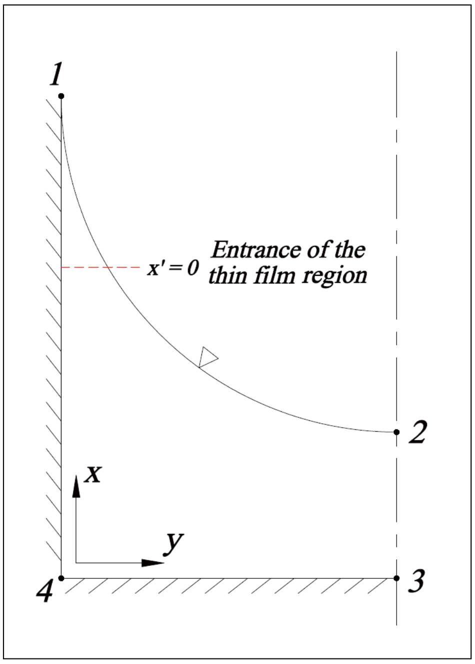

Figure 5.3: Half cross-section having 4 vertex points

Moreover, the approximate location of the entrance of thin film region is shown by a dashed line in Figure 5.3.

When the problem is solved on the domain indicated by Figure 5.3, the w velocity distribution is achieved throughout the domain. Applying a simple post process, the w velocity distribution at the entrance line of the thin film region can be extracted from the overall results. Then, solution of the Poisson's Equation on the groove cross-section is the initial task to reach the w velocity distribution at the micro region.

Before solving the Poisson's Equation, the boundary conditions have to be defined at the half groove geometry. Firstly, no slip condition is assumed at the groove walls. At the center line of the groove, symmetry condition is assumed. Lastly, negligible shear force between liquid and gas phases is assumed at the liquid-vapor interface. The non-dimensional Poisson's Equation with the boundary conditions can be seen below,

$$\frac{\partial^2 \bar{w}}{\partial \bar{x}^2} + \frac{\partial^2 \bar{w}}{\partial \bar{y}^2} = f(z^*), \tag{5.27}$$

$$\begin{aligned}
\bar{w} &= 0 \qquad \text{at} \quad \bar{x} = 0, && (5.28a)\\
\bar{w} &= 0 \qquad \text{at} \quad \bar{y} = 0, && (5.28b)\\
\mathbf{n} \cdot \bar{\bar{\sigma}} \cdot \mathbf{t} &= 0 \qquad \text{at} \quad \text{the free surface,} && (5.28c)\\
\frac{\partial \bar{w}}{\partial \bar{x}} &= 0 \qquad \text{at} \quad \bar{y} = b. && (5.28d)
\end{aligned}$$

The solution of the Poisson's Equation is performed by spectral element method which uses one element discretized by 77 × 77 GLL nodes. The details about the discretization of the formulation or mapping between physical and standard domain in the spectral element method were given in Chapter 4.2.1. So, spectral element method is not reviewed again in the current chapter.

The resultant distribution of the axial velocity, w, is seen in Figure 5.4.

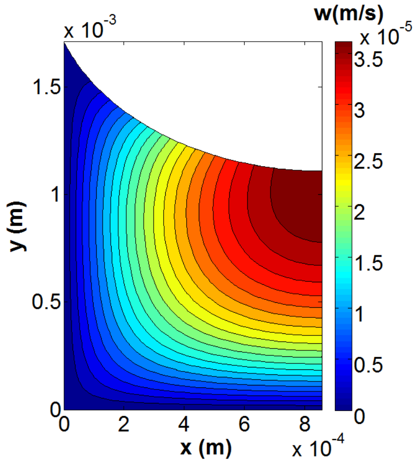

Figure 5.4: Axial velocity distribution in the groove

5.2.2 Solution of Poisson's Equation on the Micro Region

The dimensions and the location of the micro region on the groove cross-section were calculated in the previous chapters. From the velocity distribution shown in Figure 5.4, velocity of the fluid entering to the micro region (evaporating thin film region) can be extracted. The problem domain for the micro region is seen in Figure 5.5 where the coordinate x' is replaced by x for the simplicity.

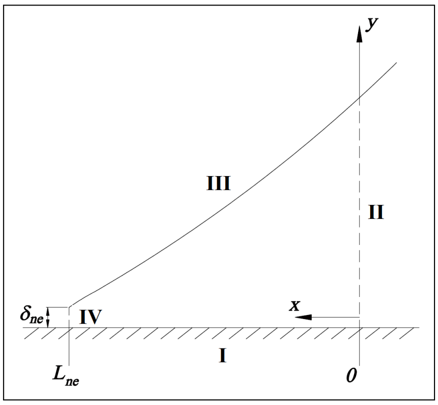

Figure 5.5: Evaporating thin film region

The governing equation with the corresponding boundary condition can be expressed as follows,

$$\frac{\partial^2 \bar{w}}{\partial \bar{x}^2} + \frac{\partial^2 \bar{w}}{\partial \bar{y}^2} = f(z^*), \tag{5.29}$$

$$\bar{w} = \bar{w}_0(\bar{y}), \quad \text{at} \quad \bar{x} = 0, \tag{5.30a}$$

$$\bar{w} = 0 \quad \text{at} \quad \bar{y} = 0, \tag{5.30b}$$

$$\mathbf{n} \cdot \bar{\bar{\sigma}} \cdot \mathbf{t} = 0 \quad \text{at} \quad \text{the free surface}, \tag{5.30c}$$

$$\bar{w} = 0 \quad \text{at} \quad \bar{y} = L_{ne}. \tag{5.30d}$$

The solution of the Poisson's Equation on the micro region is also performed by spectral element method which uses one quadrilateral element and again discretized by 77 × 77 number of GLL nodes. The resultant distribution of the axial velocity, w, on the micro region can be seen in Figure 5.6.

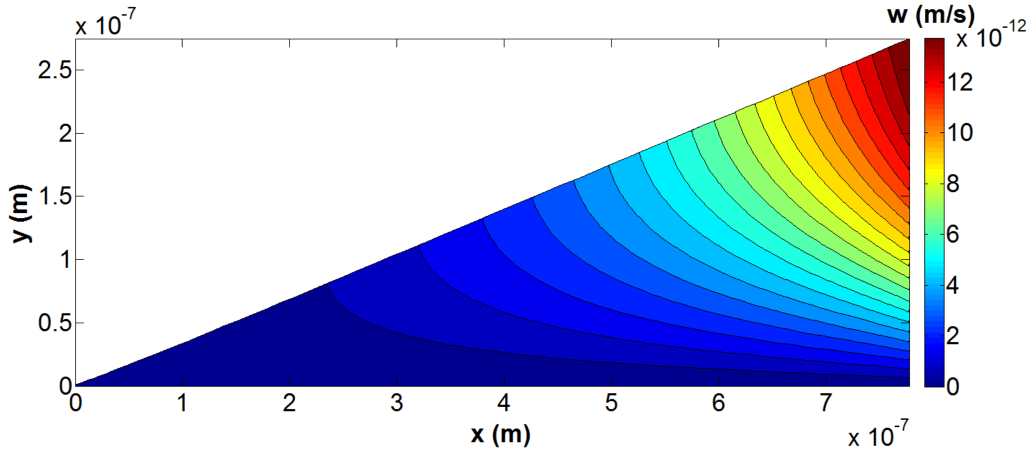

Figure 5.6: Axial velocity distribution in the micro region

5.3 Evaluation of the Results

From the distribution of the axial velocity shown in Figure 5.6, the amount of fluid flowing across the micro region is calculated as approximately 10^{-21} kg/s. It was stated that, solution of the axial velocity contains the information of the pressure gradient in the axial direction and this information was taken from the study of Odabaşı [43] by using the radius distribution found in that study. The step size between the two successive cross-sections was approximately 1 mm. Then, the pressure gradient was estimated between two the cross-sections, separated by 1 mm. Total evaporated liquid for the unit depth of the micro region was calculated as 4.5612×10^{-6} kg/s·m . Considering 1 mm step sizes in the axial direction, total evaporated mass in one step can be calculated as 4.5612×10^{-9} kg/s.

When the axial mass flow and total evaporative flow is compared, the ratio of the axial flow to the supply of liquid which evaporates in the micro region, is about 2×10^{-13}. This ratio shows that axial flow does not bring a considerable amount of liquid to the micro region and all of the fluid evaporated in the micro region is supplied from the undisturbed bulk meniscus region.

CHAPTER 6

PARAMETRIC STUDY

Unlike most of the studies in the literature, Stephan and Busse [31] shared almost all of the parameters that were used in their analysis. In order to make a reasonable comparison with an existing study, parameters and the geometry of the study of Stephan and Busse [31] were used in this thesis. Table 2.1 and Table 3.1 summarize the geometry and physical parameters of the problem which match those of the reference study. As can be seen from the Table 3.1, initial conditions of the current study are film thickness ($\delta = 0.282\,\mu\text{m}$), apparent contact angle ($\theta = 19.7°$) and radius of curvature ($R = 909\,\mu\text{m}$).

The values of the apparent contact angle and radius of curvature are directly taken from the reference study [31]. However, the information about the geometry of rectangular groove cannot be directly taken from the reference study because Stephan and Busse used a triangular groove geometry in their study. Therefore, the geometry of the rectangular groove used in the present study is determined to match the study of Stephan and Busse. For a rectangular groove, the half width of the groove geometry is a function of contact angle and radius of curvature:

$$b = \cos(\theta)R. \tag{6.1}$$

The depth of the groove is taken equal to the width of the groove for the simplicity.

In addition to the case of Stephan and Busse, the present study aims to test different cases to understand the behaviour of the developed model for different superheats, contact angles and physical properties. It should be noted that parametric study is performed considering only unidirectional flow based evaporation model due to the fact that contributions of the flow in other directions are found to be negligible in the previous chapter of this thesis.

6.1 Effect of Superheat

Superheat is the difference between the temperatures of the vapor phase and the solid wall on which evaporating liquid film exists. In the previous chapters, a 1 K superheat is used for the analyses. This temperature difference can be categorized as a high superheat value considering the studies in the literature. Furthermore, evaporation model of Wayner fails for superheats higher than 5 K [36]. Therefore, superheats higher than 1 K were not studied. However, small superheats are widely used in the evaporation analyses in the literature such as [26], [27] or [28]. Therefore, the present study tests different superheats which are equal and smaller than 1 K.

In Figure 6.1, film thickness variations of the systems which have different superheats, are shown. Moreover, variations of film thickness near the contact line are given in a blown up plot in Figure 6.1.

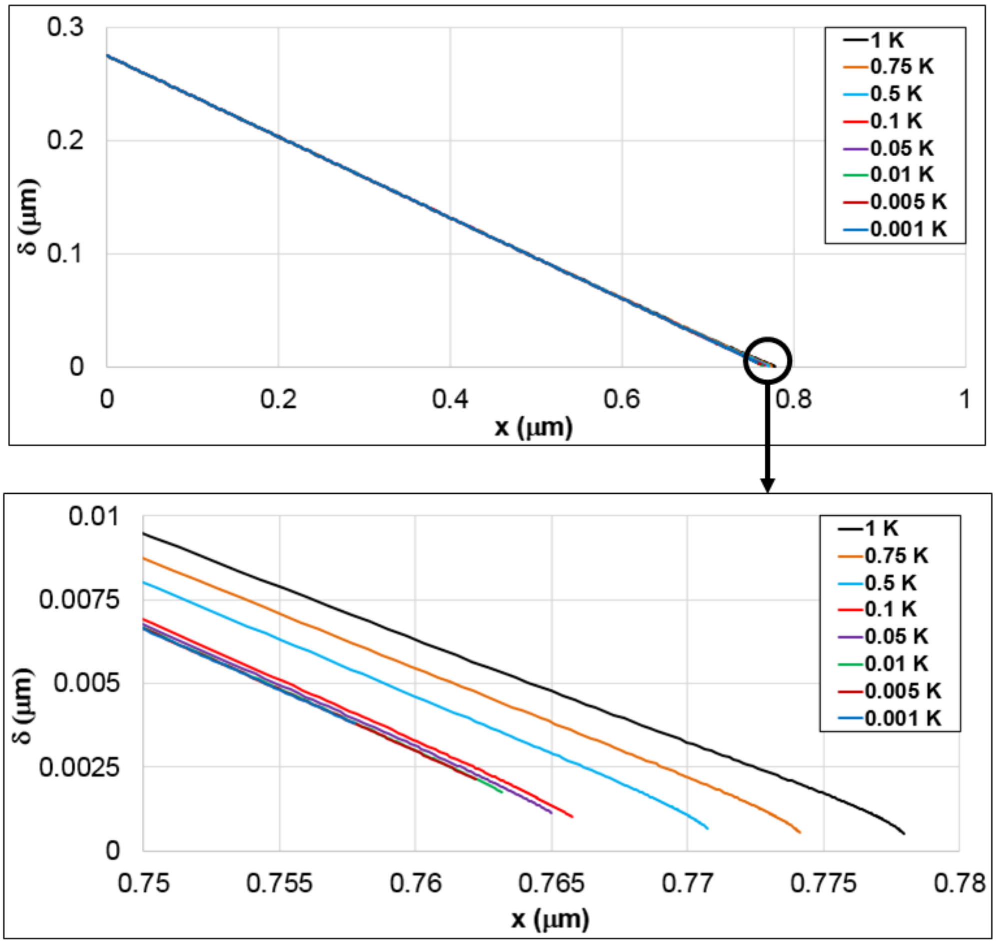

Figure 6.1: Variations of film thickness for different superheats

The first observation from Figure 6.1 is that the extension of the meniscus contracts with decreasing superheat. Thus, the length of the micro region becomes smaller. The thickness of the contact line, on the other hand, increases with decreasing superheat, as expected. The magnitude of the disjoining pressure decreases with increasing film thickness. Thus, systems which have lower superheats, are subjected to reduced disjoining pressures. As a result of this, the bending of the curves becomes less apparent at the contact line for reduced superheats and the systems which have superheats smaller than 0.1 K, cannot be distinguished in Figure 6.2. Therefore, the systems having superheats less than 0.1 K are grouped and they are evaluated separately from the systems which are subjected to large superheats. On the other hand, superheats of 1 K, 0.75 K or 0.5 K are meaningful in case of the engineering applications of heat pipes. Besides, utilization of extremely small superheats helps only to understand the underlying physical phenomena, where experimental data is also available in literature. In the rest of the parametric study, superheats are divided to groups of small and large superheats for these reasons.

In Figure 6.2, film thickness variations of small superheated systems are shown in a close-up view. Even at this magnification, the systems which are subjected to 0.01 K, 0.005 K and 0.001 K superheats, cannot be distinguished from each other, easily. To overcome this difficulty, a marker is placed at the contact line of each profile. The highest contact line has the lowest superheat. Moreover, the contraction of the length of the micro region can be seen from Figure 6.2.

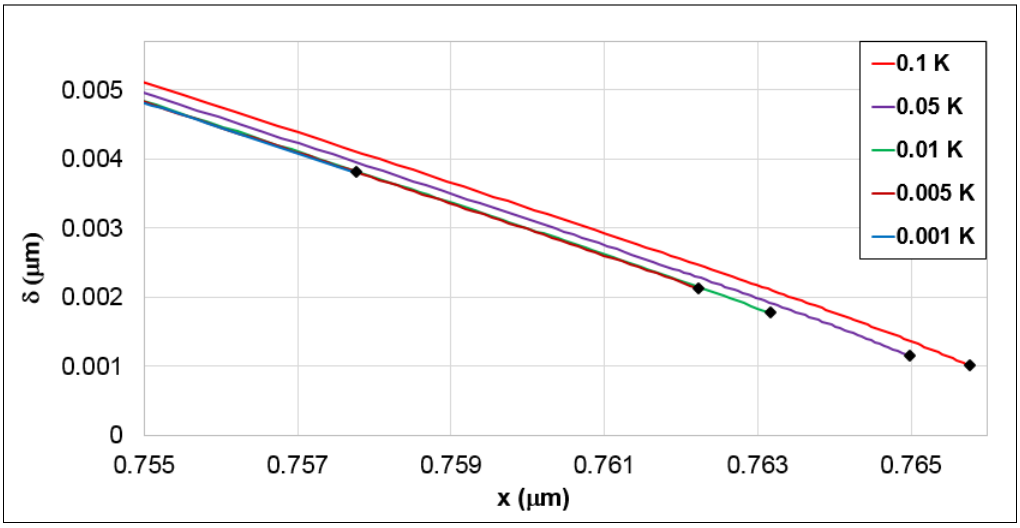

Figure 6.2: Variations of film thickness for small superheats near contact line

Summary of the film thickness variations at the contact line for different superheats are given in Figure 6.3.

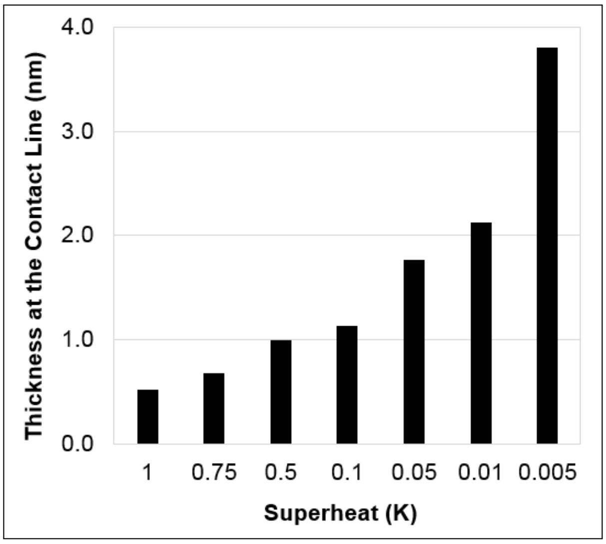

Figure 6.3: Film thicknesses at the contact line for different superheats

A natural consequence of the lower superheat is a reduction in the total evaporated mass within the micro region. The total evaporated masses in the micro region normalized with respect to the value for a 1 K superheat, are shown in Figure 6.4.

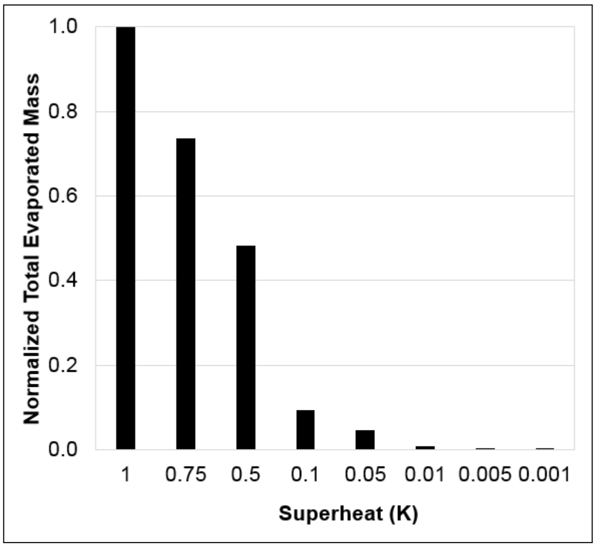

Figure 6.4: Normalized total evaporated mass for different superheats

In Figure 6.4, the amount of total evaporated mass changes almost linearly with superheat. In order to confirm this linear trend, a scatter plot of the data is given in Figure 6.5 for selected superheats.

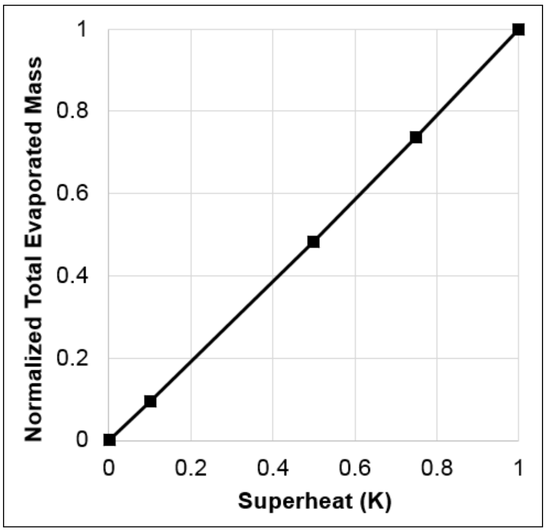

Figure 6.5: Normalized total evaporated mass for selected superheats

It is apparent in Figure 6.5 that the total amount of evaporation in the micro region is a linear function of superheat.

The effect of reducing superheat on the variation of evaporative heat flux within the micro region, on the other hand, can be deduced from Figure 6.6. The resolution of the plot is not sufficient to show the heat flux variation for small superheats, therefore, a blown up plot is also provided in Figure 6.6.

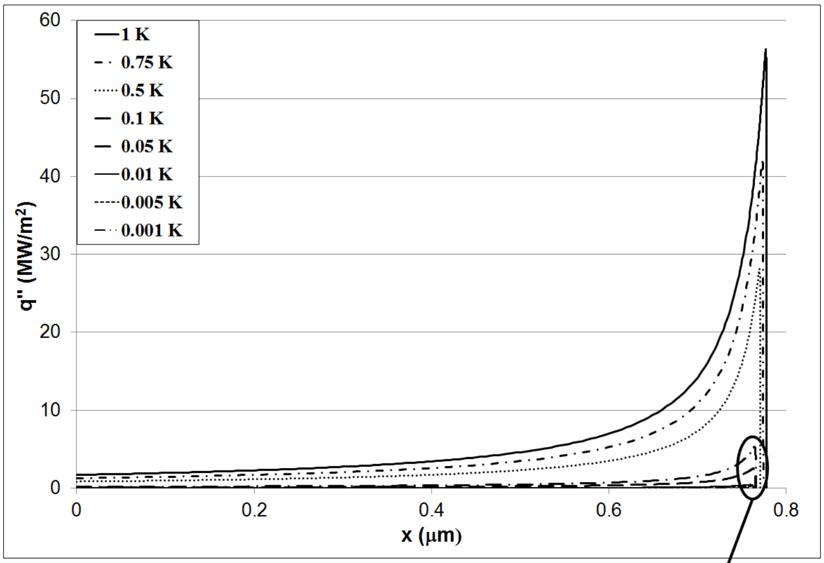

(a) All superheats

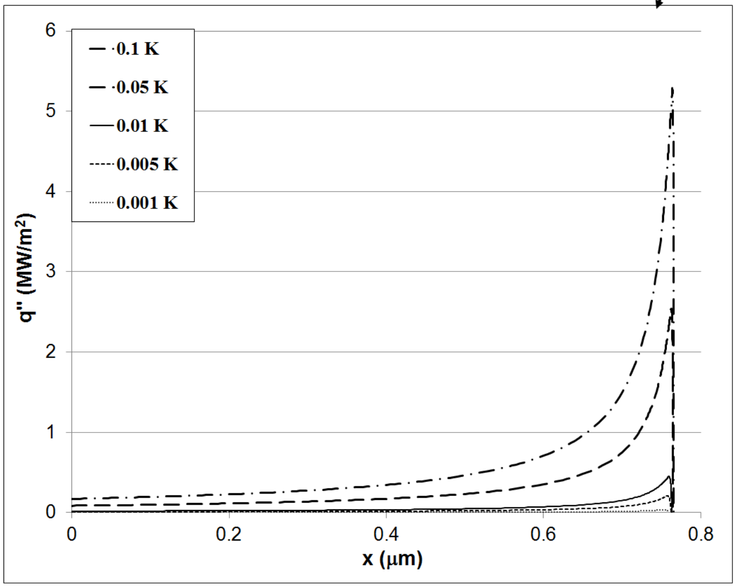

(b) Small superheats

Figure 6.6: Variations of evaporative heat flux for different superheats

It can be seen from Figure 6.6 that evaporation peak drops and peak shape becomes smoother when superheat is reduced. To describe the relation between the superheat and the peak of the evaporative heat flux, Figure 6.7 should be examined.

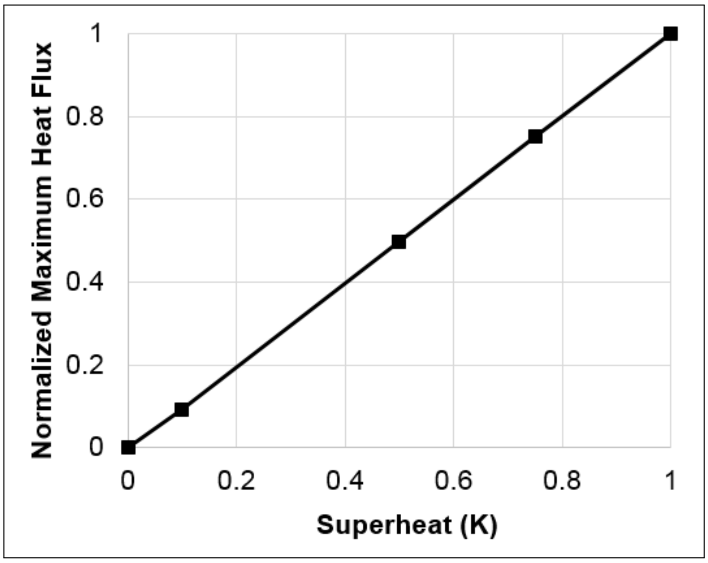

Figure 6.7: Normalized maximum heat flux values for selected superheats

Figure 6.7, in which the peak evaporation of 1 K superheat applied system is taken as the reference for normalization process, shows that the value of the maximum evaporative heat flux in the micro region is also a linear function of superheat.

In addition to the variation of evaporative flux, the variation of cumulative evaporation from the system may also be examined for different superheats. Figure 6.8 shows the cumulative evaporations from the micro region normalized with respect to total for each superheat evaporated mass.

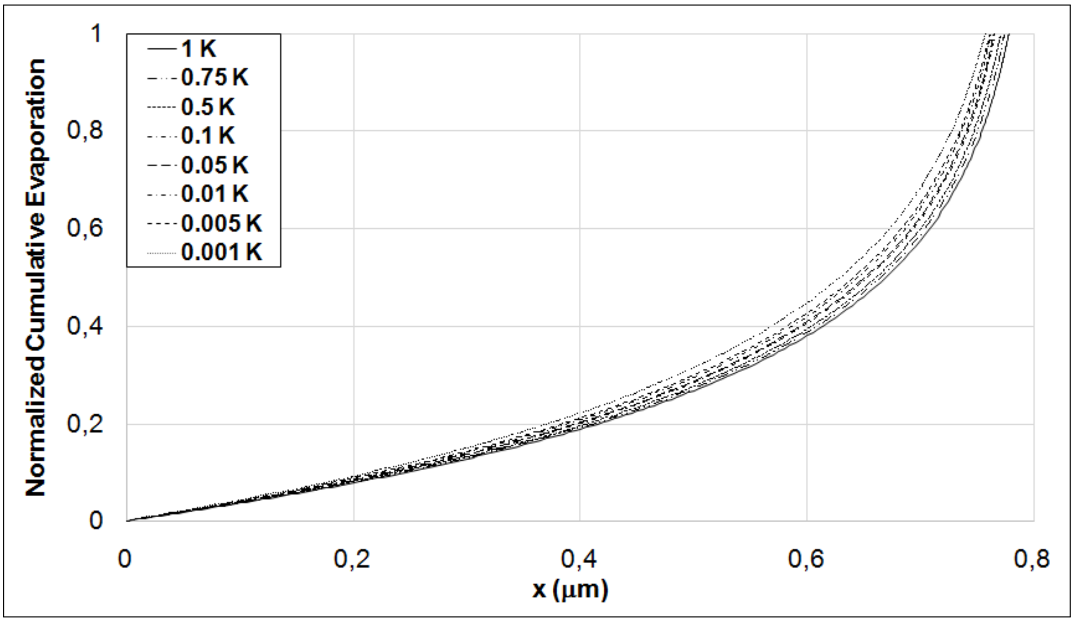

Figure 6.8: Variations of normalized cumulative evaporation for different superheats

It can be seen from Figure 6.8 that normalized cumulative evaporation curves differ from each other due to the different lengths of the evaporating regions. In order to eliminate this difference and explore the trend of the cumulative evaporation for different superheats, the length of the micro region of each system can be normalized. Figure 6.9 shows the normalized evaporation with respect to the normalized x span for different superheats.

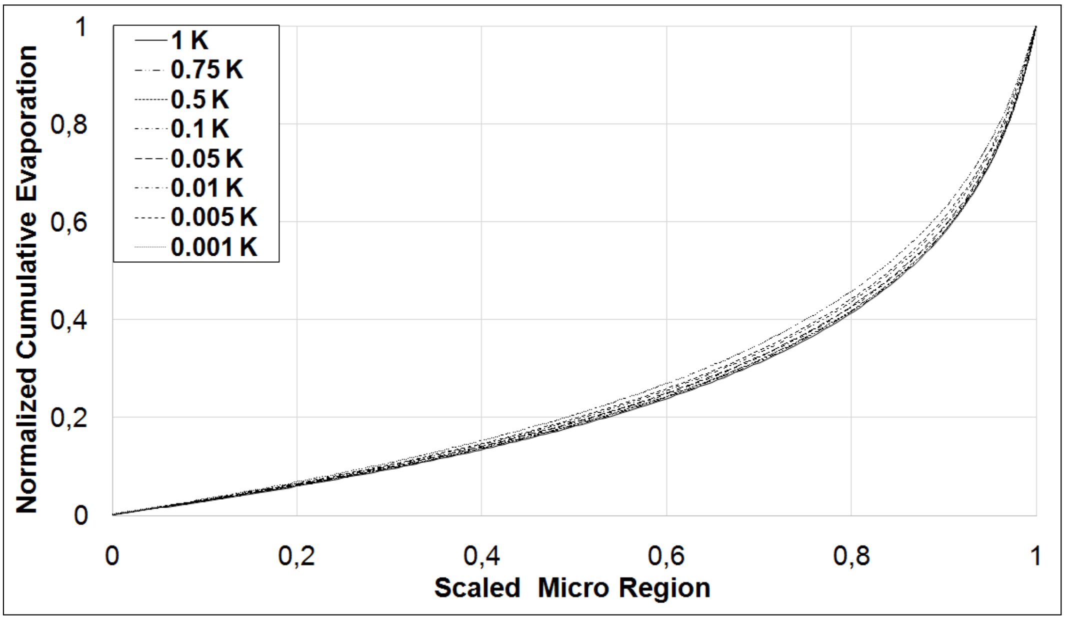

Figure 6.9: Variations of normalized cumulative evaporation in the scaled micro region for different superheats

It can be deducted from Figure 6.9 that although there is no considerable difference between cumulative evaporation curves of different superheats, in the higher ones, contribution to evaporation near the contact line or near the peak point of the evaporative flux, is larger. One can also see that the dominant contribution to evaporation occurs in the vicinity of the contact line.

The balance between disjoining and capillary pressures determines the liquid pressure in the flow. The effect of different superheats on these pressures should also be investigated.

Disjoining pressure variations of the systems for different superheats are shown in Figure 6.10. Note that disjoining pressure is only effective at the close proximity of the contact line, therefore, Figure 6.10 only reports results in this restricted region.

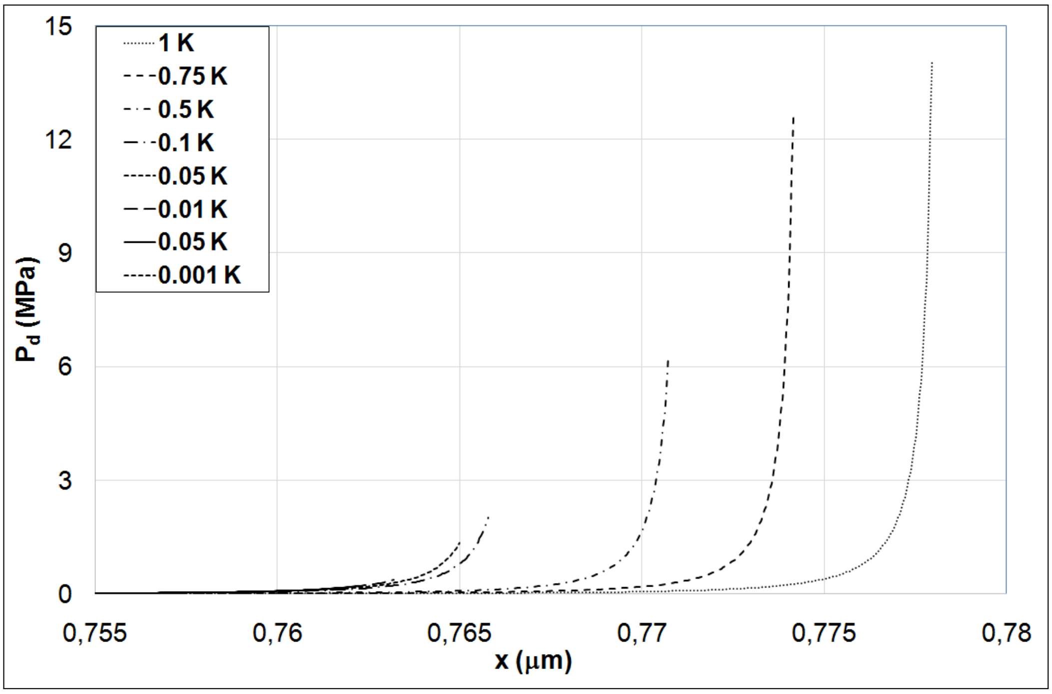

Figure 6.10: Variations of disjoining pressure for different superheats

Being an inverse function of the film thickness, disjoining pressure decreases in systems having small superheat due to increased contact line thickness as shown in Figure 6.10.

Capillary pressure is a function of the radius of curvature of the liquid-vapor surface. The variation of radius of curvature is sufficient to represent the capillary pressure. Furthermore, the radius of curvature directly dictates the shape of the film profile, therefore, examining the radius of curvature instead of capillary pressure helps to understand the shape of the film profile near the contact line. Figure 6.11 shows the variations of radius of curvature for different superheats.

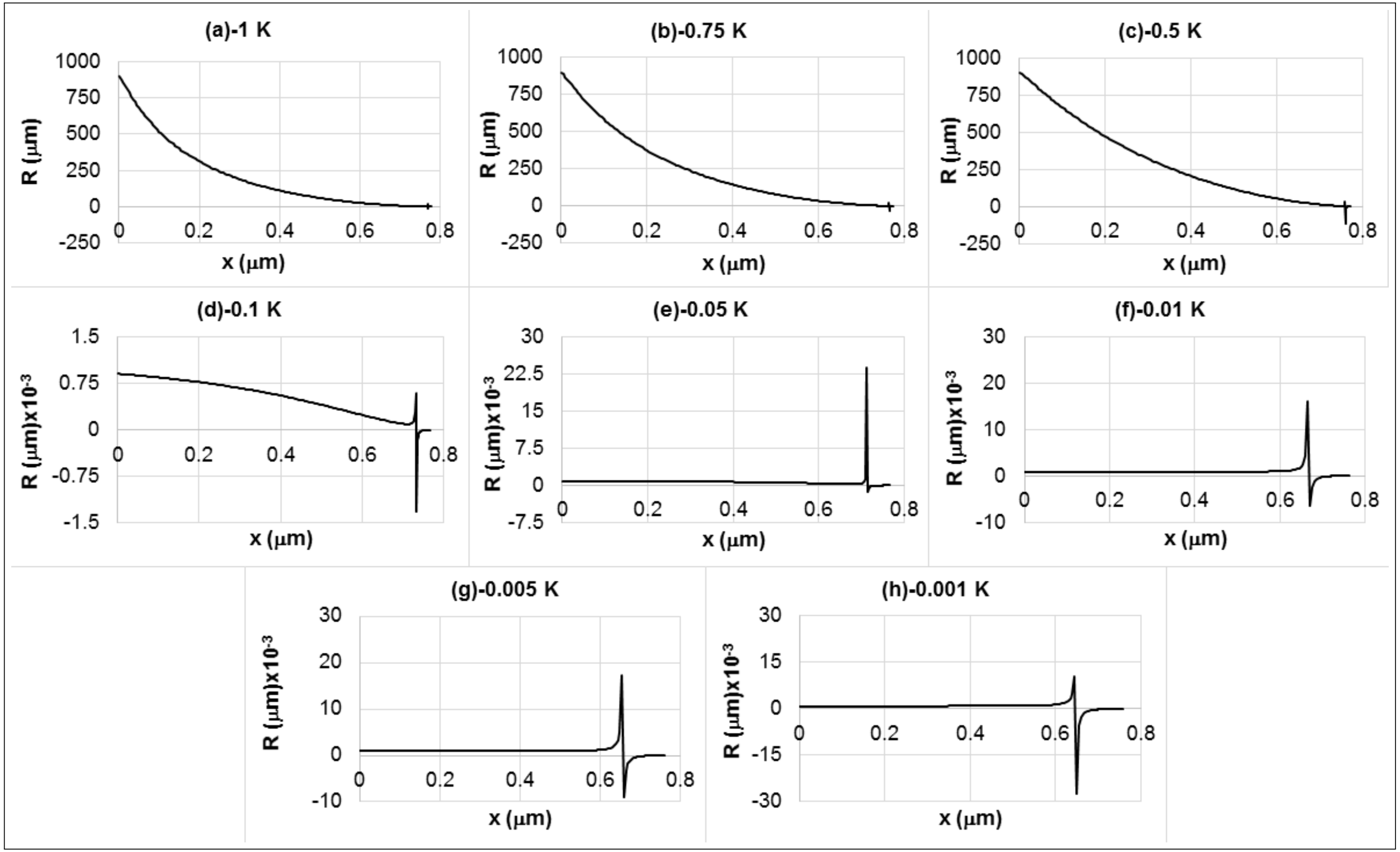

Figure 6.11: Radius of curvature variation for different superheats

The variation of radius of curvature exhibits different trends for small and large superheats. Systems having large superheats have the superheat values of 1 K, 0.75 K and 0.5 K and are shown in Figure 6.11(a) to Figure 6.11(c). Away from the contact line the radius of curvature deforms (decreases) to generate the capillary pumping effect. Near the contact line, on the other hand, disjoining pressure is dominant and disjoining pressure gradient is responsible for supplying the necessary liquid pressure gradient. It can be understood from the small positive peaks of the radius of curvatures in the first three plots of Figure 6.11 that capillary pressure decreases in this region where disjoining pressure is effective. Furthermore, the decrease in capillary pressure is not sufficient to balance the aggressively increasing disjoining pressure and the second derivative of film thickness, δ, changes sign, effectively changing the sign of capillary pressure by bending the film thickness profile towards the solid wall. In Figure 6.11, a small magnitude negative peak follows the small magnitude positive peak for this reason. The system which is subjected to a 0.1 K superheat exhibits a transition trend between the large and small superheats. The systems having small superheats, on the other hand, separate from the larger ones especially in terms of the change of capillary pressure on the undisturbed meniscus side of the close proximity of the contact line. The systems having small superheats have small evaporation rates. Therefore, the amount of fluid flow or liquid pressure gradient is also small for these systems. This small liquid pressure gradient is generated by both capillary and disjoining pressure gradients. Therefore, capillary pressure gradient is not sufficient for generating the liquid pressure gradient. In Figure 6.11(e) to Figure 6.11(h), changes in the radius of curvature, away from the contact line, are not recognizable for this reason. Moreover, positive and negative peaks of the radius of curvature have large magnitudes in the close proximity of the contact line due to the fact that there is no need for high capillary pressures to balance the small disjoining pressures for small superheats.

Variations of liquid, capillary and disjoining pressure gradients for all superheats are summarized in Figure 6.12.

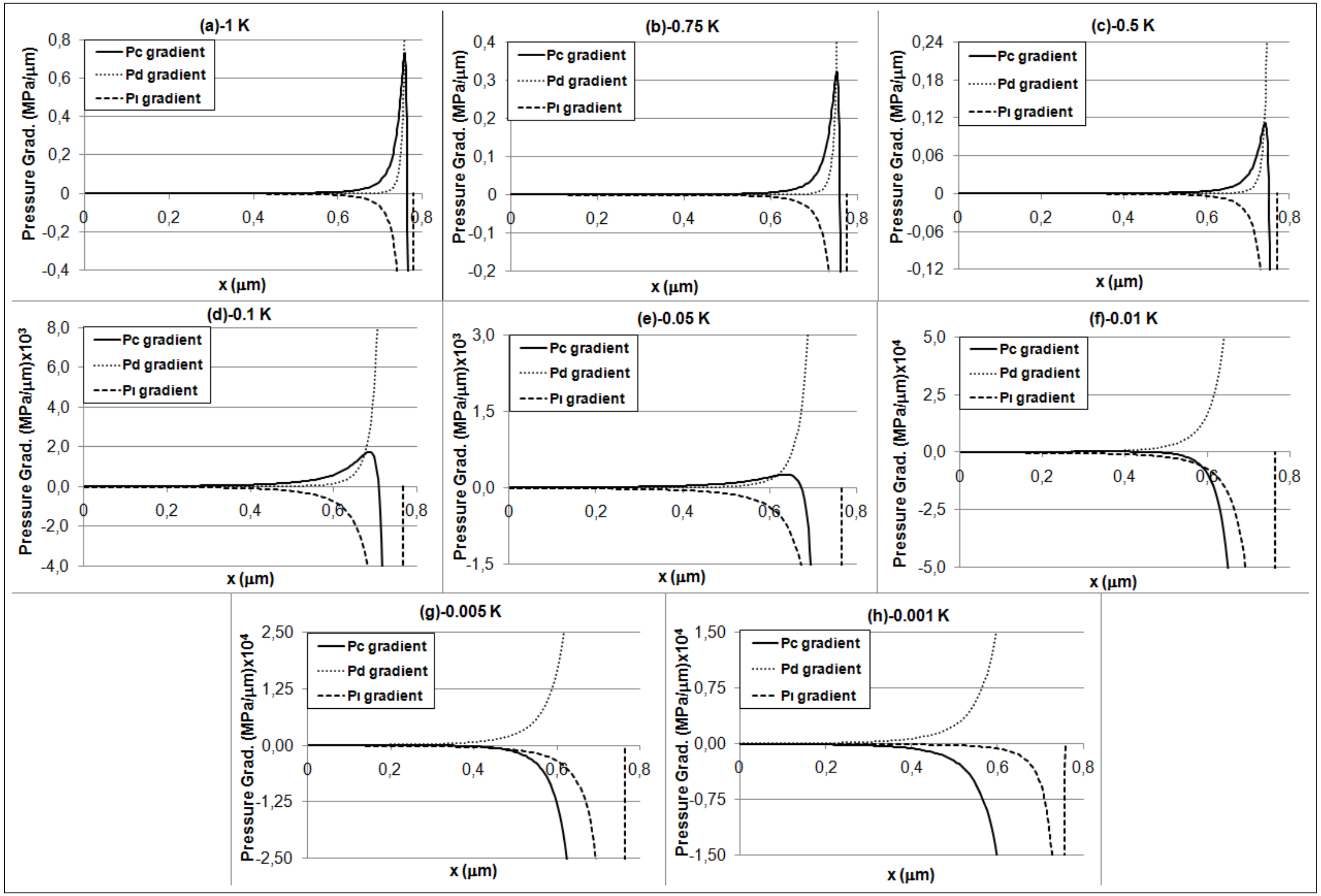

Figure 6.12: Variation of pressure gradients for different superheats

When plots (a) to (e) of Figure 6.12 are examined, it can be seen that the capillary pressure gradient increases from the entrance of micro region until a maximum is reached. In this region, disjoining pressure and the gradient of disjoining pressure are small, therefore capillary pressure gradient drives the liquid flow. When approaching the contact line, on the other hand, the value of disjoining pressure increases due to very thin film thicknesses and its value exceeds that of the capillary pressure. After this point, disjoining pressure gradient dominates the capillary pressure gradient and drives the liquid flow. Moreover, in the close vicinity of the contact line, disjoining pressure reaches extremely high values and in order to counterbalance this effect, capillary pressure becomes negative by the changing sign of the radius of curvature. This mechanism is not valid for the plots (f) to (h) of Figure 6.12 which correspond to extremely small superheats, and evaporations are very small in these cases. Small evaporation requires less liquid flow so that the value of the required pressure gradient is very small. In these cases, the magnitude of disjoining pressure gradient is sufficient to create this liquid pressure gradient. Therefore, capillary pressure gradient does not increase and drive the liquid flow. In the plots (f) to (h) of Figure 6.12, capillary pressure gradient decreases without a sign change for this reason.

Local heat transfer coefficient of evaporation is expressed as evaporative heat flux and superheat as shown in Equation 6.2:

$$h = \frac{q''}{T_w - T_v}. \tag{6.2}$$

Variations of local heat transfer coefficient in the micro region are shown in Figure 6.13 for different superheats. It should be noted that the local heat transfer coefficients are plotted starting from the contact line in Figure 6.13. Moreover, a blown up plot is provided in Figure 6.13 to show the distribution near the contact line.

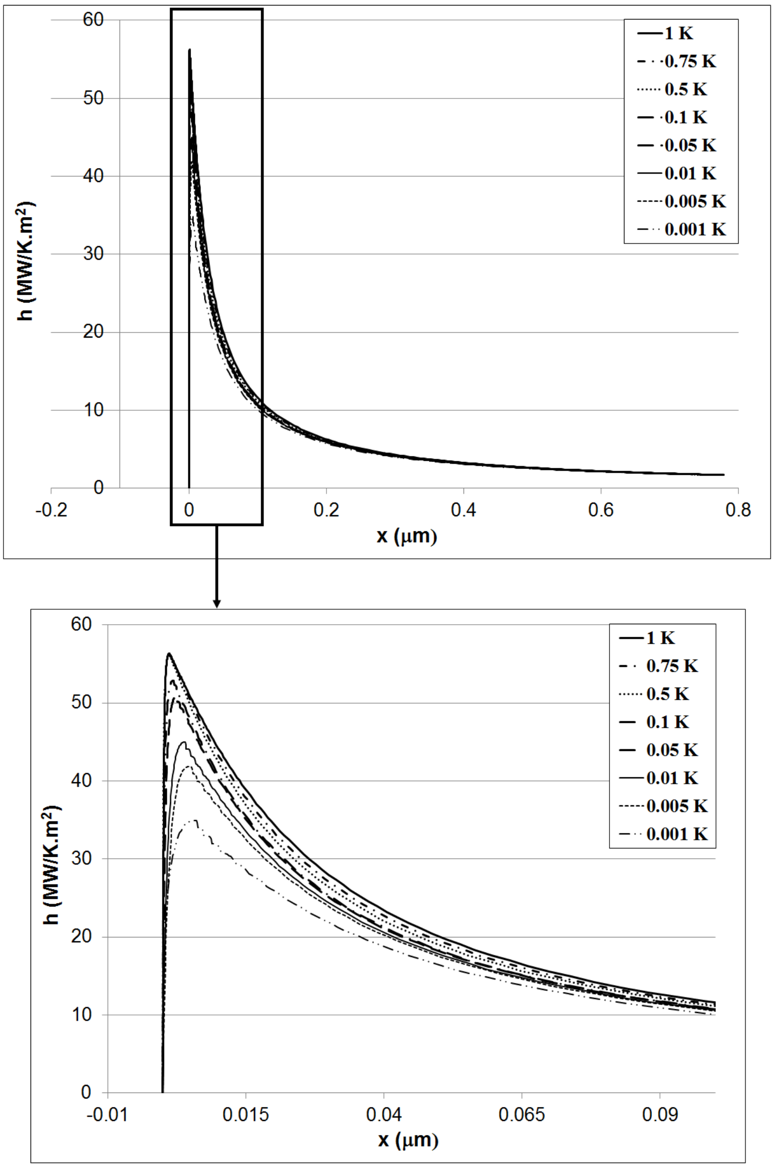

Figure 6.13: Variations of local heat transfer coefficient for different superheats

As shown in Figure 6.13, local heat transfer coefficient increases with increasing superheats. Moreover, the differences between the magnitudes of the local heat transfer coefficients are maximum in the close vicinity of peak evaporation point.

Finally, variations of local Nusselt number are given in Figure 6.14 for different superheats. In this figure, the variation of local Nusselt number is plotted starting from the contact line.

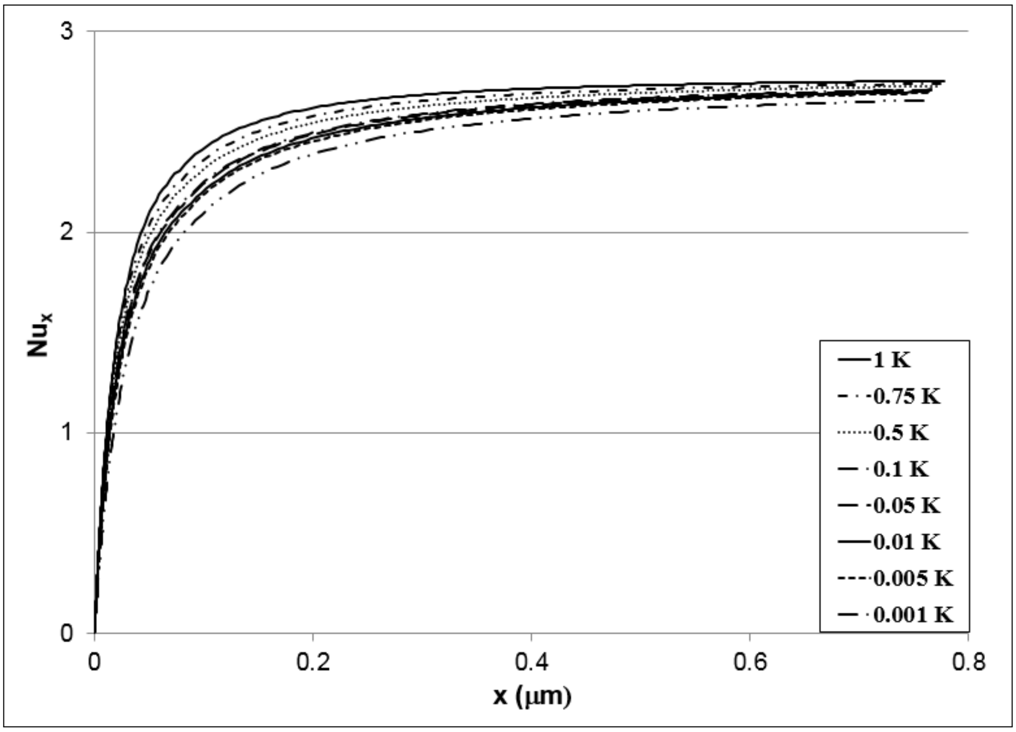

Figure 6.14: Variations of local Nusselt number for different superheats

Similar to the local heat transfer coefficient, local Nusselt number increases with increasing superheats. However, the maximum differences between the magnitudes of the local Nusselt numbers for different superheats do not appear in the close vicinity of the maximum evaporation point as in the case of heat transfer coefficients.

6.2 Effect of Contact Angle

To understand the behaviour of the model for contact angles other than 19.7°, a parametric study is carried out. For five different contact angle values between 10° and 20°, five simulations are performed. Moreover, these analyses are made for one large and one small superheat values to examine the effect of contact angle for different superheats.

6.2.1 Large Superheat

A 1 K superheat is applied to the system and five different contact angles are used in the model developed for the unidirectional flow based evaporation model. However, the developed algorithm for the model cannot solve every different case. When dispersion constant is altered by a definite amount, a solution can be obtained. The reason of this situation actually arises from the definition of the physical problem. A contact angle between a solid wall and a liquid is a property of a system. It means that when all other parameters are fixed, there exists a unique contact angle for a system. It is known that the physical problem defined with the contact angle of 19.7° has a physically realizable solution. In other words, the system having 19.7° contact angle does in fact exist. However, it is not certain that systems constructed with other contact angles are physically possible. On the other hand, by changing the dispersion constant, a physically realizable system may be obtained because the value of dispersion constant is crucial for the evaporation models since it directly determines the value of disjoining pressure. Instead of assigning a value, the magnitude of the dispersion constant is calculated in the experimental studies, by measuring the non-evaporating thickness at the contact line. Actually, dispersion constant is unique to the system because it depends on molecular properties of liquid and solid which are affected by the thermal state of the problem. Furthermore, the geometry of the film thickness, especially slope, also affects the value of the dispersion constant. Therefore, different numerical values for the dispersion constant are tried and the one which enables a solution to all five cases, is selected. The remaining physical parameters are the same as Table 3.1.

The film thickness distributions of the five cases are shown in Figure 6.15.

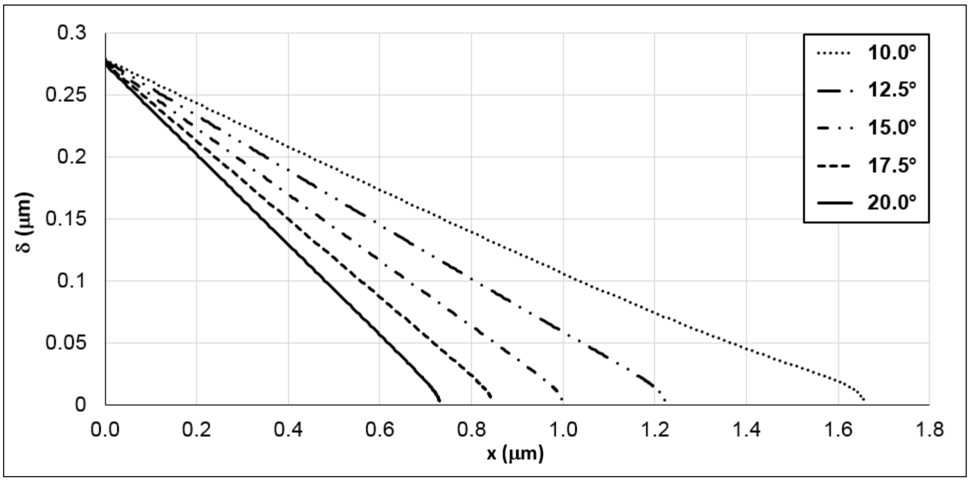

Figure 6.15: Variations of film thickness for different contact angles at 1 K superheat

Similar to the original problem, apparent contact angles are preserved until the close vicinity of the contact line. Thus, when the contact angle is reduced, the range of the evaporation increases, as shown in Figure 6.15.

The distributions of the evaporative flux for the five cases are shown in Figure 6.16.

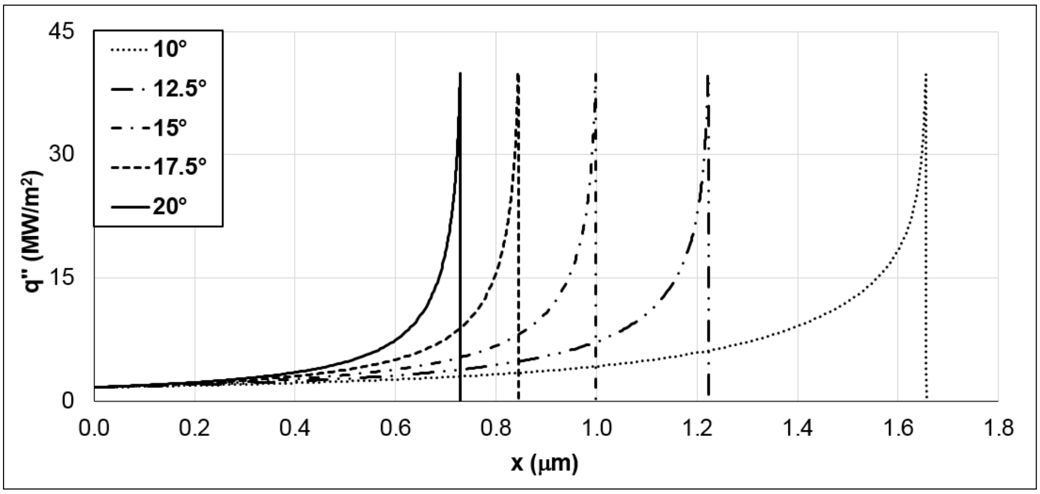

Figure 6.16: Variations of evaporative heat flux for different contact angles at 1 K superheat

The peak value of the evaporative heat flux curves of the all cases are approximately the same as shown in Figure 6.16. Then, the case which has the smallest contact angle, should have the maximum total evaporation due to the fact that it has the longest evaporation distance. Total amount of heat transfer for the five cases can be seen in Figure 6.17.

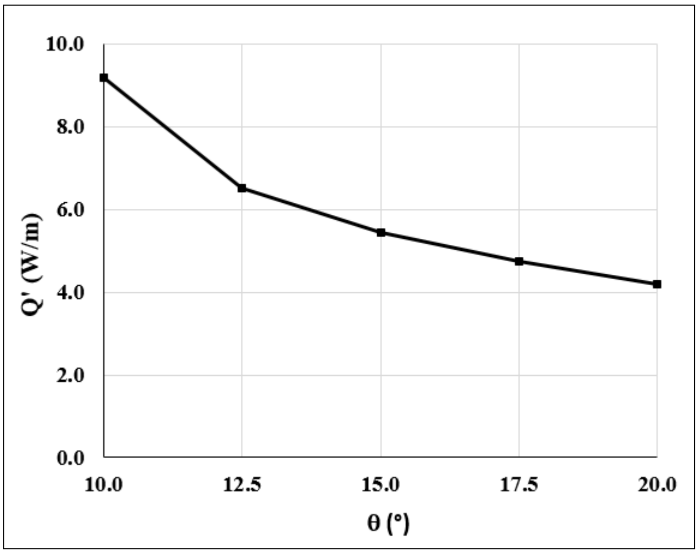

Figure 6.17: Total heat transferred for different contact angles at 1 K superheat

In addition to variation of evaporative heat flux, variation of cumulative evaporation is presented for different contact angles of when the system is subjected to 1 K superheat. To eliminate the difference arising from the length of evaporation, the length of the micro region is normalized for each system in the results. Furthermore, cumulative evaporation of each system is also normalized to understand the trend of cumulative evaporation for different contact angles. Figure 6.18 shows the normalized evaporation with respect to the normalized x span for different contact angles.

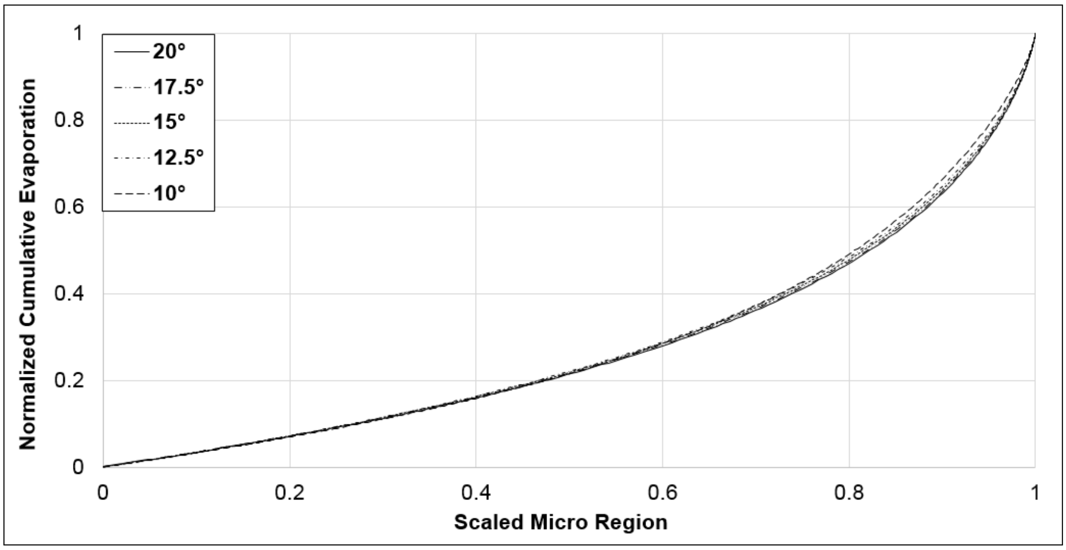

Figure 6.18: Variations of normalized cumulative evaporation in the scaled micro region for different contact angles at 1 K superheat

It can be deducted from Figure 6.18 that although there exists no considerable difference between cumulative evaporation curves of the systems having different contact angles, contribution to evaporation near the contact line is larger for large contact angles.

Variations of liquid, capillary and disjoining pressure gradients for different contact angles of 1 K superheat applied system are shown in Figure 6.19 which reveals that the contribution of capillary pressure gradient to the liquid pressure gradient increases with smaller contact angles because systems which have smaller contact angles, have small disjoining pressure gradient due to their low slopes.

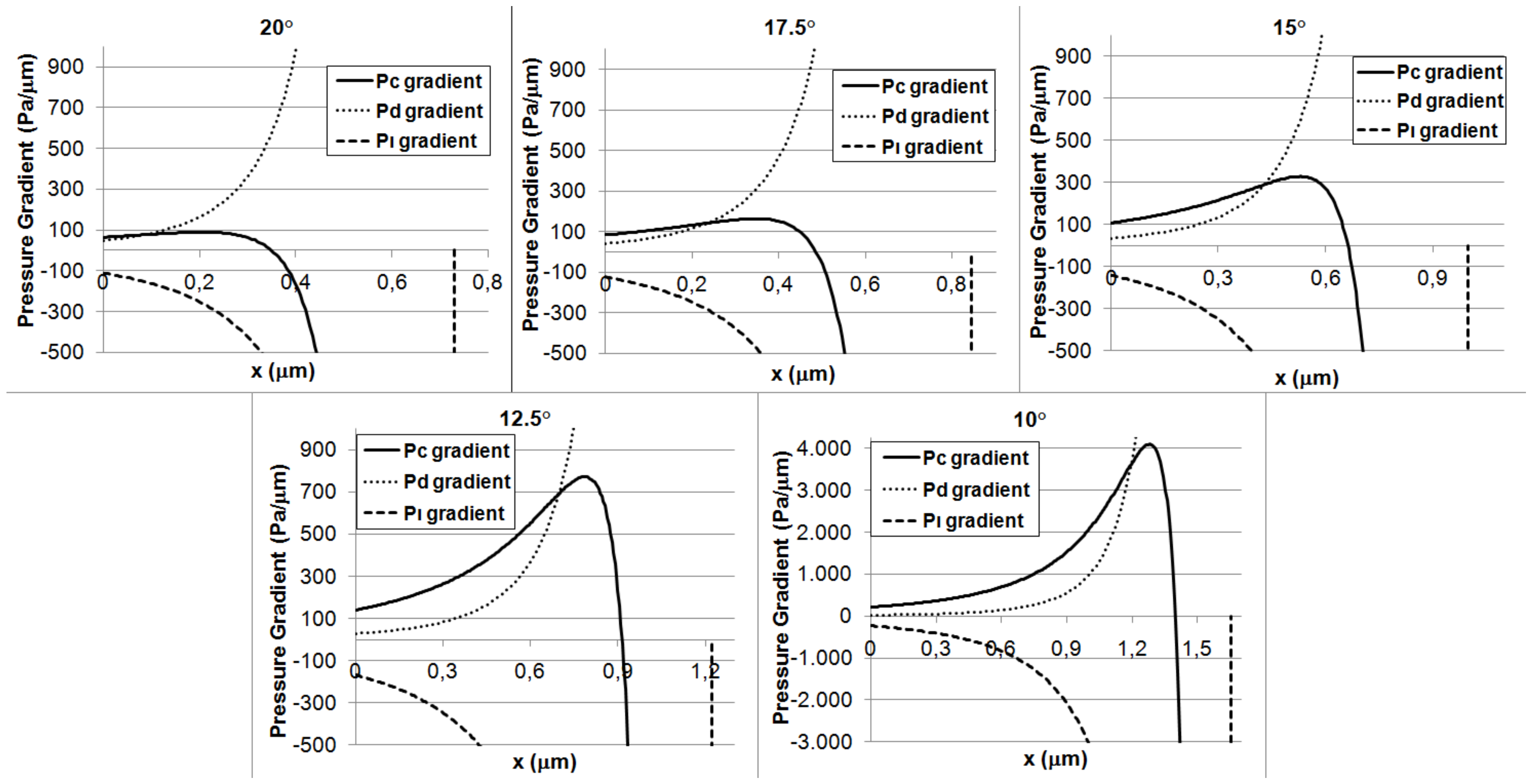

Figure 6.19: Variation of pressure gradients for different contact angles at 1 K superheat

6.2.2 Small Superheat

In this part of the parametric study, effect of contact angle is investigated for the system subjected to 0.01 K superheat. The same value of dispersion constant is used as the one used in large superheat case. Film thickness distributions corresponding five different contact angles, are shown in Figure 6.20.

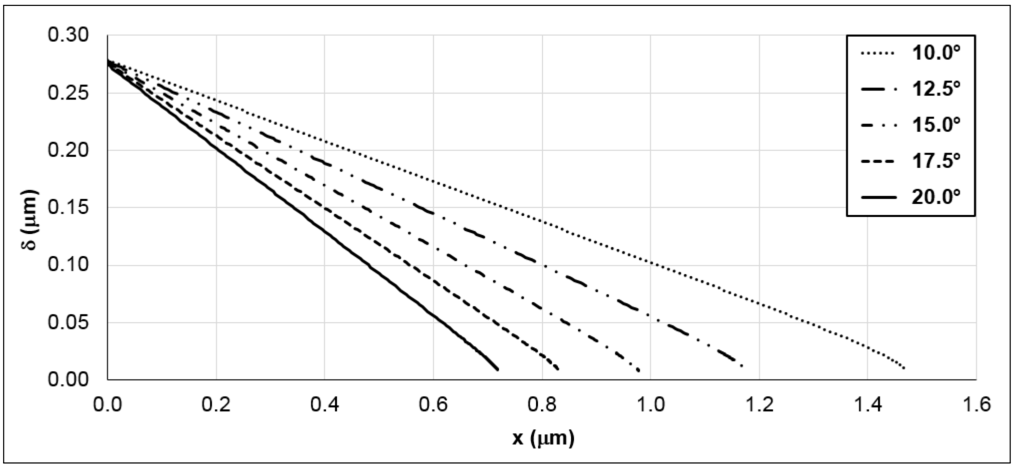

Figure 6.20: Variations of film thickness for different contact angles at 0.01 K superheat

Variations of film thickness for the small superheat condition is similar to the ones obtained for large superheat condition except the length of the micro regions. Reduced evaporation leads to a decrease in the extension of the meniscus and micro region lengths when the corresponding contact angles are reduced.

The distributions of the evaporative flux for the five cases are shown in Figure 6.21.

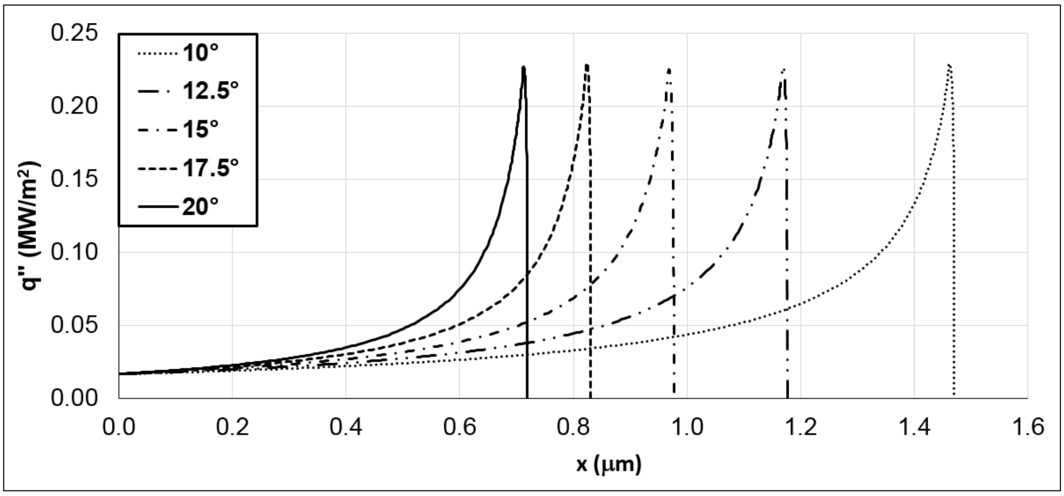

Figure 6.21: Variations of heat flux for different contact angles at 0.01 K superheat

Similar to the analysis made for the large superheat, the peak values of the evaporative heat flux curves of the all cases are approximately equal as shown in Figure 6.21. Then, the case which has the lowest contact angle, has the maximum total evaporation due to the fact that it has the largest evaporation distance. Total amount of heat transferred for the five cases can be seen in Figure 6.22.

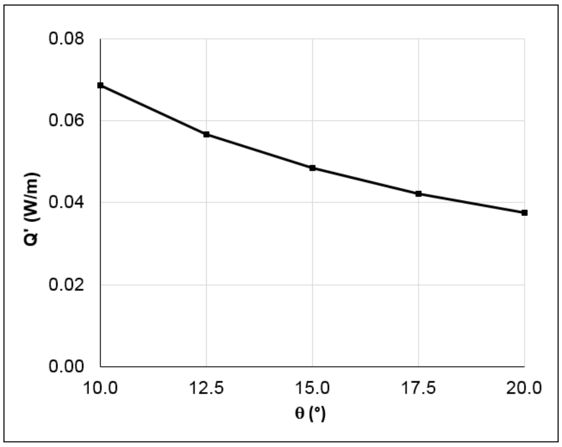

Figure 6.22: The total heat transferred for different contact angles at 0.01 K superheat

Figure 6.23 shows the normalized evaporation with respect to the normalized x span for different contact angles when the system is subjected to small superheat.

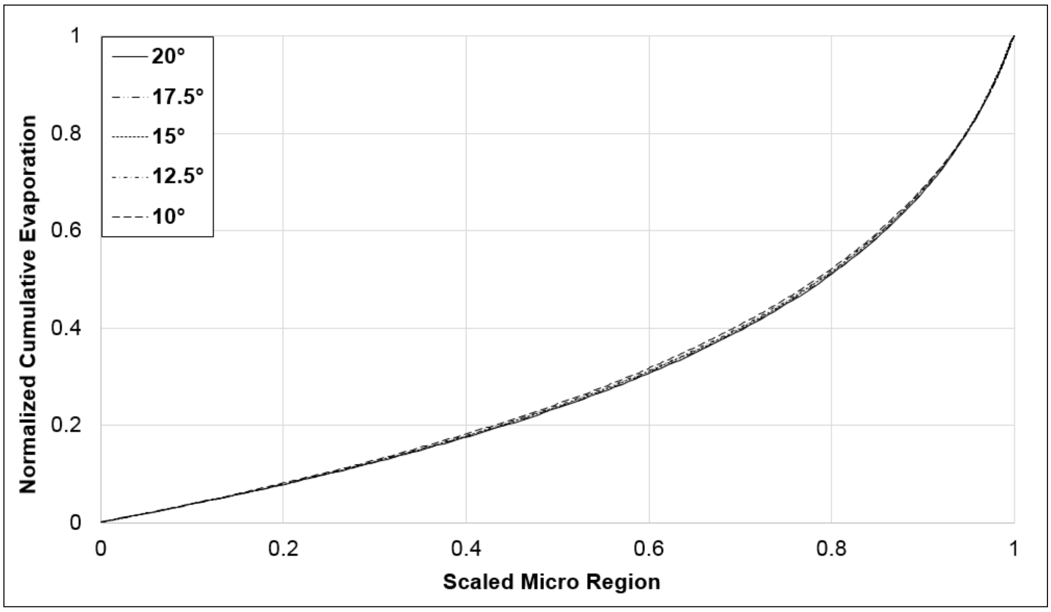

Figure 6.23: Variations of cumulative evaporation in the scaled micro region for different contact angles at 0.01 K superheat

The differences between the cumulative evaporation curves of the systems having different contact angles are less apparent in Figure 6.23 when compared with the large superheat case presented in Figure 6.18.

Finally, variations of liquid, capillary and disjoining pressure gradients for different contact angles of 0.01 K superheat applied systems are shown in Figure 6.24.

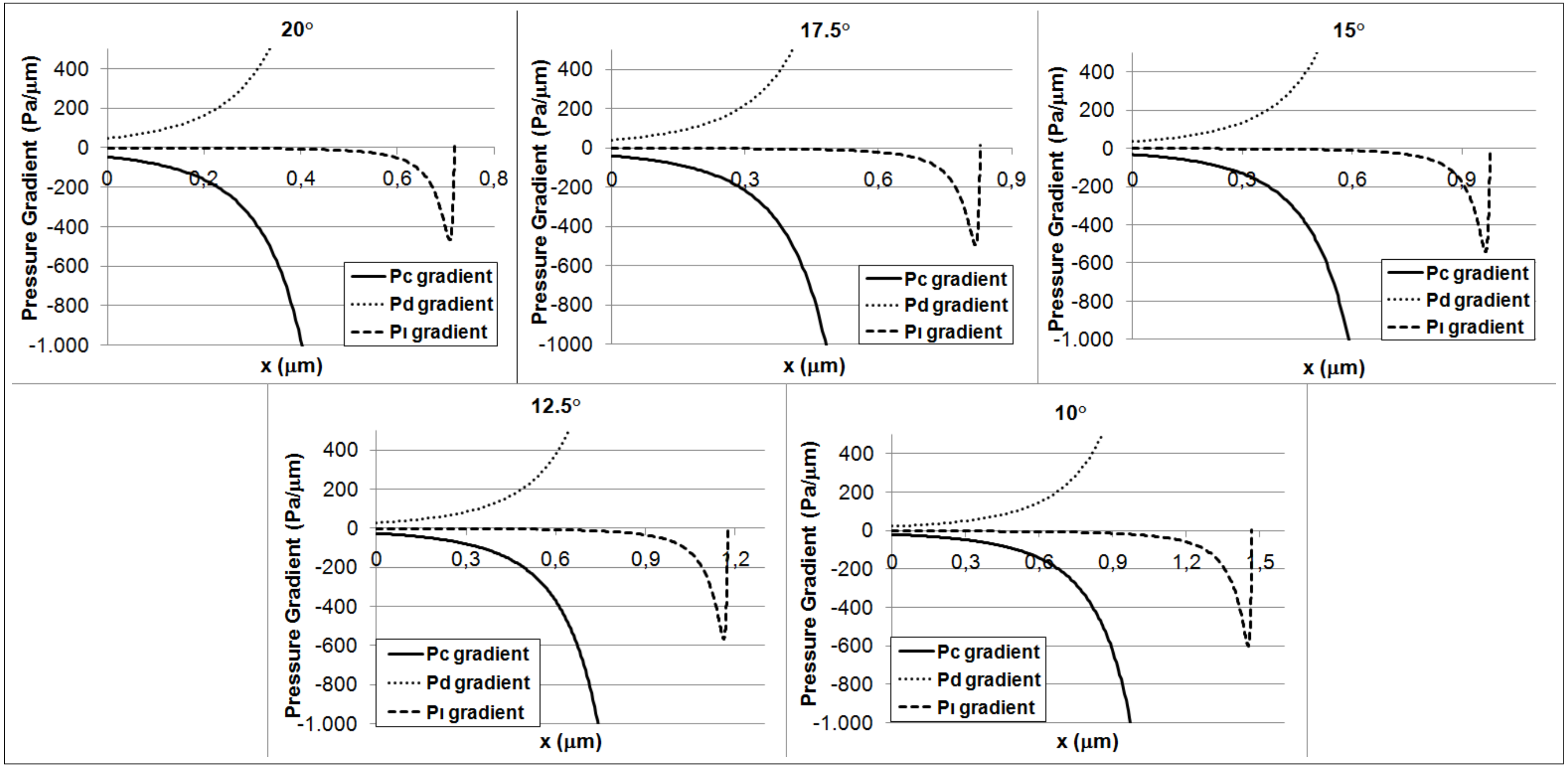

Figure 6.24: Variation of pressure gradients for different contact angles at 0.01 K superheat

As can be seen in all individual plots of Figure 6.24, capillary pressure gradient is always negative for all contact angles. This means that disjoining pressure gradient drives the flow instead of capillary pressure gradient. The reason for this mechanism is due to the fact that evaporation is sufficiently small for this small superheat. Moreover, increased dispersion constant for the analyses also suppresses evaporation. Thus, there exists very small mass flow and liquid pressure gradient. The changes in disjoining pressure even at large film thicknesses dominate the liquid pressure gradient such that capillary pressure gradient has virtually no effect.

6.3 Effect of Physical Properties

As the third part of the parametric study, ammonia is replaced by another working liquid, keeping all other parameters the same. Although various kinds of liquids were used in the literature, their properties, which are defined at the thermal and geometrical conditions corresponding to the system used in these studies, were not completely available. The only liquid whose properties are available at different states is water. Therefore, water is chosen as the alternative fluid in the problem to be used instead of ammonia. It should be noted that water shows strong polarity and Equation 2.8 should be used instead of Equation 2.7 to formulate the disjoining pressure. Both formulations are used to compare the effect of using different disjoining pressure models. The difference of total evaporated mass between the two models for 1 K superheat is estimated to be only 0.337%. Due to this small difference, different disjoining models are not used in the rest of the parametric study.

6.3.1 Large Superheat

When ammonia is replaced by water and 1 K superheat is applied, variations of the film thickness and evaporative heat flux are shown in Figure 6.25 and Figure 6.26, respectively.

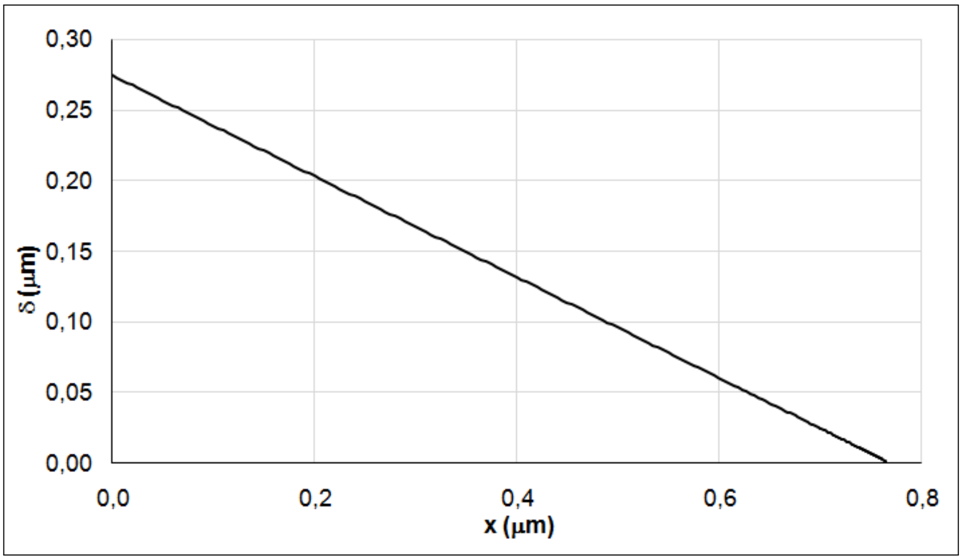

Figure 6.25: Variation of film thickness for water

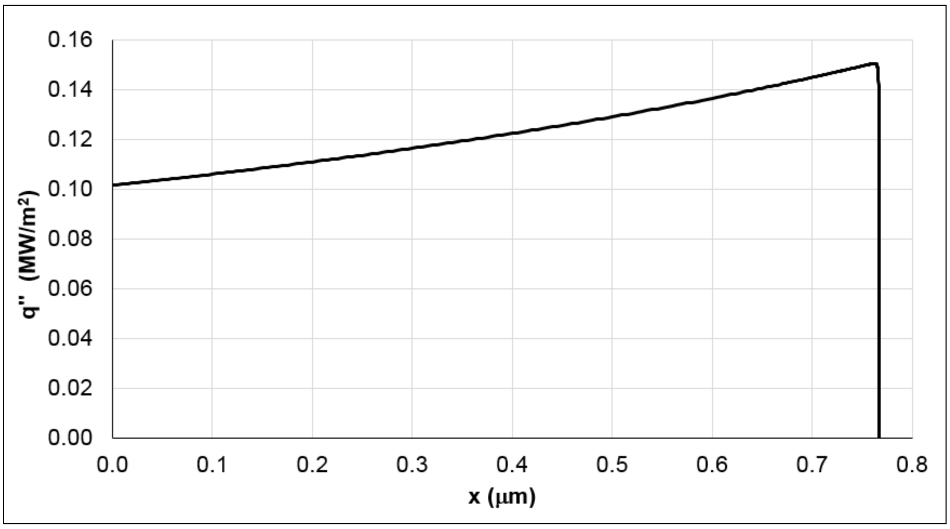

Figure 6.26: Variation of evaporative heat flux for water

In order to compare the effect different working fluids, results should be reported on the same figures for water and ammonia. However, when Figure 6.25 is examined, the film thickness profiles are very close to each other except in the close proximity of the contact line. Therefore, the comparison between the film profiles of water and ammonia is made in the close proximity of the contact line in Figure 6.27.

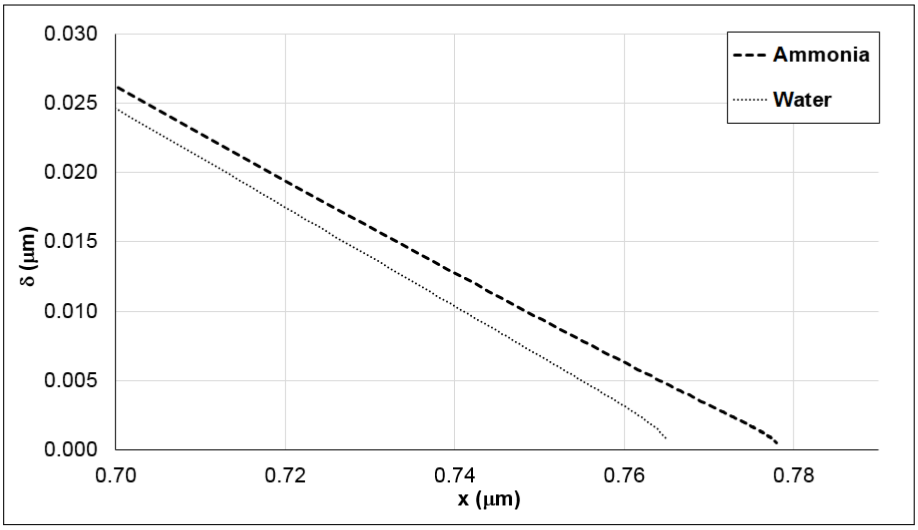

Figure 6.27: Variations of film thickness for water and ammonia

Replacing ammonia with water results in approximately a 10 nm decrease in the length of the micro region as shown in Figure 6.27.

Similar to the film thickness, profiles of the variation of evaporative heat flux for both water and ammonia utilizing systems should be displayed on the same figure. However, the magnitudes of the heat fluxes of water and ammonia have different orders due to their different properties, especially the latent heat of evaporation. Moreover, the lengths of the micro regions of these systems are also not equal. Therefore, both heat fluxes and micro region lengths of water and ammonia utilizing systems are normalized and given in Figure 6.28.

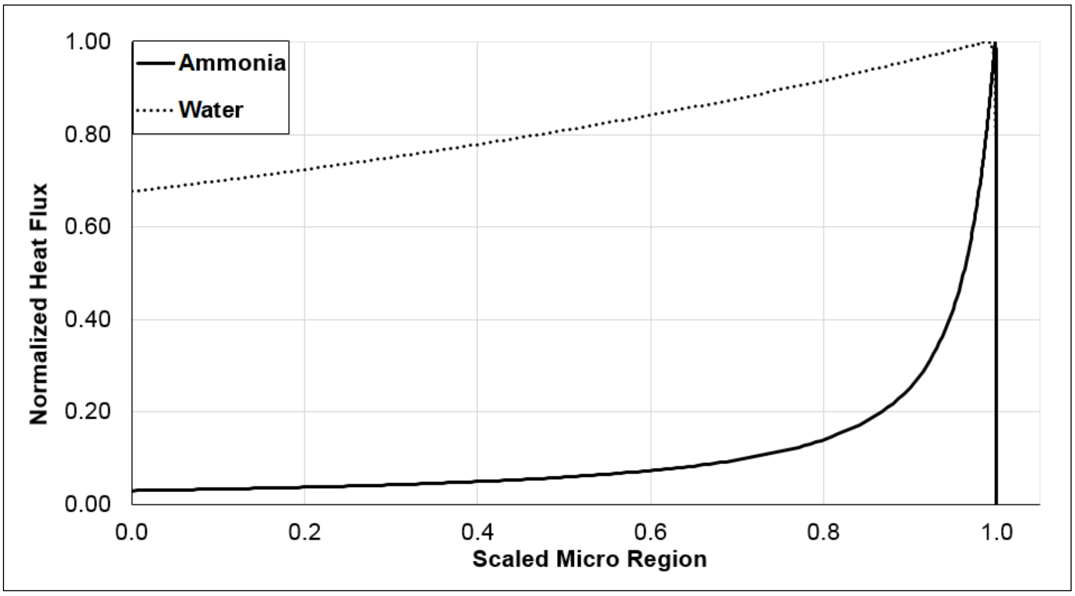

Figure 6.28: Variations of normalized heat flux in the scaled micro region for water and ammonia

The parametric studies made in the present study always show that the contribution in the vicinity of peak heat flux to the total evaporation is high for ammonia utilizing system. However, when the ammonia is replaced by water, variation of heat flux shows a linear trend when approaching the peak point as shown in Figure 6.28. Moreover, magnitude of the normalized evaporative heat flux is larger for water at the inlet of the problem domain. These findings show that for a water system, an earlier starting point should be selected to achieve an evaporative heat flux distribution similar to ammonia system.

Although Figures 6.25 to 6.28 show expected trends without exhibiting any inconsistency, the absolute liquid pressure of the system drops below zero by creating a physical conflict. The liquid pressure of the system is given with capillary and disjoining pressures in Figure 6.29. Moreover, the constant vapor pressure is also added to Figure 6.29.

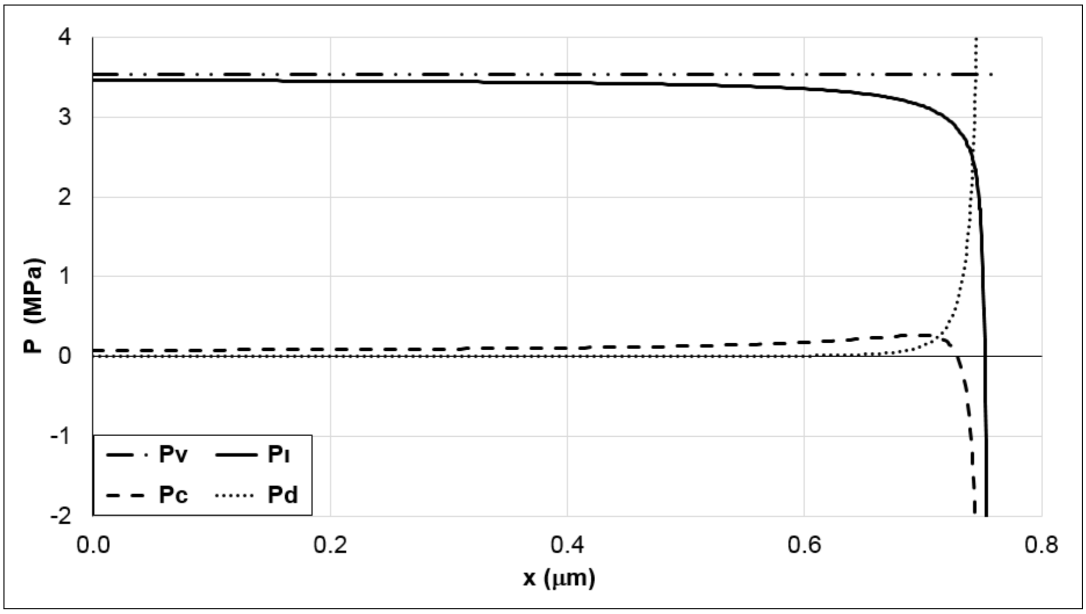

Figure 6.29: Variations of pressures for the system using water

It can be easily detected from Figure 6.29 that absolute liquid pressure becomes negative within the problem domain. The reason for this non-physical situation arises again from the definition of the problem. A water-aluminium system having 19.7° apparent contact angle and 909 μm radius of curvature values at the film thickness of 0.282 μm may never form a stable evaporating meniscus at a temperature of 300 K. To perform a realistic analysis, the problem should be carefully defined. Therefore, it can be concluded that analytical approach should be coupled with experimental work to have a realistic model of the system.

6.3.2 Small Superheat

To investigate the effect of small superheat on water utilizing system, 0.01 K superheat is applied to the system.

Due to the fact that variations of film thicknesses of water and ammonia utilizing systems are very close, the comparison between them is made in the close proximity of the contact line as shown in Figure 6.30.

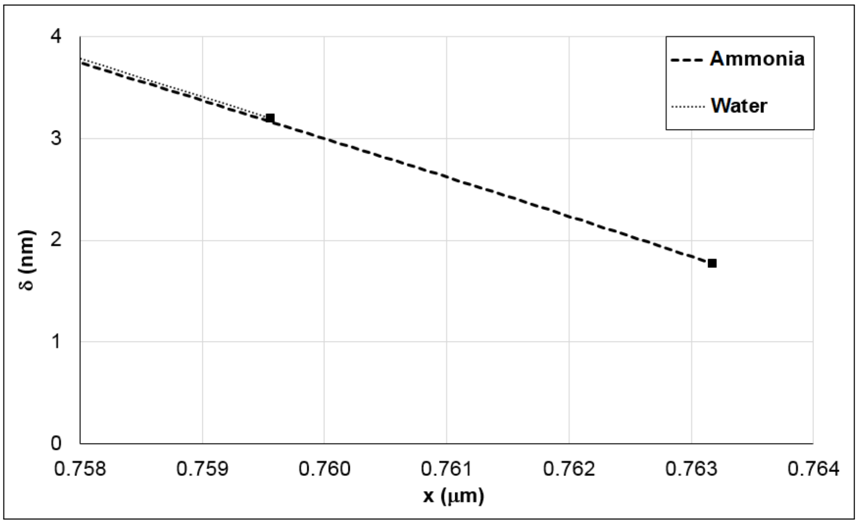

Figure 6.30: Variation of film thickness for water

Replacing ammonia with water results in an approximately, 4 nm decrease in the length of the micro region as shown in Figure 6.30.

As in the case of large superheat, variations of heat fluxes of water and ammonia utilizing systems are given in a normalized plot for small superheat, as shown in Figure 6.31.

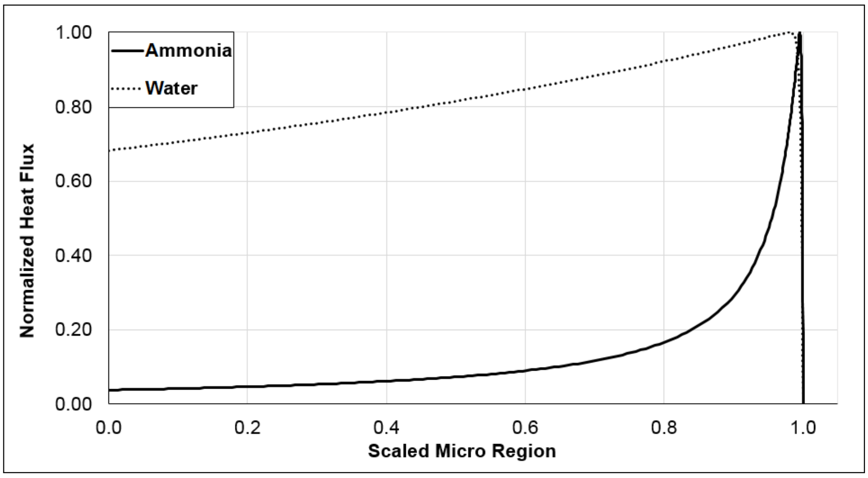

Figure 6.31: Variations of normalized heat flux in the scaled micro region for water and ammonia

When compared with systems subjected to high superheat, the same trends of heat fluxes are also achieved for small superheat as shown in Figure 6.31.

The negative absolute liquid pressure reported in the water system for large superheats (Figure 6.31) is also encountered in case of small superheat.

CHAPTER 7

DISCUSSION

The present study starts with the solution of simple unidirectional flow based evaporation model. Instead of starting the solution from the contact line, a location in the intrinsic meniscus region, where the effect of disjoining pressure is small, is taken as the starting point to the numerical solution in order to avoid the numerical difficulties and physical conflicts existing at the contact line.

The results of the unidirectional flow based model do not match the results of Stephan and Busse [31]. Starting with the same thickness, slope and radius of curvature values found at the end of the reference study, total heat transferred is estimated to be 18.5% less than the result of study of Stephan and Busse [31]. The reason for this decrease is originated from the difference of film thickness distributions of the two studies. As it was shown in Figure 3.4, when there is no enforced boundary condition at the contact line, film thickness of the present study does not asymptotically approaching zero. At first glance, film thickness preserves its contact angle and intersects with the x axis. This situation leads to a decrease in the length of the problem domain and explains the decrease in the total amount of evaporation. However, an interesting situation in the distribution of the film thickness reveals itself when the close vicinity of the contact line is examined. As shown in Figure 3.4, the second derivative of film thickness, δ, changes sign and the film profile bends inward near the contact line instead of asymptotically approaching zero. Such a profile is unusual and does not appear in the results of the studies reported in the literature. However, when the literature is carefully studied, a similar profile can be seen in Wayner [23] published in 1982. Wayner drew the conceptual views of the spreading and non-spreading systems for the isothermal and evaporating cases. In the sketch of the non-spreading systems, the contact line of the film bended inward and absorbed layer was not shown. In the present study, the film thickness at the contact line was estimated to be approximately, 0.5 nm. This value is even smaller than any realistic surface roughness of solid materials. Therefore, there is no physical counterpart of the adsorbed layer depicted as in the sketch of Wayner [23] for non-spreading systems. It does not mean that adsorbed layer does not exist but a smooth transition to the absorbed layer from the evaporating layer is not necessary at such a scale smaller than the surface roughness. In short, the film distribution found in the present study matches the non-spreading system definition of Wayner. Wayner [23] used different signs for the capillary and disjoining pressures when forming the augmented Young-Laplace equation for the non-spreading system. The author generalized this approach with use of the term "characteristic frequency for van der Waals interaction" which multiplies the disjoining pressure term and has different signs for spreading and non-spreading systems. However, the present study does not force the signs of the terms of the governing equations to change depending on whether the system is spreading or non-spreading. Instead, formulation of the the radius of curvature in the capillary pressure term is allowed to change its sign without any interference. An ammonia droplet does not entirely spread on an aluminium surface. Then, the system may be characterized as a non-spreading system. Following this fact, the sign of radius of the curvature of the system is changed to negative by bending the interface inward at a point near to the contact line. Due to the fact that capillary pressure is a function of curvature, it also becomes negative. The negative capillary pressure is important because there exists no mechanisms which can balance the rapidly increasing disjoining pressure due to ultra-thin film thickness values near the contact line.

It should be noted that summation of capillary and disjoining pressures should not exceed the vapor pressure, otherwise absolute liquid pressure drops below zero which leads to a physically unrealizable state. When the solution starts at the non-evaporating contact line, the thickness of the contact line is determined by equating Equation 3.31 to zero with the assumption of negligible capillary pressure. In other words, curvature at the contact line is assumed zero. Then, only the disjoining pressure survives at the right hand side of augmented Young-Laplace equation. The vapor pressure of the saturated system is the function of the vapor temperature, so its value is also fixed. Then, the value of liquid pressure can be calculated at the contact line from the augmented Young-Laplace equation. Some studies which start the solution from the contact line, such as Stephan and Busse [31], Wang *et al.* [36] or Du and Zhao [41], found negative liquid pressures at the contact line. Physically, there is no meaning of having negative absolute pressure. Then, the problems solved in these studies cannot exist physically. Starting the solution from the intrinsic region fixes this problem in the present study.

The maximum value of the heat flux, on the other hand, is estimated to be 6% higher than the value reached in the study of Stephan and Busse [31]. The reason of this difference is also due to the negative capillary pressure existing at the point of maximum evaporation. According to the evaporation flux model of Wayner, Equation 3.31, evaporation is promoted by superheat and suppressed by the temperature jump which is the summation of capillary and disjoining pressures. The negative capillary pressure forming at the close vicinity of the evaporation peak, reduces the pressure jump and thus, evaporation is promoted.

Another prediction of the current study is that analysis ends up with a contact line thickness value smaller than estimated in the literature. Except for the studies which analyze the problem experimentally and theoretically simultaneously, theoretical studies which have boundary conditions at the contact line, use Equation 3.31 to find the non - evaporating thickness by equating the heat flux to zero and using zero capillary pressure. However, when capillary pressure becomes negative with the sign change of the curvature of the film, a decrease in the film thickness of the non-evaporating region should be expected. Thus, non-evaporating thickness cannot be found *a priori*, and the problem has to be solved till the end of the domain where the liquid pressure gradient vanishes.

The application of the unidirectional flow assumption to the systems having moderate contact angles is questionable. The present study investigates the evaporation from the ammonia surface formed on aluminium surface with 19.7° contact angle. Therefore, small film slope assumption is not valid throughout the problem domain and vertical component of the velocity is also taken into consideration by replacing the unidirectional flow with the bi-directional flow. The solution of the evaporation model based on bi-directional flow in the problem domain, is only 0.04% different from the unidirectional flow based model. This result shows that there is no necessity of using bi-directional flow to model the evaporation in the systems having contact angles at least smaller than 20°. However, presentation of the distribution of vertical velocity in the micro region enables to understand the underlying physical phenomena.

To relate the model to the three dimensional problem in a heat pipe channel, the contribution of axial flow to the mass supply of the micro region is also analyzed in the present study. Although it was estimated that the contribution of the axial flow might be negligible due to the small dimensions of the micro region with respect to the whole groove geometry, a quantitative description of the phenomena is carried out to complete the analysis. The ratio of the axial mass flow to the evaporating mass in the micro region, is estimated to be 2×10^{-13}. This ratio shows that all of the fluid evaporated in the micro region is supplied from the undisturbed bulk meniscus region.

This thesis also includes a parametric study in which, a linear increase of the heat transfer is reported with the increasing superheat. Moreover, small contact angles yields increased heat transferred in the micro region due to extended range of micro region. As an outcome of the parametric study, systems which form small apparent contact angles between the wall and liquid, are suggested to get enhanced heat transfer.

CHAPTER 8

CONCLUSION AND SUGGESTIONS FOR FUTURE WORK

8.1 Conclusion

The contact line region of the evaporating meniscus has been subjected to the extensive research for approximately 50 years. Most of the analytic formulations are based on the unidirectional flow of the fluid parallel to the solid wall on which the meniscus forms. However, small film slope assumption is not valid for moderate contact angles and and vertical component of the velocity should be taken into consideration. Therefore, present study considers the solution of bi-directional flow based evaporation model in addition to unidirectional flow based model. Furthermore, the present study considers the evaporating meniscus as a part of the liquid-vapor interface formed within the groove of a rectangular grooved heat pipe and adds the effect of the flow perpendicular to the meniscus plane. Thus, three directional evaporation model is built for the first time in the literature for an evaporating meniscus or simply for a micro region. During the modelling efforts of the present study, following predictions are made:

1) By starting the solution of the unidirectional flow based evaporation model from the intrinsic meniscus region, the need for modification or tuning of boundary conditions is eliminated as long as no pre-determined shape is forced at the contact line.

2) In the present study, the sign change capability of the capillary pressure preserves the absolute liquid pressure from the possibility of having negative

values, as long as the problem is physically realizable.

3) Thickness of the contact line cannot be found *a priori* before the end of the numerical solution where the liquid pressure gradient becomes zero.

4) Unidirectional flow based evaporation model can be used even at the systems having moderate apparent contact angles.

5) In a heat pipe, the mass carried to the micro region due to axial flow is negligible.

6) To build a consistent evaporation model, theoretical study should be supported by an experimental study.

8.2 Suggestions For Future Work

In order to validate the use of models in engineering applications where large superheats are possible, more experimental data are needed. The application of experimental data obtained for small superheats to problems with large superheats, at bent, is questionable. The effect of surface roughness should be carefully investigated in these systems due to the fact that extremely small film thicknesses are predicted in large superheat systems, even smaller than the order of surface roughness.

On the other hand, experimental studies on the systems which have large contact angles, should be carried together with analytical verifications which use slope dependent disjoining pressure formulations.

REFERENCES

[1] E.AZAD. Theoretical and experimental investigation of heat pipe solar collector. *Experimental Thermal and Fluid Science*, 32:1666–1672, 2008.

[2] ThermoLab Co. Ltd. Wick structures. *http://thermolab.co.kr/3443*, last visited on June 2015.

[3] M.C.ZAGHDOUDI S.MAALEJ J.MANSOURI M.B.H.SASSI. Flat miniature heat pipes for electronics cooling: State of the art, experimental and theoretical analysis. *World Academy of Science, Engineering and Technology*, 51:879–902, 2011.

[4] Y.WANG K.VAFAI. An experimental investigation of the thermal performance of an asymmetrical flat plate heat pipe. *International Journal of Heat and Mass Transfer*, 43:2657–2668, 2000.

[5] YU.F.MAYDANIK. Loop heat pipes. *Applied Thermal Engineering*, 25:635–657, 2005.

[6] H.N.CHAUDHRY B.R.HUGHES S.A.GHANI. A review of heat pipe systems for heat recovery and renewable energy applications. *Renewable and Sustainable Energy Reviews*, 16:2249–2259, 2012.

[7] R.G.BRESSLER P.W.WYATT. Surface wetting through capillary grooves. *Transactions of the ASME*, page 126–132, 1970.

[8] P.C. WAYNER Jr. C.L.COCCIO. Heat and mass transfer in the vicinity of the triple interline of a meniscus. *AIChe Journal*, 17-3:569–575, 1971.

[9] M.POTASH Jr. P.C.WAYNER Jr. Evaporation from a two-dimensional extended meniscus. *International Journal of Heat and Mass Transfer*, 15:1851–1863, 1971.

[10] B.V.DERJAGUIN Z.M.ZORIN. Optical study of the adsorption and surface condensation of vapours in the vicinity of saturation on a smooth surface. *Proc. 2nd Int. Congr. Surface Activity, London*, 2:145–152, 1957.

[11] P.C.WAYNER Jr. Fluid flow in the interline of an evaporating non-zero contact angle meniscus. *International Journal of Heat and Mass Transfer*, 16:1777–1783, 1973.

[12] J.F.PADDAY. Cohesive properties of thin films on liquids adhering to a solid surface. *Special Discussion, Faraday Society,Cambridge*, 6:65–74, 1970.

[13] R.W.SCHRAGE. *A Theoretical Study of Interphase Mass Transfer.* Columbia University Press, New York, 1953.

[14] P.C.WAYNER Jr. Y.K.KAO L.V.LACROIX. The interline heat-transfer coefficient of an evaporating wetting film. *International Journal of Heat and Mass Transfer*, 19:487–492, 1976.

[15] F.RENK P.C.WAYNER Jr. G.M.HOMSY. On the transition between a wetting film and a capillary meniscus. *Journal of Colloid and Interface Science*, 67:408–414, 1978.

[16] F.W.HOLM S.P.GOPLEN. Heat transfer in the meniscus thin-film region. *Journal of Heat Transfer*, 101:543–547, 1979.

[17] P.C.WAYNER Jr. Effect of interfacial phenomena in the interline region on the rewetting of a hot spot. *International Journal of Heat and Mass Transfer*, 22:1033–1040, 1979.

[18] F.J.RENK P.C.WAYNER Jr. An evaporating ethanol meniscus part i: Experimental studies. *Journal of Heat Transfer*, 101:55–58, 1979.

[19] F.J.RENK P.C.WAYNER Jr. An evaporating ethanol meniscus part ii: Analytical studies. *Journal of Heat Transfer*, 101:59–62, 1979.

[20] S.MOOSMAN G.M.HOMSY. Evaporating menisci of wetting fluids. *Journal of Colloid and Interface Science*, 73:212–223, 1980.

[21] P.C.WAYNER Jr. Interfacial profile in the contact line region of a finite contact angle system. *Journal of Colloid and Interface Science*, 77:495–500, 1980.

[22] P.HU A.W.ADAMSON. Adsorption and contact angle studies ii. water and organic substances on polished polytetrafluoroethylene. *Journal of Colloid and Interface Science*, 59:605–614, 1977.

[23] P.C.WAYNER Jr. Adsorption and capillary condensation at the contact line in change of phase heat transfer. *International Journal of Heat and Mass Transfer*, 25:707–713, 1982.

[24] M.SUJANANI P.C.WAYNER Jr. Microcomputer-enhanced optical investigation of transport processes with phase change in near-equilibrium thin liquid films. *Journal of Colloid and Interface Science*, 2:472–488, 1991.

[25] J.A.SCHONBERG P.C.WAYNER Jr. Analytical solution for the integral contact line evaporative heat sink. *Journal of Thermophysics*, 6:128–134, 1992.

[26] S.DASGUPTA J.A.SCHONBERG I.Y.KIM P.C.WAYNER Jr. Use of the augmented young-laplace equation to model equilibrium and evaporating extended menisci. *Journal of Colloid and Interface Science*, 157:332–342, 1993.

[27] S.DASGUPTA J.A.SCHONBERG P.C.WAYNER Jr. Investigation of an evaporating extended meniscus based on the augmented young-laplace equation. *Journal of Heat Transfer*, 115:201–208, 1993.

[28] S.DASGUPTA I.Y.KIM P.C.WAYNER Jr. Use of the kelvin-clapeyron equation to model an evaporating curved microfilm. *Journal of Heat Transfer*, 116:1007–1015, 1994.

[29] I.Y.KIM P.C.WAYNER Jr. Shape of an evaporating completely wetting extended meniscus. *Journal of Thermophysics and Heat Transfer*, 10:320–325, 1996.

[30] J.A.SCHONBERG S.DASGUPTA P.C.WAYNER Jr. An augmented young-laplace model of an evaporating meniscus in a microchannel with high heat flux. *Experimental Thermal and Fluid Science*, 10:163–170, 1995.

[31] P.C.STEPHAN C.A.BUSSE. Analysis of the heat transfer coefficient of grooved heat pipe evaporator walls. *International Journal of Heat and Mass Transfer*, 35(2):383–391, 1992.

[32] J.M.HA G.P.PETERSON. The interline heat transfer of evaporating thin films along a micro grooved surface. *Journal of Heat Transfer*, 118:747–755, 1996.

[33] S.K.THOMAS R.C.LYKINS K.L.YERKES. Fully developed laminar flow in trapezoidal grooves with shear stress at the liquid-vapor interface. *International Journal of Heat and Mass Transfer*, 44:3397–3412, 2001.

[34] S.LAUNAY V.SARTRE M.LALLEMAND. Hydrodynamic and thermal study of a water-filled micro-heat-pipe array. *Journal of Thermophysics and Heat Transfer*, 18(3):358–363, 2004.

[35] S.K.WEE K.D.KIHM K.P.HALLINAN. Effects of the liquid polarity and the wall slip on the heat and mass transport characteristics of the micro-scale evaporating transition film. *International Journal of Heat and Mass Transfer*, 48:265–278, 2005.

[36] H.WANG S.V.GARIMELLA J.Y.MURTHY. Characteristics of an evaporating thin film in a microchannel. *International Journal of Heat and Mass Transfer*, 50:3933–3942, 2007.

[37] H.WANG S.V.GARIMELLA J.Y.MURTHY. An analytical solution for the total heat transfer in the thin-film region of an evaporating meniscus. *International Journal of Heat and Mass Transfer*, 51:6137–6322, 2008.

[38] R.BERTOSSI Z.LATAOUI V.AYEL C.ROMESTANT Y.BERTIN. Modeling of thin liquid film in grooved heat pipes. *Numerical Heat Transfer*, A(55):1075–1095, 2009.

[39] K.H.DO S.J.KIM S.V.GARIMELLA. A mathematical model for analyzing the thermal characteristics of a flat micro heat pipe with a grooved wick. *International Journal of Heat and Mass Transfer*, 51:4637–4650, 2008.

[40] K.H.DO S.P.JANG. Effect of nanofluids on the thermal performance of a flat micro heat pipe with a rectangular grooved wick. *International Journal of Heat and Mass Transfer*, 53:2183–2192, 2010.

[41] S.DU Y.H.ZHAO. New boundary conditions for the evaporating thin-film model in a rectangular micro channel. *International Journal of Heat and Mass Transfer*, 54:3694–3701, 2011.

[42] A.M.BENSELAMA S.HARMAND K.SEFIANE. Thermocapillary effects on steadily evaporating contact line: A perturbative local analysis. *Physics of Fluids*, 24(072105):1–38, 2012.

[43] G. ODABAŞI. Modeling of multidimensional heat transfer in a rectangular grooved heat pipe. *Middle East Technical University, Ph.D. Thesis*, 2014.

[44] V.P.CAREY. *Liquid-vapor Phase Change Phenomena.* Hemisphere Publishing House, New York, 1992.

[45] B.V.DERJAGUIN E.OBUCHOV. *J. Colloid Chemistry*, 1:385, 1935.

[46] B.V.DERJAGUIN L.M.SHCERBAKOV. *Colloid J. U.S.S.R.(trans)*, 23:33, 1961.

[47] V.M.STAROV. Suface forces action in a vicinity of three phase contact line and other current problems in kinetics of wetting and spreading. *Advances in Colloid and Interface Science*, 161:139–152, 2010.

[48] B.V.DERJAGUIN N.V.CHURAEV. The current state of the theory of long-range surface forces. *Colloid Surf. A*, 41:223–237, 1989.

[49] N.V.CHURAEV B.V.DERJAGUIN. Inclusion of structural forces in the theory of stability of colloids and films. *Journal of Colloid and Interface Science*, 103:542–553, 1985.

[50] D.KHRUSTALEV A.FAHGRI. Heat transfer during evaporation on capillary-grooved structures of heat pipes. *Journal of Heat Transfer*, 117:740–747, 1995.

[51] C.A.MILLER E.RUCKENSTEIN. The origin of flow during wetting of solids. *Journal of Colloid and Interface Science*, 48(3):368–373, 1974.

[52] L.BISWAL S.K.SOM S.CHAKRABORTY. Thin film evaporation in microchannels with slope and curvature dependent disjoining pressure. *International Journal of Heat and Mass Transfer*, 57:402–410, 2013.

[53] Q.WU H.WONG. A slope-dependent disjoining pressure for non-zero contact angles. *Journal of Fluid Mechanics*, 506:157–185, 2004.

[54] K.PARK K.NOH K.LEE. Transport phenomena in the thin-film region of a micro-channel. *International Journal of Heat and Mass Transfer*, 46(13):2381–2388, 2003.

[55] K.PARK K.LEE. Flow and heat transfer characteristics of the evaporating extended meniscus in a micro-capillary channel. *International Journal of Heat and Mass Transfer*, 46(24):4587–4594, 2003.

[56] W.J.GORDON C.A.HALL. A review of heat pipe systems for heat recovery and renewable energy applications. *Numer. Math.*, 21:109–209, 1973.

[57] M.MARKOS-GEBRESILASSIE. Steady liquid flow and liquid-vapor interface shapes in different groove structures in micro heat pipes. *Southern Methodist University, Ph.D. Thesis*, 2007.

APPENDIX A

FLOW CHART OF THE SOLUTION PROCEDURE

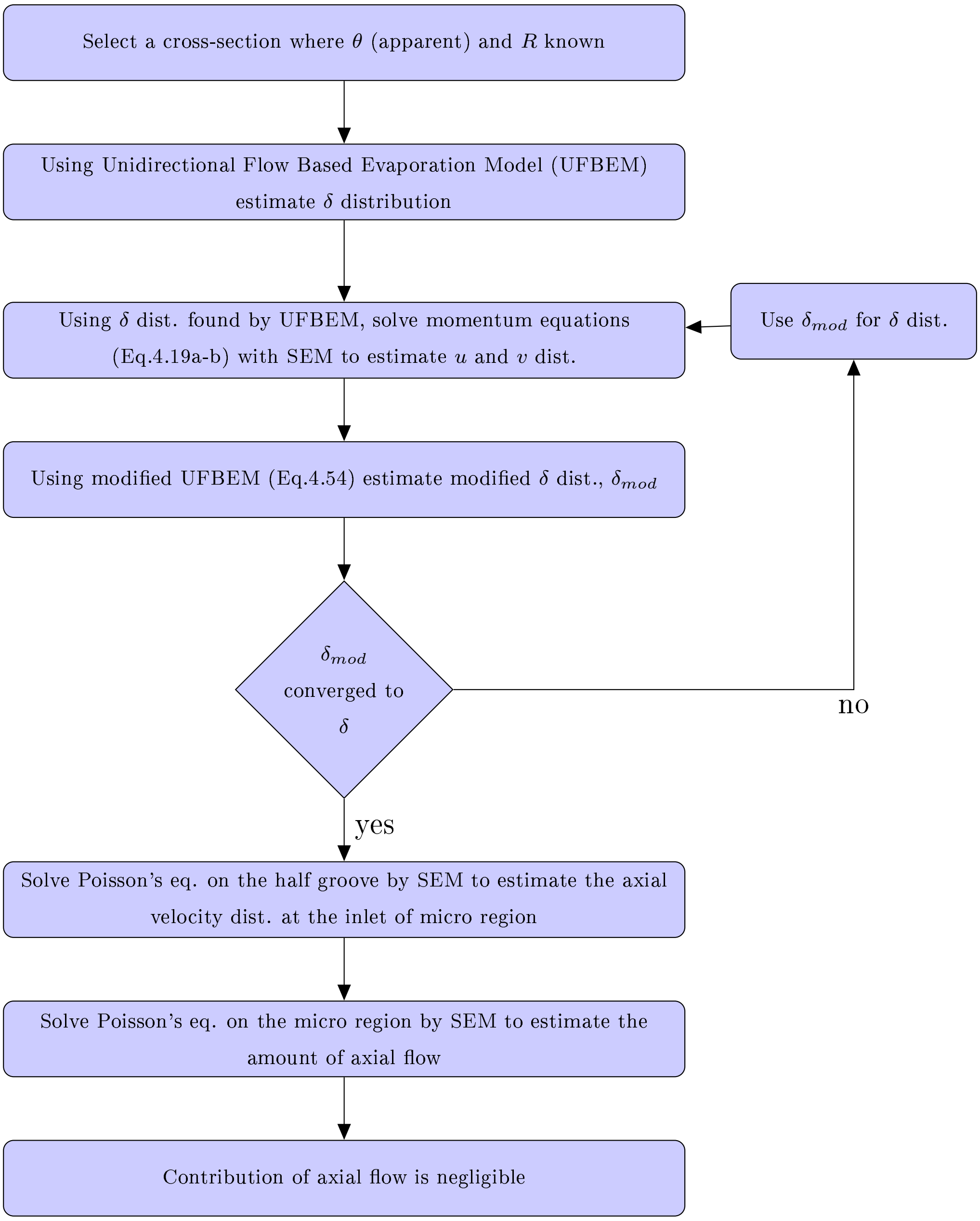

CURRICULUM VITAE

PERSONAL INFORMATION

Surname, Name: AKKUŞ, Yiğit
Nationality: Turkish (TC)
Date and Place of Birth: 1987, İzmir
Marital Status: Married
Phone: (505)5307831
Fax: (312)3544138

EDUCATION

Degree	**Institution**	**Year**
Metallurgical&Materials Eng./Minor	METU	2010
Mechanical Eng./B.S.	METU	2009
High School	Turgutlu Halil Kale Fen L.	2004

PROFESSIONAL EXPERIENCE

Year	**Place**	**Enrollment**
2014–Present	ASELSAN	Expert Engineer
2009–2014	ASELSAN	Engineer